2014-10-30

Periodic and Periodic Phase-Reversal Broadside Scanning Leaky-Wave Antennas in Substrate Integrated Waveguide

Henry, Robert

UNIVERSITY OF CALGARY

Periodic and Periodic Phase-Reversal Broadside Scanning Leaky-Wave Antennas in Substrate Integrated Waveguide

by

Robert Henry

A THESIS

SUBMITTED TO THE FACULTY OF GRADUATE STUDIES

IN PARTIAL FULFILLMENT OF THE REQUIREMENTS FOR THE

DEGREE OF MASTER OF SCIENCE

DEPARTMENT OF ELECTRICAL AND COMPUTER ENGINEERING

CALGARY, ALBERTA

OCTOBER, 2014

Abstract

In recent years the preferred solution for achieving broadside scanning LWA performance in substrate integrated waveguide (SIW) has been the composite right/left handed (CRLH) leaky wave antenna (LWA). This thesis offers an alternative approach by outlining the design and study of a new periodic LWA architecture that uses half-mode SIW (HMSIW) to feed an array of antipodal tapered slot antenna (ATSA) radiating elements. The new antenna was among the first SIW based periodic LWAs to address the open-stopband that typically hinders broadside radiation, and was the first to do so using a unit-cell matching technique.

Additionally, a compact periodic phase-reversal architecture of the antenna is presented that allows the ATSA element spacing to be reduced, enabling design with a comparatively low substrate permittivity while maintaining grating lobe free scanning. This antenna was the first SIW based LWA to use the periodic phase-reversal technique.

Keywords: Substrate Integrated Waveguide, Leaky Wave Antenna, Traveling Wave Array

Acknowledgements

Firstly, I would like to thank my supervisor Dr. Michał Okoniewski for his technical and professional support over the last two years, without which the work in this thesis would not have been possible. I am additionally thankful for his enthusiasm, confidence, and positivity, which are a contagious gift of his, that offered a cure to my doubts when I was plagued by them. The opportunity to experience working with Michał has been one of my favorite aspects of my time in graduate studies.

I would also like to thank Dr. Geoff Messier for providing me with my first research experience and for his continued guidance and support. I look up to Geoff as a role model for organized professionalism, without cost to a calm, patient, insightful and lighthearted persona. I truly enjoyed working with him.

Dr. Mike Potter, who as the professor of the first EM course I ever had the pleasure of taking (and later TA-ing), I blame at least in part for my chosen career path. Dr. Elise Fear, who as the professor of the second EM course I had the pleasure of taking (and again later TA-ing), I blame equally. Luckily I love my work, and my career path looks as bright as the sarcastic light under which I blame these professors. Sarcasm aside, the opportunity to work with, and learn from, these amazing people has enriched my experience as a student and I thank them for it.

Chris Simon, Dr. Billy Wu, Thomas Apperley, Dr. Adrian Sutinjo, Dr. Ron Johnston, and John Shelley were priceless guides through many technical aspects of my work, without whom the quality and time-line of my thesis would have suffered immensely. I also owe a great deal of my success, and my mostly retained sanity as a graduate student, to Andrew Lesser, Marcel Seguin, Jeremie Bourqui, John Garret, Bushra Muharram, Tony Dratnal, Charlotte Curtis, Andrew Loblaw, Trevor Cameron, Adrea Dukeshire, Zhixing Zhao, Benjamin Lavoie, Kay Liu, Doug Kurrant, and Marcel Nauta. I offer my thanks to all of these people for their

helpfulness without hesitation, and more importantly their company, and friendship, over the last two years.

This acknowledgment would not be complete without recognition of my friends outside the University. Without Tara Hiscox, who taught me what hard work looks like, I would not be where I am today. Without Trent Francisco, who ensured that I played every bit as hard as I learned to work from Tara, I would not be where I am today. The spectrum of friends I have defines me, and I thank them for defining me as I am.

Don, Elaine, and Kristy Henry, my family, are the brightest colors in the spectrum and the best friends I could possibly imagine. I owe them everything, including my deepest thanks for their endless love and unwavering support.

Finally, I would like to acknowledge and give thanks to the National Science and Engineering Research Council of Canada (NSERC) and the Canadian Microelectronics Corporation (CMC) for their generous support in funding and resources.

Table of Contents

List of Tables

List of Figures and Illustrations

List of Abbreviations

Symbol	Definition
LWA	Leaky-Wave Antenna
SIW	Substrate Integrated Waveguide
HMSIW	Half-Mode Substrate Integrated Waveguide
CRLH	Composite Right/Left-Handed
VNA	Vector Network Analyzer
HFSS	High-Frequency Structural Simulator
PCB	Printed Circuit Board
IC	Integrated Circuit
DUT	Device Under Test
AUT	Antenna Under Test
dB	Decibels
dBi	Decibels-isotropic
TRL	Thru-Reflect-Line
FEM	Finite Element Method
TE	Transverse-Electric
TM	Transverse-Magnetic
TEM	Transverse-Electric-Magnetic
AF	Array Factor
VSWR	Voltage Standing Wave Ratio
ATSA	Antipodal Tapered Slot Antenna
PMMA	Poly(methyl 2-methylpropenoate) (Plexiglas®)

Chapter 1

Introduction

Antennas are indispensable components in wireless electronic systems, enabling the transmission and reception of electromagnetic waves over great distances through no apparent material medium. Applications of this type of electromagnetic energy manipulation (i.e. radiation) are endless, notable examples to date including mobile communications, radio broadcast, remote sensing, radar, and microwave heating [1].

The operating frequency of any wireless system is highly application dependent. The lowest and highest usable frequencies in modern wireless technology are often dictated by antenna and circuit size limitations. Antenna sizes used for efficient radiation are generally inversely proportional to the intended frequency of operation, such that very low frequency (long wavelength) antennas can become prohibitively large and as frequency increases (i.e. wavelength decreases) antennas can become so small that fabrication may be impractical or impossible. Some types of structures are easier and more affordable to miniaturize than others, probably the most notable of which are planar printed circuit and integrated circuit structures with some features being realizable on a nano-meter scale [2]. For this reason a large amount of antenna research for high frequencies with very short wavelengths is constrained to planar structures. In this thesis two new planar antenna architectures are investigated that lend themselves well to mass production and operation in the mm-wave frequency range (30-300GHz).

1.1 Motivation

Increasing the frequency of wireless technology tends to support the progression of broadband and high resolution techniques. For this reason, wireless technology applications such

as wireless networks, automotive radars, imaging sensors, and biomedical devices have begun to utilize the mm-wave frequency range [3]. The commercial success of these systems often relies on their compatibility with exiting mass-production techniques. In particular planar structures utilizing well established printed circuit board (PCB) and integrated circuit (IC) fabrication processes can usually be mass produced at a relatively low cost. Transmission lines traditionally used at lower microwave frequencies (like microstrip and coplanar waveguide) do not scale to the mm-wave frequency range without significantly higher conductor and radiation losses, resulting in severe Q-factor degradation for components based on these technologies. Rectangular waveguide can be used to design high-Q mm-wave components however are bulky and impractical for mass production due to precision machining requirements and post fabrication assembly and tuning requirements [3]. To address this problem, the rectangular waveguide which provides very efficient transmission at mm-wave frequencies has effectively been realized in planar form as substrate integrated waveguide (SIW) [4]. Despite some performance degradation compared to rectangular waveguide, SIW offers very efficient transmission and a relatively high power handling capacity in comparison to other planar transmission lines of similar fabrication complexity [4], [5].

The invention of substrate integrated waveguide (SIW) for efficient mm-wave system integration has opened the door to a wealth of new research opportunities. The flexibility of SIW based systems (and therefore their usefulness in mass producing mm-wave technology) hinges upon the availability of SIW compatible components and thus much effort has been expended to create all kinds of SIW based devices and components including antennas.

Leaky wave antennas (LWAs) are traditionally praised for their simple feed mechanism, directive radiation, and frequency dependent beam scanning [6]. One problem associated with leaky wave antennas is that broadside radiation requires specialized design techniques in order to be realized [7]–[9]. In SIW, composite right/left-handed (CRLH) LWAs have received particular interest (after first being realized in microstrip LWAs in 2008 [10]) and

can offer broad scan ranges in addition to broadside radiation [11] (referred to as broadside scanning radiation). In this thesis it will be shown that a half mode SIW (HMSIW) [12] based periodic LWA architecture using antipodal tapered slot antenna (ATSA) radiating elements can offer comparable broadside-scanning performance with maximum radiation in the plane of the substrate [13]. Previously, all existing broadside scanning SIW based LWAs (reviewed in Chapter 2 Section 2.3) offered maximum radiation in the space above and/or below the substrate plane.

The simplest periodic LWA designs generally exhibit an open-stopband at the broadside frequency which results in a standing wave on the structure and diminished radiated power. [14] The addition of a unit-cell matching section to the HMSIW periodic LWA design presented in this thesis enabled broadside radiation from the antenna, which, like the CRLH approach, was a technique that was first realized in microstrip based LWAs [15]–[16]. To the author's knowledge, the proposed antenna was the first SIW based periodic LWA to use the unit-cell matching technique for achieving broadside scanning radiation. Prior to the new design, only one other SIW based periodic LWA found in literature [17] had achieved broadside-scanning radiation, however it used a different and arguably less effective technique for addressing the broadside open-stopband [15]. All other broadside scanning SIW based LWA architectures found in literature were of the CRLH variety (reviewed in Chapter 2 Section 2.3).

One limitation associated with the proposed design was the high permittivity requirement of the substrate needed to keep element spacing small enough to avoid grating lobes over the entire scan range of the antenna. For this reason an additional compact periodic phase-reversal architecture of the antenna was realized [18]. In [19] it was shown that the periodic phase-reversal of adjacent series fed radiating elements, which reduces element spacing, can relax high substrate permittivity requirements for some full space scanning antennas, as is the case for the proposed design. To the author's knowledge the proposed design was the

first time the periodic phase-reversal technique for radiating element spacing reduction had been employed in an SIW based periodic LWA.

Two new but similar antenna designs are therefore outlined in this thesis, the second being a periodic phase-reversal version of the first. The two architectures are referred to as the "non-inverting element" architecture and the "periodic phase-reversal" architecture. Reasons for the names used will become clear in Chapter 3 where the proposed architectures are first presented.

The antenna architectures outlined in Chapter 3 and the associated results in Chapter 5 are largely reproduced from the following previously published works:

- ©[2014] IEEE. Reprinted, with permission, from [Henry, R.; Okoniewski, M., "A new half mode substrate integrated waveguide leaky wave antenna," 8th European Conference on Antennas and Propagation (EuCAP), pp.586–589, 6–11 April 2014] [20]

- ©[2014] IEEE. Reprinted, with permission, from [Henry, R.; Okoniewski, M., "A Broadside-Scanning Half-Mode Substrate Integrated Waveguide Periodic Leaky-Wave Antenna," Antennas and Wireless Propagation Letters, IEEE, vol.13, pp.1429–1432, 2014] [13]

- ©[2014] IEEE. Reprinted, with permission, from [Henry, Robert; Okoniewski, Michal, "Half mode substrate integrated waveguide periodic leaky wave antenna with antipodal tapered slots," Antennas and Propagation Society International Symposium (APSURSI), pp.1284,1285, 6–11 July 2014] [18]

- ©[2014] IEEE. Reprinted, with permission, from [Henry, R.; Okoniewski, M., "A Compact Broadside Scanning Substrate Integrated Waveguide Periodic Phase-Reversal Leaky Wave Antenna," Antennas and Wireless Propagation Letters, IEEE 2014] - Pending Approval

1.2 Thesis Goals and Expected Contributions

The primary goals of this thesis are:

- To develop a conceptual framework from which the new antenna designs can be understood
- To outline the existing state of the SIW based broadside scanning LWA field of knowledge from which the value of the new antenna designs can be appreciated
- To demonstrate the design approach used to arrive at the non-inverting element periodic LWA architecture (introduced in Chapter 3) and to validate the applicability of leaky wave theory to the new structure
- To demonstrate the design approach used for the periodic phase-reversal LWA architecture (introduced in Chapter 3) and to validate the applicability of leaky wave theory to the new structure
- To verify the theoretical performance of the new antenna designs through simulations and prototyping

In meeting the thesis goals, the expected contributions of the thesis are:

- To show that periodic LWAs can be designed in SIW as an alternative to CRLH LWAs which previously dominated the SIW based broadside scanning LWA field of knowledge (with the exception of the work in [17])
- To develop and validate the unit-cell matching technique for broadside open-stopband mitigation in an SIW based periodic LWA
- To develop and validate the periodic phase-reversal technique for size reduction and/or substrate permittivity reduction in a SIW based periodic LWA

- To offer two new SIW based broadside scanning LWA designs that radiate with maximum intensity in the substrate plane where previously maximum radiation for all SIW based broadside scanning LWAs had been in the space above and/or below the substrate plane

1.3 Thesis Outline

This thesis is structured as follows:

- Chapter 2 briefly outlines and explores the required background theory for understanding the proposed antenna designs as well as explores existing solutions to the SIW based broadside scanning LWA problem in order to understand the knowledge gap filled by the new designs.
- Chapter 3 introduces the proposed antenna architectures and explains their mechanisms of operation from a high level.
- Chapter 4 delves into details of the analysis and design techniques that were used to arrive at the exact dimensions of the proposed antenna architectures.
- Chapter 5 presents simulated and measured antenna results.
- Chapter 6 concludes the thesis with a discussion of the results and contributions as well as outlines possibilities for future work.

Chapter 2

Background

In order to understand the antenna architectures, design procedures, and results outlined in the remaining chapters of this thesis, some background information is essential. The goal of this chapter is therefore to introduce some relevant theory and design techniques pertaining to SIW and broadside scanning LWAs. In addition, existing broadside radiating SIW based LWAs are introduced and discussed in order to develop a framework from which the value of the proposed new designs can be appreciated.

2.1 Substrate Integrated Waveguide

As was mentioned in the introduction, SIW is a planar alternative to conventional rectangular waveguide technology (first proposed in [4]). SIW and rectangular waveguide behave nearly identically (for selected modes), so much so that most analysis stems from a transformation of SIW into an equivalent rectangular waveguide model [21, 22, 23]. This section therefore introduces relevant rectangular waveguide theory, followed by the methods through which the theory is applied to SIW and HMSIW analysis.

2.1.1 Rectangular Waveguide Transmission Line Modeling

A rectangular waveguide is a type of transmission line which is a structure that guides or transmits electromagnetic waves. The structure, as the name might imply, is rectangular in its cross-section and will contain air or some other material characterized by relative electric permittivity (ϵ_r) and relative magnetic permeability (μ_r). A photograph of a typical rectangular waveguide along with some parameter definitions is shown in Figure 2.1.

Assuming the structure is infinitely extending in the longitudinal (y) direction, the field

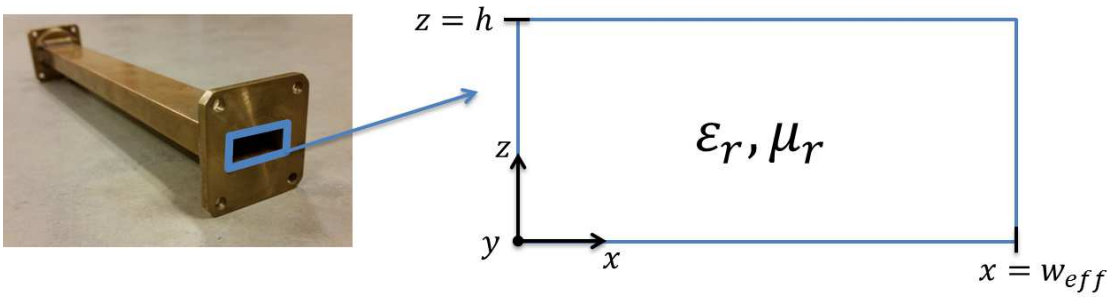

Figure 2.1: Rectangular waveguide and its cross-sectional dimensions

solutions for the allowed modes (electric and magnetic field distributions) within the waveguide are governed by the frequency of operation, the cross-sectional dimensions of the waveguide, and the filling material properties ϵ_r and μ_r. In fact, the exact field solutions can be solved by applying the appropriate boundary conditions to the 3-D electromagnetic wave equations which can be derived directly from Maxwell's equations [24, 25].

From these solutions it can be shown that waveguides (which generally consist of a single conductor) can support transverse electric (TE) and transverse magnetic (TM) modes, while transverse electric magnetic (TEM) modes are impossible. For fundamental theory on these subjects, [24] and [25] are excellent references.

In this thesis the fundamental TE mode is used for the proposed antenna designs and is therefore of main interest. For a given mode the waveguide can be treated as a dispersive transmission line with a phase constant β, attenuation coefficient α, and wave impedance Z_{TE} as shown in Figure 2.2. Waveguide analysis from the transmission line perspective allows system level designers to avoid the unnecessary complexity of computing full field solutions for the structure.

The following equations [24] can be used to compute the transmission line parameters of a rectangular waveguide. Firstly, the cutoff wavenumber dictates the minimum frequency of operation of the desired mode, below which propagation will not occur. For a rectangular waveguide with width w_{eff}, height h and dielectric filling with relative permittivity ϵ_r (and assuming $\mu_r = 1$) as shown in Figure 2.1, the cutoff wavenumber of the TE_{mn} mode can be

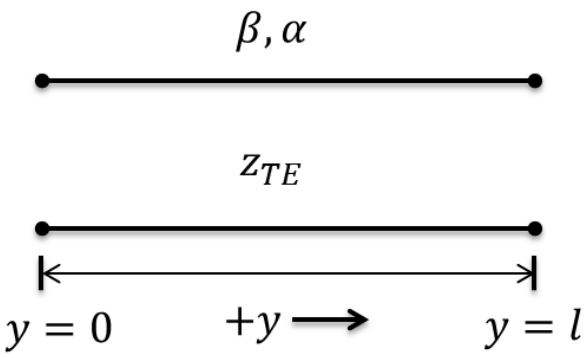

Figure 2.2: Equivalent transmission line model of a rectangular waveguide

calculated as:

$$k_c = \sqrt{(m\pi/w_{\text{eff}})^2 + (n\pi/h)^2}, \quad m, n \in \{0, 1, 2, ...\} \tag{2.1}$$

where

$$k = \omega\sqrt{\mu\epsilon}. \tag{2.2}$$

The phase constant in the direction of propagation (i.e. the longitudinal axis of the rectangular waveguide) can then be calculated as:

$$\beta = \sqrt{(k)^2 - (k_c)^2}. \tag{2.3}$$

The cutoff frequency for the specified mode is given by:

$$f_c = \frac{c}{2\pi\sqrt{\epsilon_r}}k_c = \frac{c}{2\pi\sqrt{\epsilon_r}}\sqrt{(m\pi/w_{\text{eff}})^2 + (n\pi/h)^2}. \tag{2.4}$$

From the longitudinal phase constant, the guided wavelength is defined by:

$$\lambda_g = \frac{2\pi}{\beta}, \tag{2.5}$$

and the wave impedance is given by,

$$Z_{TE} = \frac{k\eta}{\beta}, \tag{2.6}$$

where η is the wave impedance of a TEM wave propagating in the waveguide filling material. Wave impedance η is defined as:

$$\eta = \frac{\mu_r \mu_0}{\epsilon_r \epsilon_0}. \tag{2.7}$$

It will be shown that the above transmission line modeling of rectangular waveguide can similarly be applied to substrate integrated waveguide in order to simplify design.

2.1.2 SIW and Half-Mode SIW Transmission Line Modeling

SIW uses linear arrays of closely spaced metalized vias to realize the sidewalls of the rectangular waveguide while top and bottom walls are metal substrate layers. A typical SIW configuration and its design parameters are shown in Figure 2.3 along with a fabricated prototype.

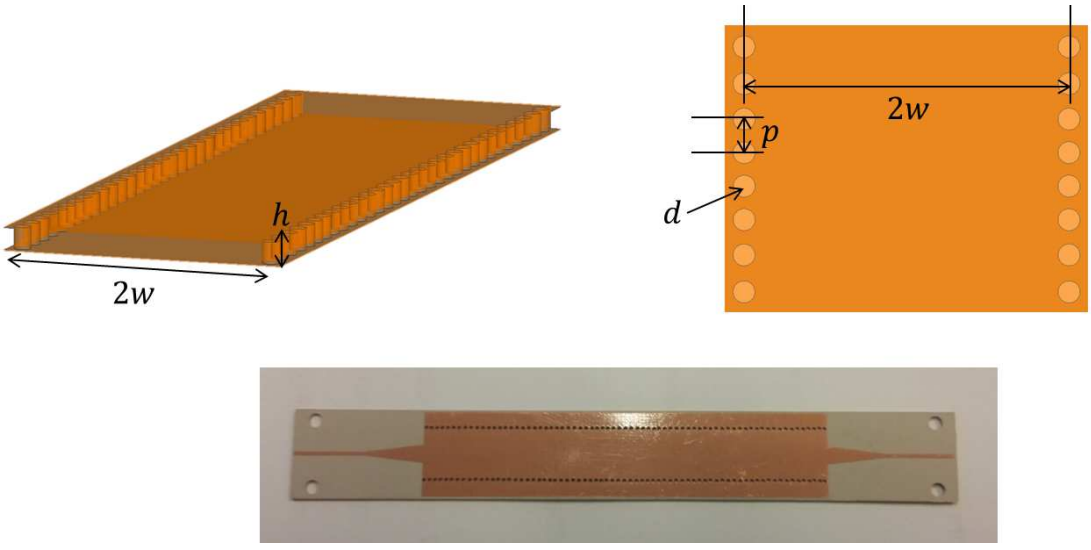

Figure 2.3: SIW geometry and prototype

With appropriate via diameter (d) and spacing (p) relative to a guided wavelength the

leakage loss from the space between vias is negligible and the field solutions are very similar to those observed in rectangular waveguides [26] (electric field magnitudes shown Figure 2.5). Metal layers and metalized vias are commonly used structures in most fabrication processes meaning that SIW lends itself well to mass production using existing fabrication facilities and enables its integration with other planar technologies.

Similar to rectangular waveguides, it is often useful in analysis to treat SIW as a dispersive transmission line rather than solving field equations. The transmission line properties for a given mode geometry are fully defined by the frequency of operation, the dimensions of the SIW ($2w$ and h in Figure 2.3), and the chosen substrate permittivity. From Figure 2.3 it is apparent that the width of SIW is somewhat arbitrary due to via spacing and diameters. For this reason, numerous empirically derived equations have been developed to enable calculation of an equivalent rectangular waveguide width (w_{eff}) from which dispersive properties can be modeled [21, 22, 23]. In this thesis the equation provided in [23], shown here:

$$w_{\text{eff}} = 2w - \frac{d^2}{0.95 \cdot p}, \tag{2.8}$$

was used due to its relative simplicity. In order to ensure this approximation is valid and that leakage does not occur between vias, the following conditions must be met [26]:

$$d < \frac{\lambda_g}{5}, \tag{2.9}$$

and

$$p \leq 2d. \tag{2.10}$$

With a rectangular waveguide effective width calculated the dispersive transmission line properties of the SIW can be calculated using equations 2.1– 2.7.

Half-mode SIW is essentially SIW split longitudinally at its center along the broad wall as shown in Figure 2.4, which is allowed by the symmetric field distribution of the fundamental TE_{10} SIW mode about the longitudinal axis shown in Figure 2.5. Half-mode SIW was first demonstrated in [12] and has been shown to offer comparable performance to full SIW.

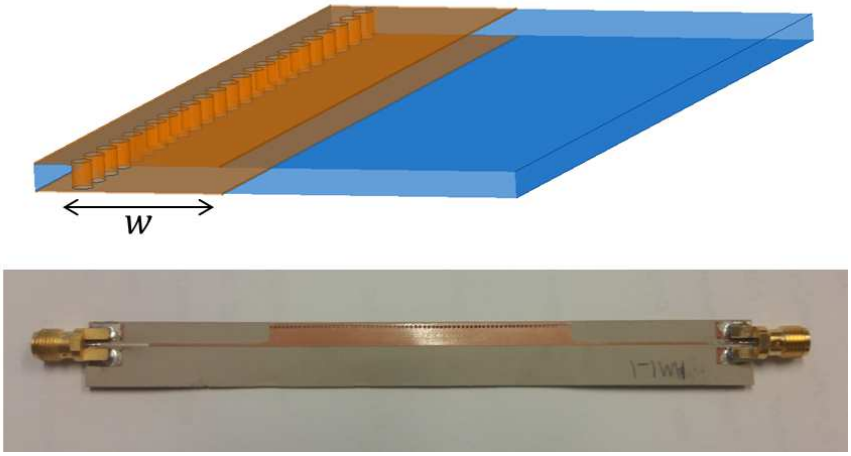

Figure 2.4: Half-mode SIW geometry and prototype

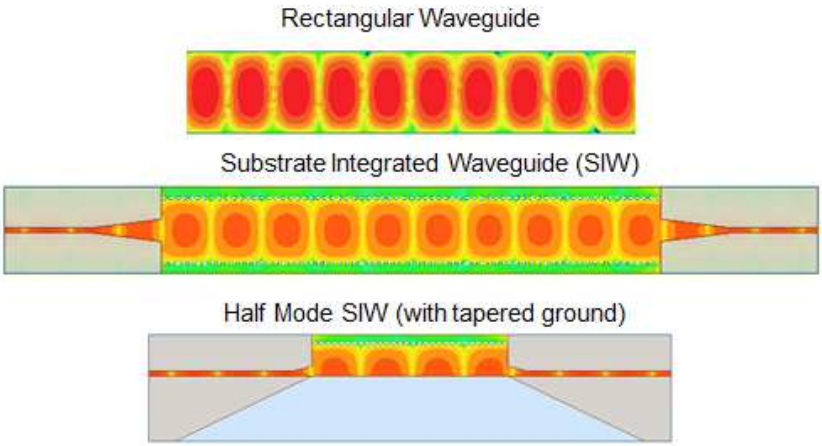

Figure 2.5: Electric field magnitudes for rectangular waveguide, SIW and HMSIW

The dispersive transmission line properties (β and Z_{TE}) of a HMSIW with a width w are approximately equivalent to an SIW of width $2w$. A rough estimate of HMSIW dimensions for a desired cutoff frequency and dispersion properties can therefore be calculated using the

rectangular waveguide transformation from equation 2.8 to obtain an equivalent SIW width of $2w$, such that the equivalent HMSIW width is w.

More precise HMSIW analysis is available in [27] which accounts for fringing fields at the open sidewall of the HMSIW. The fringing fields are approximated as an extension of HMSIW width w by $\triangle w$ resulting in a reduction in the expected cutoff frequency. This more accurate analysis is not, however, directly applicable to the HMSIW design in this thesis, as it was derived semi-empirically for HMSIW with an extended ground plane, while the HMSIW ground plane in this thesis ends at the open sidewall, as shown in Figure 2.4.

2.2 Leaky-Wave Antenna Theory

Leaky wave antennas are generally realized by introducing a radiating perturbation (uniformly or periodically) to a wave-guiding structure such that it radiates along its length [14]. It will be shown in this section that the analysis of such a structure relies heavily on determining its "leaky-wavenumber" ($k_{LW} = \beta - j\alpha$) which describes the phase and attenuation of the wave propagating along the length of the antenna. For an LWA to be realized, the perturbation introduced to the guided wave must be such that a "fast wave" is open to free space. A fast wave is one with a phase constant $\beta < k_0$ where k_0 is the free space wavenumber. Conversely a slow wave has a phase constant $\beta > k_0$ and in general will not radiate even when open to free space. Analysis supporting the observation that fast waves radiate and slow waves do not can be reviewed in detail in [28].

Now, assuming an open, fast wave structure is realized, if the radiation leakage is weak (corresponding to low values of α) and spread along the length of an electrically long structure, the resulting radiation pattern can be highly directive. Combined with good radiation efficiency, very high gain antenna designs can be realized with simple feed mechanisms and frequency dependent beam scanning [14]. Antennas with these properties are particularly useful for radar and for high microwave and mm-wave frequencies which can suffer major

losses in overly complex feed networks [29]. Analysis and design techniques for LWAs will be outlined in this section. The following section (2.3) will introduce some existing LWAs with an emphasis on SIW based broadside scanning LWAs.

2.2.1 Uniform and Quasi-Uniform LWAs

Uniform LWAs are typically realized by introducing some uniform (longitudinally) radiating perturbation to some guided wave structure. In many cases this is realized by opening guiding structures, that are typically closed, to free space in order to allow radiation leakage to occur. As already was mentioned, such an opening will only radiate if the guiding structure supports a fast wave. The air filled rectangular waveguide (or in fact any air filled single conductor waveguide) can be used as an LWA in this fashion since $\beta < k_0$ for all frequencies (which can easily be verified using equation 2.3). In fact, the earliest LWAs to be realized were slitted rectangular waveguides where a longitudinal cut allowed radiation leakage along the waveguide length [30], [31]. As an interesting side note, in such antenna designs it was found much more recently that a simple uniform longitudinal slot results in modal solutions for the structure resembling a superposition of the fundamental waveguide mode and a "slot-mode" due to currents running along the inner wall of the slot. This in turn results in pattern degradation from simultaneously leaking modes [32]. In quasi-uniform LWAs, closely spaced radiators are introduced to the guiding structure however analysis remains unchanged in comparison to uniform LWAs [14]. This section outlines the relevant theory of operation for these types of LWAs. It will be seen in the next section that much of this theory can be easily adjusted to suit the needs of periodic LWA analysis.

A typical line source uniform/quasi-uniform LWA model is shown in Figure 2.6. For simplicity assume that the LWA only radiates in the space above it.

The amplitude and phase of the wave traveling along the longitudinally uniform LWA ($V(y)$) can be fully described by the leaky-wavenumber $k_{LW} = \beta - j\alpha$ using the expres-

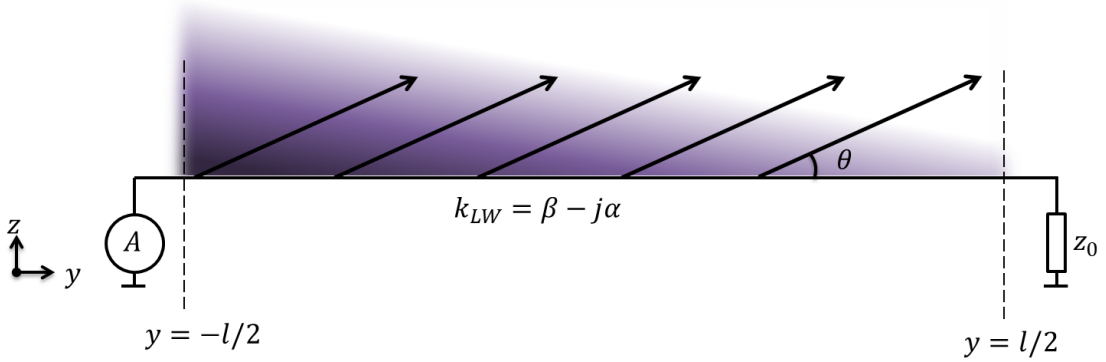

Figure 2.6: Line source uniform LWA model

sion [14]:

$$V(y) = Ae^{-jk_{LW}} = Ae^{-j\beta y}e^{-\alpha y}. \tag{2.11}$$

This expression defines an aperture field distribution for the open structure which can be used to calculate a theoretical radiation pattern for the antenna by applying a spatial Fourier transform. To compute the radiation pattern, the Fourier transform can be calculated as [14]:

$$f(\theta) = \int_{-l/2}^{l/2} e^{-jk_{LW}y}e^{jk_0 y\cos\theta}dy. \tag{2.12}$$

The result of the integral in equation 2.12 is:

$$f(\theta) = l\ \text{sinc}\left((\beta - j\alpha - k_0\cos\theta)\frac{l}{2}\right) \tag{2.13}$$

which indicates that the antenna radiation pattern depends primarily on its length and the leaky wavenumber.

The LWA length should ideally be designed such that 90–95% percent of power is radiated, with the remainder dissipated in a matched load termination. Exceeding 90–95% can result in an unnecessarily long antenna while a significantly shorter antenna would not be efficient.

For a known α the ideal antenna length for 90% radiated power can be calculated from [14]:

$$\frac{P(l)}{P(0)} = e^{-2\alpha l} = 0.1, \tag{2.14}$$

which can be rearranged to write the antenna length in terms of free space wavelengths as

$$\frac{l}{\lambda_0} \approx \frac{0.18}{\frac{\alpha}{k_0}}. \tag{2.15}$$

The antenna electrical length is therefore dictated by α which therefore also dictates the following beamwidth approximation [14]:

$$\triangle\theta \approx \frac{1}{\frac{l}{\lambda_0} cos\theta_{max}}. \tag{2.16}$$

With a known k_{LW} the main beam angle may also be simply approximated using [14]:

$$\cos(\theta_{max}) \approx \frac{\beta}{k_0}. \tag{2.17}$$

The above equations enforce two main ideas in terms of design, the first being that the aperture field amplitude distribution (and thus the directivity and side lobe levels) is primarily controlled by the leaky wave attenuation coefficient α , and the second that the main beam angle is primarily determined by the leaky wave phase constant β. With careful design of α LWAs can be designed to offer very high directivity patterns (which easily translate to high gains due to the simple feed mechanism of LWAs), while the frequency dependence of β/k_0 ensures frequency dependent beams scanning (as approximated by equation 2.17).

A popular alternative to LWAs for high gains and frequency dependent beam scanning are phased arrays. A serious drawback to phased arrays however is that the feed networks can be extremely complex, thus dissipating signal strength and degrading the overall antenna efficiency [6]. As was mentioned previously, this is especially true for higher microwave and

mm-wave frequencies where power lost to feed networks can be very high.

2.2.2 Periodic Leaky-Wave Antennas

Periodic LWAs are similar to uniform LWAs in that they are traveling wave antennas that "leak" radiation along their length. The difference lies in the fact that for periodic LWAs, radiating perturbations are placed periodically along the guiding structure rather than uniformly along the entire length. Periodic LWAs therefore resemble series fed traveling wave arrays, and in fact could in some cases be modeled as such. In [14] it is stated that the primary difference between a traveling wave array and a periodic LWA is the resonance of the radiating elements. In LWAs the elements should weakly load the guided mode (and thus are intentionally made non-resonant) so that the antenna can be viewed as a wave guiding structure with a complex propagation constant (k_{LW}). For traveling wave arrays the elements are often made resonant and it is best to approach analysis differently as shown in [33]. Periodic LWAs differ from quasi-uniform LWAs in that the radiating perturbations are spaced relatively far apart (on the order of a wavelength) which allows them to scan from reverse to forward endfire. Backward scanning can be understood in principle from array theory, where in equally spaced arrays, the beam pointing direction will be towards the phase lagging element, which is not possible with closely spaced series fed elements (unless using the CRLH LWA technique) [1]. Periodic LWAs cannot however radiate at broadside without special design techniques, the reason for which will be described towards the end of this section.

Periodic LWA analysis makes use of much of the foundation laid by uniform LWA analysis. Figure 2.7 depicts a typical linear periodic LWA model with element spacing s and leaky-wavenumber $k_{LW} = \beta_{-1} - j\alpha$ (the significance of the -1 subscript on β will be explained shortly). The antenna has a length $l = M \cdot s$ where M is the number of radiating elements.

Analysis of periodic structures generally hinges upon the observation that although the continuous field variation in the longitudinal direction cannot be modeled as a simple expo-

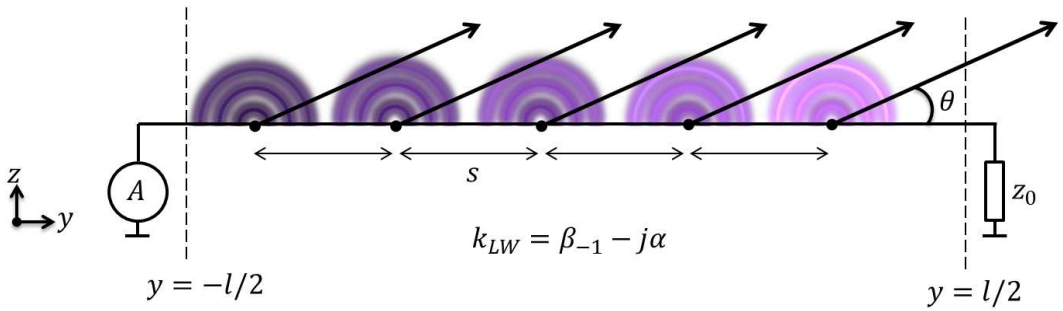

Figure 2.7: Linear periodic LWA model

nential function, the envelope of periodic field samples can [34], i.e.

$$V(y + ms) = e^{-jk_{LW}ms}V(y),\ m = \pm 1, \pm 2, ... \tag{2.18}$$

where m is the index of the m^{th} of M unit-cells (or elements in a periodic LWA).

Now, it is evident from equation 2.18 that the phase shift between some location y on the periodic structure, and a location $y + s$ away, is given by $\beta \cdot s$ and the amplitude difference is given by $e^{-\alpha \cdot s}$. Now, imagine that the magnitude difference and phase shift over distance s (i.e. $|V(y + s)|/|V(y)| = c$ and $\angle(V(y + s)/V(y)) = \phi$ respectively) were measured for an arbitrary infinitely extending periodic structure. From these measurements one could calculate the attenuation coefficient as:

$$e^{-\alpha s} = c\alpha = -\frac{\ln(c)}{s}, \tag{2.19}$$

and a phase constant β_0 as

$$\beta_0 = \frac{\phi}{s}. \tag{2.20}$$

This phase constant however does not account for the fact that ϕ for such a measurement is actually an indeterminate quantity for an arbitrary structure due to the fact that $\phi + n2\pi$, where n is any integer, would yield the same phase shift (i.e. $e^{-j\phi} = e^{-j(\phi+n2\pi)}$). Therefore

an infinity of phase constants are defined by:

$$\beta_n = \frac{\phi + n2\pi}{s} = \beta_0 + \frac{n2\pi}{s}. \tag{2.21}$$

Each phase constant β_n belongs to the n^{th} space harmonic (or Floquet mode) of the periodic structure, all of which exist simultaneously [34], [14]. The attenuation coefficient is the same (α) for all space harmonics (Floquet modes). If the n^{th} space harmonic is a fast wave at some frequency (i.e. $|\beta_n| < k_0$ or $|\beta_n/k_0| < 1$) it will radiate and the associated phase constant will dictate the radiating angle, approximated by:

$$\cos(\theta_{max}) \approx \frac{\beta_n}{k_0}. \tag{2.22}$$

From equation 2.21 it is evident that for a slow wave structure with $|\beta_0/k_0| > 1$ that radiation can be induced from space harmonics with negative values of n and appropriate periodicity s. A typical design problem is to ensure only one space harmonic (usually $n = -1$) is radiating within the desired operating frequency range. To do so the element spacing s and the $n = 0$ mode phase constant β_0 must be properly designed to satisfy [9]:

$$|\beta_{-1}| = \left|\beta_0 - \frac{2\pi}{s}\right| < k_0 \tag{2.23}$$

which can be rewritten as

$$-k_0 < \beta_{-1} < k_0 \tag{2.24}$$

in order to ensure the $n = -1$ mode is fast and radiating. Also, to avoid simultaneous radiation from the $n = -2$ space harmonic (which would cause a grating lobe to appear):

$$\beta_{-2} = \beta_{-1} - \frac{2\pi}{s} < -k_0, \tag{2.25}$$

which leads to a second condition on β_{-1}:

$$\beta_{-1} < -k_0 + \frac{2\pi}{s}. \tag{2.26}$$

In order to enable reverse endfire to forward enfire scanning (corresponding to $\beta_{-1} = -k_0$ and $\beta_{-1} = k_0$ using equation 2.22) of the $n = -1$ mode without grating lobes, $\beta_{-1} = k_0$ must satisfy condition 2.26 [9], i.e.

$$\beta_{-1} = k_0 < -k_0 + \frac{2\pi}{s}, \tag{2.27}$$

which can be reduced to

$$s < \frac{\lambda_0}{2}. \tag{2.28}$$

This result is consistent with array theory stating that if radiating element spacing is greater than a half wavelength, grating lobes appear in the array factor [1]. Thus for a single beam periodic LWA, element spacing must be chosen such that the $n = -1$ space harmonic is fast while simultaneously ensuring that the spacing is less than half of a free space wavelength at the highest operating frequency.

The design variables available to manipulate β_{-1} and β_{-2} at a particular frequency are s and β_0, where β_0 depends on the periodic structure geometry and materials. Assuming some arbitrary periodic LWA can be modeled as a TEM transmission line with fundamental mode phase constant $\beta_0 = \frac{\sqrt{\epsilon_e}\omega}{c}$, it can be shown that the effective relative permittivity ϵ_e (assuming a relative magnetic permeability of unity) of such a structure would have to be greater than nine in order to allow full space grating lobe free scanning [14]. This is a fairly accurate approximation for microstrip based periodic LWAs with radiating elements that weakly load the guided mode, and is a result of the requirement of element spacing being less than half a free-space wavelength at the highest operating frequency.

The method of proving this permittivity requirement (reported in [14]) was provided in [19] and is as follows. Firstly the phase constants of the first two radiating space harmonics can be normalized in terms of the free space wavenumber and written as:

$$\frac{\beta_{-1}}{k_0} = \frac{\sqrt{\epsilon_e}\omega}{k_0 c} - \frac{2\pi c}{\omega s} \tag{2.29}$$

and

$$\frac{\beta_{-2}}{k_0} = \frac{\sqrt{\epsilon_e \omega}}{k_0 c} - \frac{4\pi c}{\omega s}. \tag{2.30}$$

Then $\beta_{-1}/k_0 = 1$, which corresponds to forward endfire radiation of the $n = -1$ space harmonic, should occur at a lower frequency than $\beta_{-2}/k_0 = -1$, which corresponds to reverse endfire radiation of the $n = -2$ space harmonic (and thus the appearance of grating lobes). So, solving the above expressions to find the frequency at which the $n = -2$ mode becomes fast and the $n = -1$ mode becomes slow, i.e.

$$\omega_{-2\text{Fast}} = \frac{4\pi c}{s\left(\sqrt{\epsilon_e} + 1\right)} \tag{2.31}$$

and

$$\omega_{-1\text{Slow}} = \frac{2\pi c}{s\left(\sqrt{\epsilon_e} - 1\right)} \tag{2.32}$$

and enforcing the inequality:

$$\omega_{-2\text{Fast}} > \omega_{-1\text{Slow}} \tag{2.33}$$

simplifies to the effective permittivity requirement

$$\epsilon_e > 9. \tag{2.34}$$

This requirement is presented visually in the dispersion diagram of Figure 2.8 for a periodic LWA with broadside radiation at $f_b = 10$ GHz and an effective permittivity of $\epsilon_e = 9$. The β_n curves with positive slopes indicate forward traveling waves while the corresponding curves with negative slopes indicate reverse traveling waves. The figure shows the "fast-wave" region, within which a space harmonic with $|\beta_n| < k_0$ will radiate at an angle $\cos(\theta_{max}) \approx \frac{\beta_n}{k_0}$. The frequency range within which the $n = -1$ space harmonic radiates is labelled (1) on the diagram, above which region (2) indicates the fast-wave/radiating region of the $n = -2$ space harmonic. As predicted by the condition $\epsilon_e > 9$, the theoretical periodic LWA with $\epsilon_e = 9$ results in the $n = -1$ space harmonic leaving the fast-wave (radiating) region at exactly the frequency at which the $n = -2$ space harmonic enters the fast-wave (radiating) region. This allows the $n = -1$ space harmonic to sweep the entire range of beam angles, from reverse to forward endfire, as β_{-1} sweeps from $-k_0$ to k_0, without radiation from the $n = -2$ space harmonic. If the permittivity were any lower the fast wave regions would overlap and grating lobes would appear.

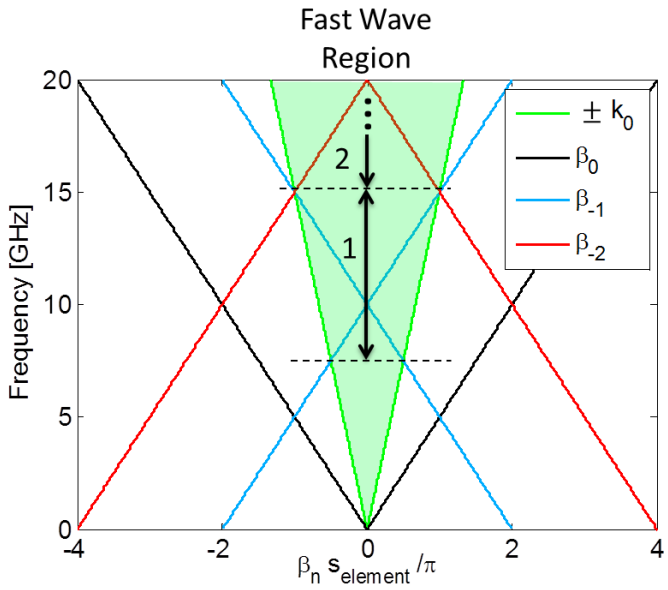

Figure 2.8: Theoretical TEM transmission line based periodic LWA dispersion diagram with $\epsilon_e = 9$ and $f_b = 10$ GHz

This condition is more stringent for non-TEM single conductor waveguides which have

dispersive properties that depend on both the material filling the waveguide and the waveguide geometry (which in turn defines its cutoff frequency). In Appendix C it is shown that the minimum permittivity requirement for a waveguide based periodic LWA can be calculated for a desired broadside frequency to cutoff frequency ratio. In order to illustrate the worsening of the permittivity requirement for non-TEM waveguide based periodic LWAs, the dispersion diagram for a rectangular waveguide (or SIW) fed periodic LWA with $f_b = 10$ GHz broadside radiation, assuming negligible mode perturbation by periodic elements, is shown in Figure 2.9. The waveguide cutoff was set to $f_c = 6$ GHz and a dielectric filling with $\epsilon_r = 9$ was used (consistent with the TEM transmission line based periodic LWA model shown in Figure 2.8).

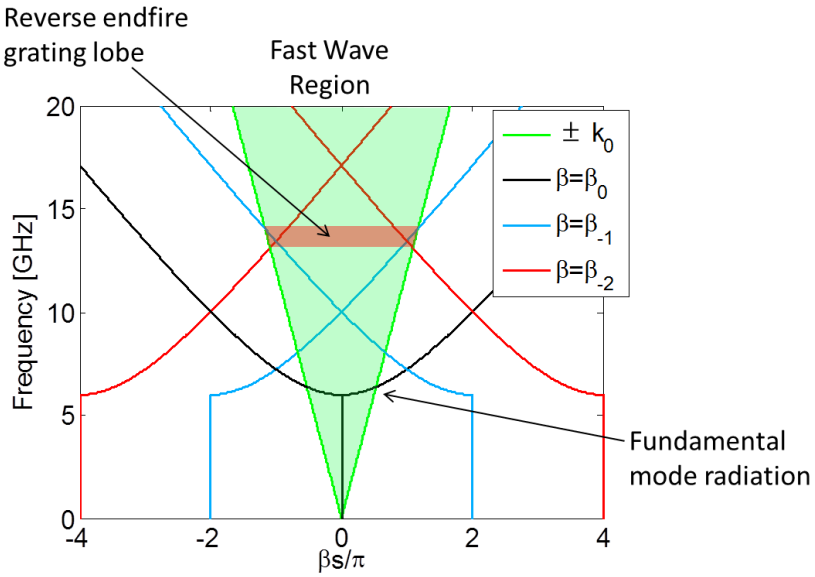

Figure 2.9: Theoretical rectangular waveguide based periodic LWA dispersion diagram with $\epsilon_r = 9$, $f_b = 10$ GHz and $f_c = 6$ GHz. Note that β becomes imaginary below waveguide cutoff and so what is shown on the graph is actually the real part of β.

In Figure 2.9 it is observed that the $\epsilon_r = 9$ permittivity requirement for grating lobe free scanning is insufficient for the waveguide, indicated by the shaded region labeled "reverse endfire grating lobe" which provides a frequency range within which both the $n = -1$ and $n = -2$ space harmonics radiate. Also, the fundamental waveguide mode radiates near cutoff (which is not the case for TEM transmission lines) and so the $n = -1$ mode must begin

backfire radiation at a higher frequency than the frequency at which the fundamental mode reaches forward endfire.

The uniform LWA analysis provided in Section 2.2.1 is applicable to periodic LWAs provided that the correct phase constant $\beta = \beta_n$ (usually β_{-1}) for the space harmonic of interest is used in the equations [14].

An additional technique for pattern prediction available to periodic LWAs is the computation of an array factor which can be used in conjunction with the unit-cell radiation pattern to calculate a theoretical antenna pattern [35]. The array factor is essentially the antenna pattern assuming isotropic radiating elements [1]. The analysis is as follows. Firstly, let us define the radiation magnitude and phase of the m^{th} of M elements as [9]:

$$V_m = e^{-jk_{LW}((m-1)s-l/2)},\ m = 1, 2, ..., M, \tag{2.35}$$

where $k_{LW} = \beta_{-1} - j\alpha$. Note that using any n^{th} space harmonic phase constant β_n in the expression would result in the same relative phase shift between elements, and thus any could be used. Then, the array factor can be calculated as [35], [9]:

$$AF(\theta) = \sum_{m=1}^{M} V_m e^{jk_0(m-1)s\cos\theta}. \tag{2.36}$$

Now, it is well known that a potential difficulty with periodic LWAs is that without special design techniques they will generally exhibit an open-stopband at the broadside frequency. An open-stopband is a frequency band of an open (or radiating) structure where traveling wave behavior is diminished and replaced with standing wave behavior and a high VSWR corresponding to a poor input impedance match. This is can be explained as a "mode-coupling" effect of the forward and reverse traveling $n = -1$ Floquet modes (space harmoincs) [36]. A more intuitive approach to understanding the problem is through the simple example shown in Figure 2.10.

For the periodic structure, the input admittance at the broadside frequency is simply the

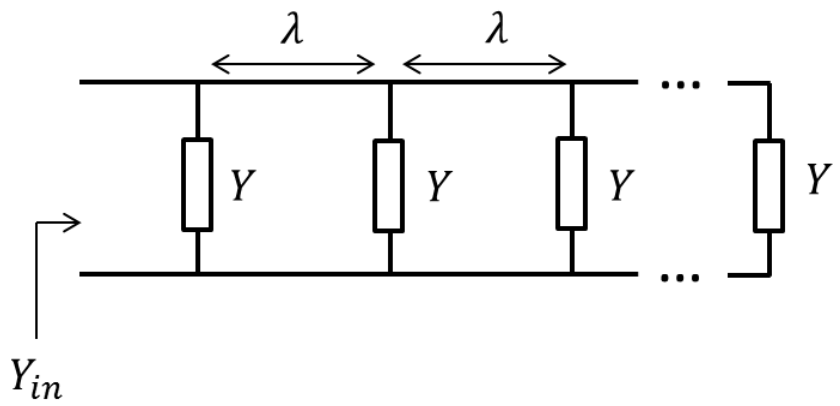

Figure 2.10: Periodic structure with shunt radiating elements

number of elements (say M) multiplied by the element admittance Y due to the wavelength periodicity at broadside. The input admittance as the number of elements M approaches infinity becomes that of a short circuit, diminishing the input impedance match and therefore radiated power. This is in effect the open-stopband problem observed in periodic LWAs. The input impedance of an infinite periodic structure is often called the Bloch impedance [24] (Z_B^+ and Z_B^- for forward and reverse traveling waves, respectively, outlined in Appendix A). One technique used to address the open-stopband problem is to add a matching section to each unit-cell in order to force the input impedance of a unit-cell to equal the characteristic impedance of the transmission line feeding/terminating the periodic structure at the broadside frequency. With a perfect input match, the unit-cell reflection for a forward traveling wave is reduced to zero (i.e. $S_{11} = 0$). It can be shown by substituting $S_{11} = 0$ into the Bloch impedance calculation in Appendix A that the input impedance of an infinite periodic structure for forward traveling waves reduces to the unit-cell terminal impedance (i.e. $Z_B^+ = Z_0$). Similarly if the unit-cell S_{22} is zero the impedance looking into the output of the periodic structure reduces to the unit-cell terminal impedance (i.e. $Z_B^- = Z_0$). Therefore in order to eliminate the open-stopband of a forward traveling wave periodic LWA, it is sufficient to minimize the unit-cell S_{11} at the broadside frequency through the use of a matching network. This technique for open-stopband mitigation was first realized in microstrip based periodic

LWAs presented in [15] and [16].

2.2.3 The Periodic Phase-Reversal LWA

In Chapter 3 of this thesis the proposed periodic LWA with broadside radiation enabled by unit-cell matching networks is presented, along with a periodic phase-reversal version of the antenna. In order to introduce the theory behind periodic phase-reversal LWAs it is useful to explore an example. For this reason a well known stripline fed periodic phase-reversal LWA proposed by Yang et al. [19] is outlined in this section. It will be shown that through periodic phase-reversal of radiating elements in a periodic LWA, the antenna size can be reduced and the grating lobe free scan range can be increased, for a given substrate permittivity.

Figure 2.11 depicts the stripline periodic phase-reversal architecture and concept proposed in [19]. The structure consists of laterally offset stripline on a substrate (+ indicating top layer conductor strip and − indicating bottom layer conductor strip) with periodic radiating perturbations that were realized by inverting the stripline lateral offset. The offset inversion results in radiation proportional to unbound current labelled I_{rad}. It is also shown in the figure that with in-phase radiating element excitation (indicated by λ separation) the radiating currents are out-of-phase due to the periodic phase-reversal of the radiating elements (which can be interpreted as an additional 180° phase shift per unit-cell). The out-of-phase radiating currents would result in a radiation null at broadside. Therefore in order to realize broadside radiation from a periodic phase-reversal LWA, elements should be spaced at half a guided wavelength at the desired broadside frequency, which is shown in Figure 2.11 as having in-phase radiating currents. [19]

Now, as with the conventional periodic LWA, the radiating properties of the structure are defined by the leaky-wavenumber k_{LW}. For the periodic phase-reversal LWA, computation of β_n requires some additional interpretation due to the spatially discrete 180° phase shift per unit-cell induced by the successive element phase-reversal. Interpreting the phase-reversal

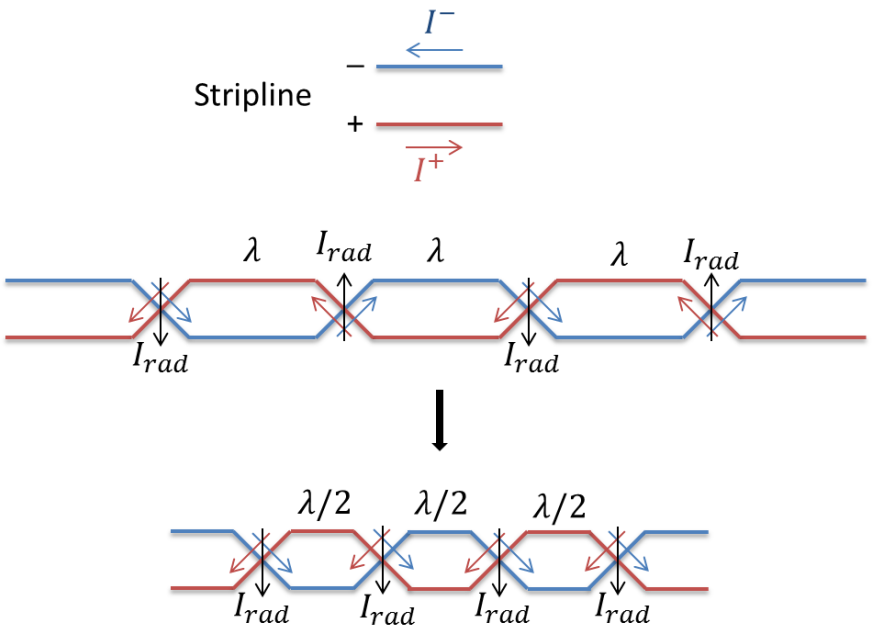

Figure 2.11: Stripline periodic phase-reversal antenna proposed by Yang et al.

as being positive, the phase constant of the n^{th} space harmonic can be written as [19]:

$$\beta_n = \pm\left(\beta_0 + \frac{(2n+1)\pi}{s}\right),\ n = 0 \pm 1, \pm 2... \tag{2.37}$$

such that the $n = -1$ space harmonic can be designed to radiate with proper element spacing. Conventional periodic LWA analysis can then be applied to the structure. The sign of β_n indicates forward and reverse traveling waves (positive and negative, respectively).

Now, it was shown previously that for an arbitrary periodic LWA modeled as a lossy unperturbed TEM transmission line that the effective permittivity would have to be greater than 9 to enable grating lobe free scanning from reverse to forward endfire. With the periodic phase-reversal architecture the permittivity requirement is relaxed due to the reduced radiating element separation (half a broadside guided wavelength rather than a full broadside guided wavelength) [19]. To prove this, again assume the antenna can be modeled as a

TEM transmission line with:

$$\beta = \frac{\sqrt{\epsilon_e}\omega}{c}, \tag{2.38}$$

$$\frac{\beta_{-1}}{k_0} = \frac{\sqrt{\epsilon_e}\omega}{k_0 c} - \frac{\pi c}{\omega s}, \tag{2.39}$$

and

$$\frac{\beta_{-2}}{k_0} = \frac{\sqrt{\epsilon_e \omega}}{k_0 c} - \frac{3\pi c}{\omega s}. \tag{2.40}$$

Then, $\beta_{-1}/k_0 = 1$, which corresponds to forward endfire radiation of the $n = -1$ space harmonic, should occur at a lower frequency than $\beta_{-2}/k_0 = -1$, which corresponds to reverse endfire radiation of the $n = -2$ space harmonic (and thus the appearance of grating lobes). So, solving the above expressions to find the frequency at which the $n = -2$ mode becomes fast and the $n = -1$ mode becomes slow, i.e.

$$\omega_{-1Slow} = \frac{\pi c}{s\left(\sqrt{\epsilon_e} - 1\right)} \tag{2.41}$$

and

$$\omega_{-2Fast} = \frac{3\pi c}{s\left(\sqrt{\epsilon_e} + 1\right)} \tag{2.42}$$

and enforcing the condition $\omega_{-2Fast} > \omega_{-1Slow}$ for grating lobe free scanning, it can easily be shown that [19]:

$$\epsilon_e > 4. \tag{2.43}$$

The periodic phase-reversal LWA can therefore be realized using transmission lines with a much lower substrate permittivity than otherwise possible. A conventional periodic LWA

with the same substrate permittivity, broadside frequency, and number of radiating elements would have to be twice as long (in theory, assuming negligible guided mode perturbation) due to full wavelength element separation at broadside and the scan range would become limited by the appearance of grating lobes (since $\epsilon_e < 9$).

This reduction in the effective permittivity requirement for the periodic phase-reversal LWA is verified visually through the example dispersion diagram shown in Figure 2.12. The associated TEM transmission line modeled periodic LWA has broadside radiation at 10 GHz and an effective permittivity of $\epsilon_e = 4$. As mentioned previously, β_n curves with positive slopes indicate forward traveling waves while the corresponding curves with negative slopes indicate reverse traveling waves, and when within the "fast-wave" region, the corresponding space harmonic will radiate with a main beam angle given by $\cos(\theta_{max}) \approx \beta_n/k_0$. As predicted by the condition $\epsilon_e > 4$, the theoretical periodic phase-reversal LWA with $\epsilon_e = 4$ results in the $n = -1$ space harmonic leaving the fast-wave (radiating) region at exactly the frequency at which the $n = -2$ space harmonic enters the fast-wave (radiating) region.

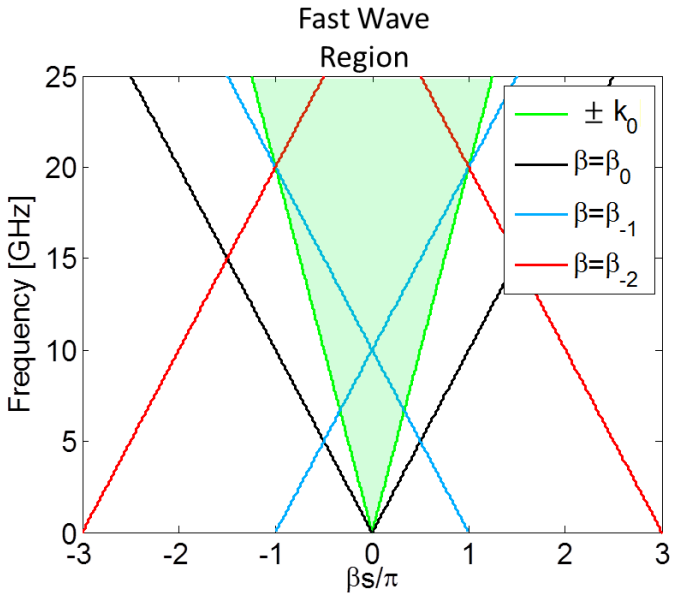

Figure 2.12: Theoretical TEM transmission line based periodic phase-reversal LWA dispersion diagram with $\epsilon_e = 4$ and $f_b = 10$ GHz

As was the case for conventional periodic LWAs, this condition is again more stringent

for waveguide based transmission lines, particularly when operating near cutoff. Appendix C outlines minimum permittivity requirements, that are waveguide based periodic and periodic phase-reversal LWA specific, for grating lobe free scanning given a desired broadside to cutoff frequency ratio f_b/f_c.

2.3 Existing SIW Broadside Scanning LWAs in Literature

In Section 2.2.2 of this chapter it was explained that periodic LWAs require specialized design techniques in order to be capable of broadside radiation. In actuality, this problem extends beyond the scope of periodic LWAs to include uniform/quasi-uniform LWAs as well. Various solutions to the broadside radiating problem have been realized for fundamentally fast-wave uniform/quasi-uniform LWAs (e.g. center-feed with PRS [8], CRLH metamaterial [37]) as well as for fundamentally slow-wave periodic LWAs (e.g. unit-cell matching [15, 16], symmetric center feed [7, 9], dual-radiator unit-cell [38]).

Of particular interest in this thesis was identification of existing SIW based solutions to the broadside scanning LWA problem, such that gaps in the field of knowledge could be identified. Reviewed SIW broadside scanning LWAs using the CRLH metamaterial approach ranged from simple single layer structures [11, 39, 40], to more complicated multilayer structures [41]–[43], including circular polarized and polarization-flexible designs [44]–[45], as well as dual-band designs like the one in [46]. These works are just a sample of the SIW CRLH LWAs currently available in literature, alluding to how much attention the relatively new design technique has received.

Many other SIW based LWA types and designs offering wide scan ranges were reviewed, including non-CRLH uniform and quasi-uniform LWAs [47]–[50], as well as periodic LWAs [51]–[54], however none of these designs were able to produce broadside radiation. It quickly became clear that broadside scanning radiation from SIW based LWAs was almost exclusively accomplished through the use of the CRLH approach, with the only found ex-

ception being a periodic LWA in [17] that used dual radiator unit-cell technique proposed in [38] to mitigate the open-stopband at broadside.

Without going into too much detail, as it is outside the scope of this thesis, CRLH structures are metamaterials, meaning that they are designed to exhibit electromagnetic properties that are not commonly found in nature. For CRLH metamaterials, the effective permittivity and permeability of the structure is frequency dependent, and can become simultaneously negative, resulting in wave propagation with a negative phase velocity despite a positive group velocity [37]. The first LWA in literature to be designed using the CRLH transmission line approach in order to realize broadside scanning radiation was a microstrip based antenna outlined in [10]. It was soon after realized that some inherent properties of SIW (beyond the scope of this thesis) makes them very well suited for CRLH LWA design [11], which has at least partially driven the appearance of large numbers of CRLH LWAs in literature since that time.

A significant difference between CRLH LWAs and periodic LWAs is that the radiating mode of the CRLH LWA is the fundamental mode of the structure while the periodic LWA will typically radiate through the $n = -1$ Floquet mode (or space harmonic) [14] as was explained in Section 2.2.2. This difference is notable from the design perspective, however both CRLH and periodic LWAs (with open-stopband compensation) can in theory offer similar broadside scanning radiation performance. Despite this fact, SIW based periodic LWAs offering broadside scanning performance were observed to be practically non-existent in literature compared to the number of SIW based CRLH LWAs (see below).

SIW based traveling wave arrays were also reviewed to find any that might offer broadside scanning performance, however those that were found had resonant radiating elements, non-periodic features, and narrow scan ranges and thus could not be interpreted as broadside scanning periodic LWAs [55], [56].

As a result of this literature review, it was realized that only one SIW based periodic

LWA had been designed to enable broadside scanning radiation comparable to existing CRLH designs [17], and its open-stopband mitigation technique (proposed in [38]) has been reported as being inferior to the unit-cell matching technique (proposed in [15, 16]) that was outlined towards the end of Section 2.2.2. In addition, no existing SIW based LWA designs were found that made use of the periodic phase-reversal technique for antenna size reduction and/or substrate permittivity reduction.

Based on these observations, the antennas presented in this thesis (to the best of the author's knowledge) were the first to use the unit-cell matching technique in order to enable broadside scanning radiation in a SIW based periodic LWA [13]. Similarly, as will be seen in Chapter 3, one of the two antenna designs presented in this thesis seems to have been the first SIW based periodic LWA to make use of the periodic phase-reversal concept. After arriving at the proposed antenna architectures it was also realized that they were the first and only SIW based broadside scanning LWAs to offer maximum radiation in the plane of the substrate.

2.4 Chapter Summary

The intention of this chapter was first to provide an introduction to relevant SIW and LWA theory, concepts, and design methodologies that will be used throughout the remainder of this thesis. Additionally, the review of existing mechanisms in literature by which LWAs have been enabled to radiate at broadside, and more specifically those mechanisms which have already been applied in SIW, was intended to summarize the broadside scanning SIW LWA field of knowledge as it was prior to the work in this thesis. In order to best understand the new antenna designs introduced in Chapter 3 and the value of the research leading to their invention, some key takeaways from this chapter are listed here:

- SIW and HMSIW analysis relies on a transformation to an equivalent rectangular waveguide which in turn can be modeled as a dispersive transmission line [23].

- LWA analysis relies on finding the leaky-wavenumber ($k_{LW} = \beta - j\alpha$) of the structure[14]. The technique used in this thesis is outlined in Appendix A and relies heavily on simulations outlined in Chapter 4.

- Periodic LWAs exhibit an open-stopband at broadside unless properly addressed. The technique used in this thesis to address the open-stopband is the unit-cell matching technique which essentially reduces the broadside frequency Bloch-impedance (which is approximately the input impedance for a long periodic structure) to be equal to the excitation/termination impedance Z_0 [15, 16].

- Periodic LWAs fed by TEM transmission lines (assuming negligible guided mode perturbation) require an effective relative permittivity greater than 9 to enable reverse to forward endfire scanning without the appearance of grating lobes from the $n = -2$ space harmonic [14]. This condition is even higher for non-TEM waveguides. For a desired broadside to cutoff frequency ratio f_b/f_c the exact theoretical relative permittivity condition for a non-TEM waveguide can be calculated as shown in Appendix C.

- Periodic phase-reversal of radiating elements can be used to reduce element spacing. The reduced element spacing relaxes the required relative permittivity to greater than 4 for TEM transmission line fed full-space scanning periodic LWAs [19]. Again this condition is more stringent for non-TEM waveguides.

- Prior to the work in this thesis, no SIW based periodic LWAs had used the unit-cell matching technique to address the open-stopband condition at broadside. Also, it was seen that CRLH LWAs dominated the SIW based broadside scanning LWA field of knowledge (with only one exception found in literature [17]). The periodic phase-reversal technique for size and/or permittivity reduction had also never been used in an SIW based periodic LWA, and of the existing SIW based broadside scanning LWAs,

none had offered maximum radiation in the plane of the substrate.

Chapter 3

Proposed Antennas

In the previous chapter, foundations of the theory governing the design of SIW, broadside scanning periodic LWAs, and periodic phase-reversal LWAs was outlined. Additionally the current state of the SIW based broadside scanning LWA field of knowledge was summarized. In this chapter the proposed antenna architectures intended to expand this field of knowledge are revealed. Design parameters are introduced, however, techniques used to define parameter values will be explained in detail in the next chapter.

3.1 Proposed Antenna Geometries

The two new antenna architectures proposed in this thesis, referred to as the "Non-Inverting Element Antenna" and the "Periodic Phase-Reversal Antenna", are introduced in this section.

3.1.1 Non-Inverting Element Antenna Geometry

As was described in the previous chapter, periodic LWAs are generally realized through the introduction of periodic radiating perturbations to the guided mode of some structure such that the $n = -1$ Floquet mode becomes fast and radiating [14]. The non-inverting element periodic LWA architecture proposed uses HMSIW (as its guiding structure) to feed periodically spaced antipodal-tapered-slot-antenna (ATSA) elements (radiating perturbations) and is shown in Figure 3.1. The periodic structure geometry is primarily defined by its unit-cell parameters and the investigated antenna is 15 unit-cells in length. In order to obtain high gain performance, the ATSA elements were designed to weakly load the fundamental HMSIW guided mode in order to achieve slow leakage along the length of the antenna. These

characteristics are consistent with those recommended for analysis from the leaky wave perspective [14]. Traveling wave array analysis may also be applicable however is not of main interest in this thesis.

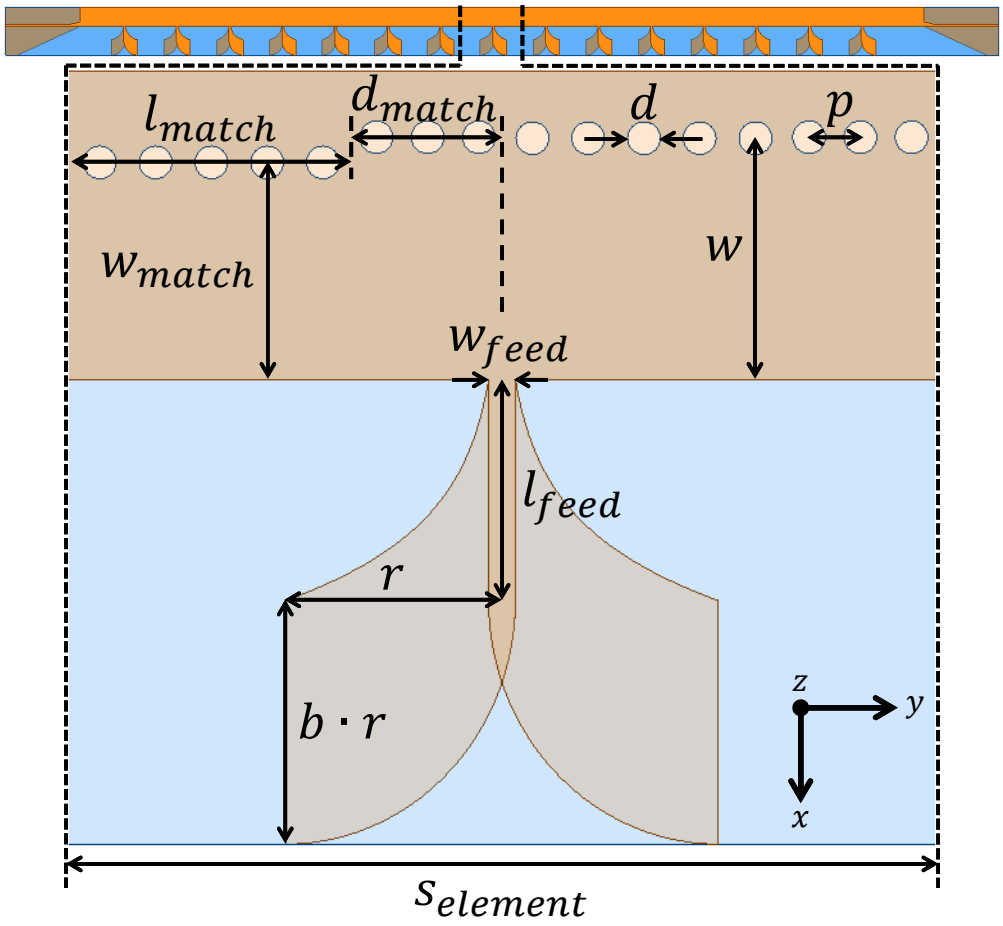

Figure 3.1: Non-Inverting Element Antenna Geometry (length units in mm): $p = 0.76$, $d = 0.508$, $w = 3.76$, $l_{match} = 4.31$, $w_{match} = 3.36$, $d_{match} = 2.34$, $w_{feed} = 0.42$, $l_{feed} = 3.42$, $r = 3.55$, $b = 1.06$, $s_{element} = 13.38$, $\epsilon_{rz} = 10.96$, $\epsilon_{rx} = \epsilon_{ry} = 13.3$

As was explained in the previous chapter, periodic LWAs generally exhibit an open-stopband at the broadside frequency [36]. The proposed antenna has matching sections added to the unit-cell of the periodic structure in order to enable broadside radiation from the scanning antenna [15] and [16]. To the author's knowledge, this architecture was the first SIW based LWA to use the unit-cell matching technique to enable broadside scanning radiation and thus offers verification of the portability of the technique to SIW based antennas [13]. For some, periodic LWA theory and design may be seen as relatively simple in comparison

to CRLH LWA theory and design, which is one reason this new design may be preferred to the alternative SIW broadside scanning LWA designs. In addition, other SIW broadside scanning LWAs produce maximum radiation in the space above and/or below the substrate plane and the proposed design was the first (again, to the author's knowledge) to offer maximum radiation in the plane of the substrate.

The remainder of this section is intended to be a brief overview of the relevance of each of the design parameters shown in Figure 3.1 while detailed design procedures for attaining exact values are provided in Chapter 4.

Appropriate selection of the substrate relative permittivity ϵ_r is crucial in the design of this periodic LWA. It has been shown that designing for a guided mode with a slower phase velocity offers beam scanning over a narrower bandwidth [40]. This in turn relaxes the bandwidth constraints on the periodic radiating element design and increases the beam scanning range to bandwidth ratio, as is usually preferred in high performance radar applications [40]. A slower phase velocity results in a reduced guided wavelength which is required to force element spacing to be close enough to avoid grating lobes up to the highest desired operating frequency (as was shown in Chapter 2) [14]. Assuming the antenna's fundamental mode phase velocity would be close to that of the guiding structure's, a high permittivity substrate was chosen to reduce the fundamental mode phase velocity in the HMSIW. In particular a Rogers RO3210 substrate with a bulk relative permittivity of 10.2 was used [57].

The structure used tapered microstrip for excitation and termination. The ground plane also had to be tapered to allow the introduction of the ATSA elements as shown in Figure 3.1. The operating range of the antenna was chosen to be within 8–12 GHz and so a simulated HMSIW cutoff of 6 GHz was deemed suitable. Parameters d, p and w in Figure 3.1 were chosen by modeling the HMSIW as a SIW with a width of $2w$ and using design equations from [23] for an equivalent X-band rectangular waveguide.

The ATSA element was chosen for its bandwidth, observed weak perturbation of the

fundamental HMSIW guided mode, as well as its radiating properties. Slots subtracted from the waveguide geometry were investigated as potential radiators however no slot configuration was realized that could offer weak guided mode perturbation in addition to adequate radiated power. The ATSA element geometry is shown in Figure 3.1, where each arm consists of a quarter section of an ellipse with axial ratio b that is fed by an exponential taper intersecting w_{feed} and r at a distance l_{feed} from the open sidewall of the HMSIW.

As was described in Chapter 2, the open-stopband observed in periodic LWAs can be understood as a frequency band where the reflections from each periodic perturbation (radiating element) add constructively in the reverse direction resulting in a standing wave on the structure and a poor input impedance match. According to [15] and [16] the individual reflections can be minimized at the broadside frequency with the use of unit-cell matching sections in order to ensure that the total reflection remains acceptably low. Matching was achieved by the addition of a reduced width section of HMSIW to the unit-cell, defined by w_{match}, l_{match}, and d_{match} in Figure 3.1.

3.1.2 Periodic Phase-Reversal Antenna Geometry

The periodic phase-reversal antenna architecture is parametrically identical to the non-inverting element design with some small changes in parameter values and the obvious successive inversion of adjacent radiating element polarity. The full antenna architecture can be viewed as a HMSIW feeding 20 periodically spaced ATSA elements. The non-inverting element architecture from the previous section is again shown in Figure 3.2 in order to help clarify the periodic phase-reversal architecture shown in Figure 3.2 (with phase-reversal indicated by the red/blue +/- signs). A matching section was included in the unit-cell of the periodic structure in order to enable broadside radiation that would otherwise be interrupted by an open-stopband [15], [16].

In essence, the polarity reversal of adjacent ATSA elements introduces a frequency independent 180° phase shift per unit-cell to radiated fields. As was described in Chapter 2

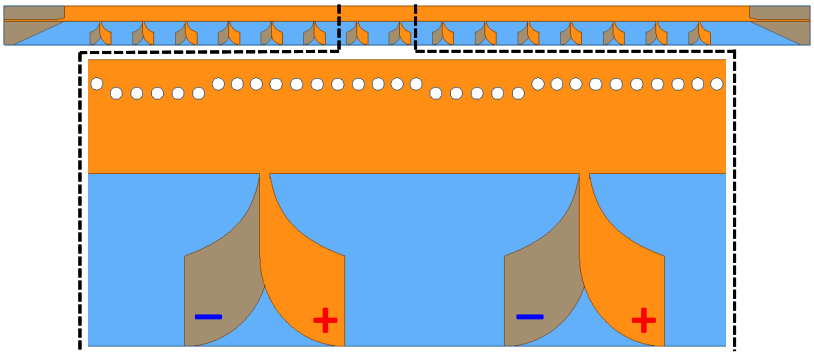

Figure 3.2: Phase polarity of the non-inverting element antenna

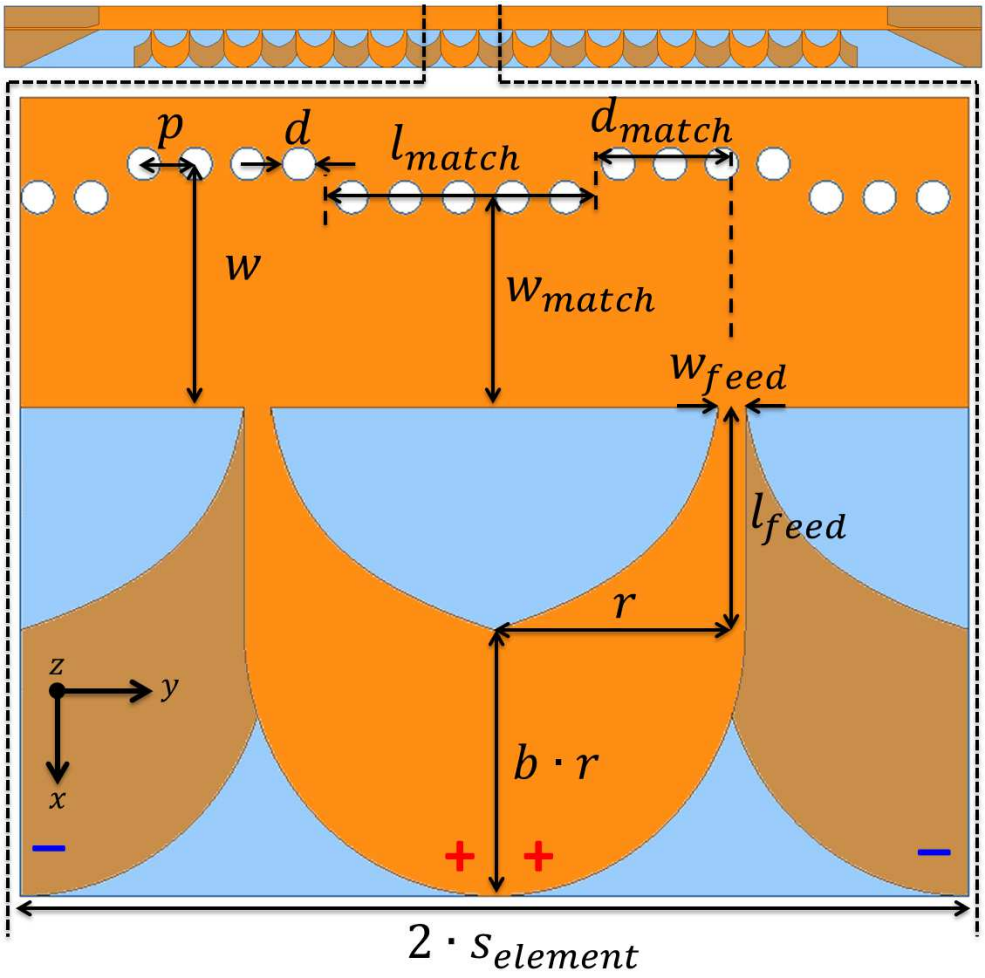

Figure 3.3: Periodic Phase-Reversal Antenna Geometry (length units in mm): $p = 0.76$, $d = 0.508$, $w = 3.76$, $l_{match} = 4.12$, $w_{match} = 3.24$, $d_{match} = 2.14$, $w_{feed} = 0.42$, $l_{feed} = 3.42$, $r = 3.86$, $b = 1.06$, $2 \cdot s_{element} = 14.58$, $\epsilon_{rz} = 10.96$, $\epsilon_{rx} = \epsilon_{ry} = 13.3$

for the offset stripline periodic phase-reversal LWA [19], the proposed architecture requires element spacing to be reduced to half a guided wavelength at the broadside frequency due to the additional 180° of phase per unit-cell (as is illustrated in Figure 3.4). The resulting architecture is compact in size and maintains similar radiating performance to the non-inverting element design. Furthermore, the reduced element spacing can allow the substrate permittivity to be reduced while maintaining grating lobe free scanning as will be shown in Chapters 4 and 5. Interpreting the phase shift as positive is consistent with the structure radiating through the $n = -1$ Floquet mode (or space harmonic), as described in [19], and implies periodic LWA analysis is suitable [14].

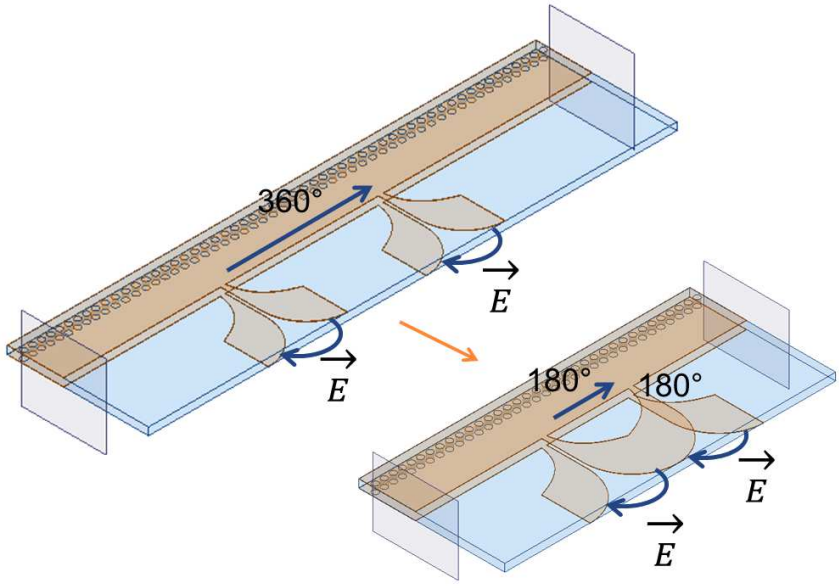

Figure 3.4: Periodic phase-reversal at the broadside frequency

As was mentioned in the previous section, the non-inverting element design was fabricated on a Rogers RO3210 substrate with a relative permittivity of 10.2 in order to ensure element spacing was small enough to avoid grating lobes over a wide scan range. In order to reduce fabrication costs, the periodic phase-reversal LWA was fabricated on the same Rogers RO3210 panel (the PCB vendor charged per panel and so an additional panel would have

doubled the cost). The anisotropic substrate permittivity values in Figure 3.3 were attained through Rogers directly. The chosen substrate permittivity was, however, unnecessarily high for the proposed periodic phase-reversal structure, was explained in Chapter 2 and is verified through simulations and measurements in Chapters 4 and 5.

3.2 Chapter Summary

In this chapter the proposed antenna architectures and design parameters were introduced. Key takeaways from this chapter are:

- Due to the simple planar antenna geometries, the proposed antennas can be manufactured using standard, single layer, PCB fabrication processes
- The principles of operation of the new antennas adhere to fairly rudimentary periodic LWA theory (as outlined in Chapter 2) and as such should be reasonably easily grasped by anyone with some background in antenna design
- The antennas make use of a unit-cell matching section in order to acquire broadside scanning radiation
- The antennas exhibit maximum radiation in the plane of the substrate (as might be predicted by the ATSA element orientation)
- A primary drawback of the non-inverting element geometry is the high substrate permittivity requirement for grating lobe free scanning
- This drawback is addressed by the periodic phase-reversal architecture

The proposed antennas therefore enable SIW based system level designers to choose a broadside scanning antenna with maximum radiation in the plane of the substrate. Also, the flexible design procedure (as will be seen in Chapter 4) may be preferable to some designers over the CRLH approach.

Chapter 4

Design and Theoretical Antenna Performance

This chapter describes in detail the design procedures that were used to arrive at the proposed antenna architectures introduced in Chapter 3. The design will be broken down into five parts numbered in Figure 4.1, corresponding to the first five sections of this chapter. The periodic phase-reversal architecture follows similar steps as the non-inverting element architecture and so a single section (4.4) is dedicated to outlining the key design differences. In section 4.6, leaky wave analysis of the structures using simulated data is presented which is used in section 4.7 to offer antenna pattern predictions for the two architectures. These predictions are compared to full antenna simulations and prototype measurements in Chapter 5. Where not otherwise specified, simulations were performed using ANSYS® HFSS (a commercial FEM solver for 3-D full-wave electromagnetic structure simulations).

Now, it is important to note that in designing the proposed antennas, we initially used the substrate permittivity from the Rogers RO3210 data-sheet labeled "bulk permittivity" $\epsilon_r = 10.2$ [57]. This turned out to be incorrect, as was discovered when fabricated prototype measurements exhibited a frequency shift of approximately 4% from initial simulations, shifting the broadside frequency from 10 GHz to 9.6 GHz. Investigating this problem revealed that the "design permittivity" of 10.8 on the substrate data-sheet was intended to be used in simulations. Furthermore, from direct communication with Rogers it was also revealed that the substrate exhibits significant permittivity anisotropy as well as some frequency dependence such that $\epsilon_{rz} = 10.96$ (out of the substrate plane) and $\epsilon_{rx} = \epsilon_{ry} = 13.3$ (in the substrate plane) are in fact much more accurate approximations in the X-band.

Fortunately, besides shifting the operating frequency, the antenna performances were largely unaffected. Also working in our favor was the fact that the 10 GHz broadside fre-

quency was chosen arbitrarily, and so the shift to 9.6 GHz was inconsequential. For these reasons, it was decided that the design process (which was of main importance) could be reasonably verified for the fabricated prototypes by re-computing simulations throughout the design steps using the correct substrate permittivity model, and a desired 9.6 GHz broadside frequency. For the sake of brevity, the incorrect simulations with substrate relative permittivity $\epsilon_r = 10.2$ are omitted from this chapter.

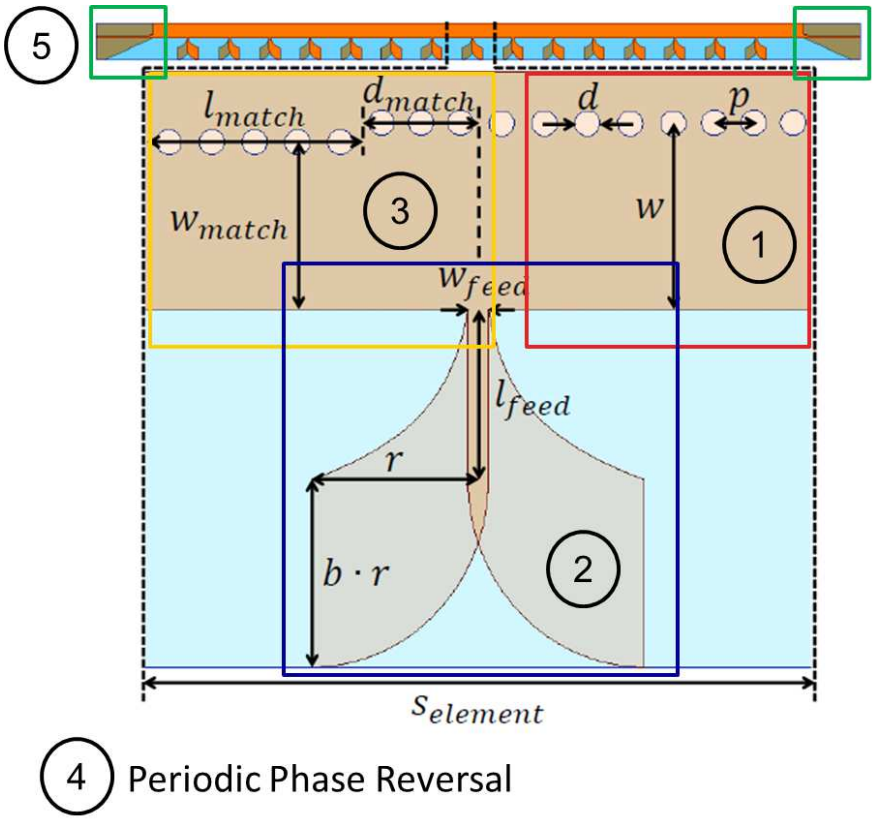

Figure 4.1: Antenna design breakdown

4.1 Half Mode Substrate Integrated Waveguide Design

The HMSIW geometry is defined by parameters d, p and w shown Figure 4.2. Using design equations outlined in Chapter 2, a rectangular waveguide with a desired cutoff frequency and dispersion characteristics can be transformed into an equivalent full SIW. The SIW can then be cut in half longitudinally to acquire HMSIW dimensions with a cutoff and dispersion

characteristics similar to the original rectangular waveguide. The dispersive properties were expected to change with the addition of radiating elements and matching sections to the periodic structure (loading the fundamental mode) and so ensuring the cutoff was well below the desired operating frequency range was deemed acceptable without designing for an exact value. In other words, the HMSIW design was analytical and approximate and then more precise dispersion properties were extracted from simulations without design iteration.

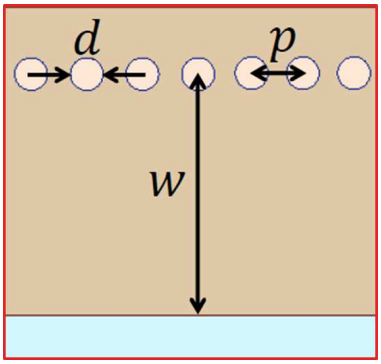

Figure 4.2: Half-mode substrate integrated waveguide design parameters

As was mentioned in the preamble to this chapter, the relative permittivity was thought to have been 10.2 and thus this value was used to acquire the dimensions of the HMSIW. An X-band HMSIW cutoff frequency (6.557 GHz [24]) was chosen to enable operation between 8-12 GHz.

As was outlined in Chapter 2, in order to be approximated by equivalent solid metal walls, via diameters must be less than $\lambda_g/5$ [26]. Assuming an upper frequency limit of 13 GHz, a cutoff frequency of 6.557 GHz, and a substrate relative permittivity of 10.2, the phase constant of such a waveguide at the upper frequency limit would be $\beta_{limit} = 751$ rads/m (from equation 2.3). The guided wavelength λ_g would then be approximately 8 mm, resulting in $d < 1.6$ mm. From the list of allowed diameters from the PCB vendor (Candor Industries), a via diameter of $d = 0.508$ mm was chosen which is well below the maximum allowed 1.6 mm. The center-to-center via separation must be less than $2d$ to avoid power leakage [26], thus $p = 1.5 \cdot d = 0.76$ mm was deemed acceptable.

Now, the width of a rectangular waveguide w_{eff} with a desired $TE_{1,0}$ cutoff frequency of 6.557 GHz and substrate permittivity $\epsilon_r = 10.2$ can be calculated from equation 2.4 as [24]:

$$w_{\text{eff}} = \frac{c}{2f_c\sqrt{\epsilon_r}} = 7.16\text{mm}. \tag{4.1}$$

Then an equivalent full SIW with a width $2w$ can be calculated as using equation 2.8 as [23]:

$$2w = w_{\text{eff}} + \frac{d^2}{0.95 \cdot p} = 7.51\text{mm}, \tag{4.2}$$

from which the HMSIW width was chosen to be $w = 7.51mm/2 = 3.76mm$. Some reduction in the cutoff frequency was expected due to fringing fields at the open side wall [27]. The cutoff was further reduced by the fact that the z directed substrate relative permittivity of 10.96 (assuming primarily z directed electric fields for the fundamental TE mode) was significantly higher than the relative permittivity used in the analytical design above (10.2). As was described in Chapter 2, HMSIW can be treated as a transmission line with longitudinal phase constant β [24]. The dispersion characteristics were therefore simulated in HFSS using the correct anisotropic permittivity model, the results of which are shown in Figure 4.3.

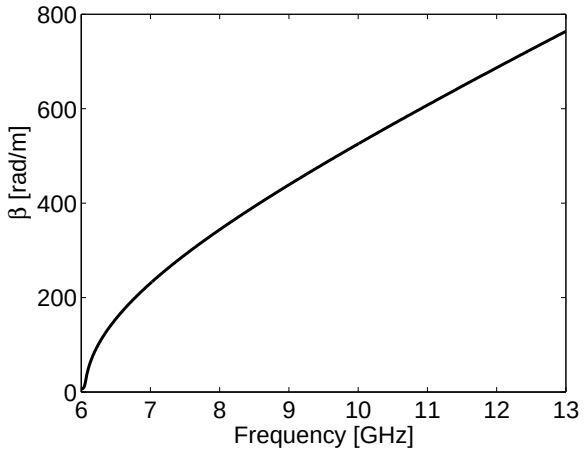

Figure 4.3: Simulated HMSIW dispersion with $\epsilon_{rz} = 10.96$, $\epsilon_{rx} = \epsilon_{ry} = 13.3$

A simulated cutoff frequency of approximately 6 GHz was observed as shown by the

dispersion curve of Figure 4.3. One problem with a reduced cutoff frequency is the possibility of the operating frequency extending above the cutoff of higher order modes. An interesting trait of HMSIW that can be quite beneficial in design is that HMSIW with a width w exhibits an exclusive fundamental mode operating frequency range 1.5 times that of a full SIW with a width $2w$ (i.e. the cutoff of the first spurious mode in HMSIW is three times the fundamental mode cutoff) [27]. The reduced 6 GHz cutoff was therefore not a concern for antenna operation between 8 and 12 GHz. The reduced cutoff did however affect performance by shifting the broadside frequency from 10 GHz to 9.6 GHz.

As was mentioned in the chapter preamble, the remainder of the design process (which is primarily simulation based) uses the more accurate anisotropic permittivity model and a desired broadside frequency of 9.6 GHz in order to clearly illustrate the design process.

4.2 Antipodal Tapered Slot Antenna (ATSA) Element Design

The periodic LWA design obviously requires periodic radiating elements. Several were investigated before an acceptable design was achieved including a variety of slot geometries and other element geometries external to the SIW guiding structure (like the ATSA element). The problem with most geometries was that the requirement of a broad impedance bandwidth (weakly loading the guided HMSIW mode), in addition to significant partial radiation of accepted power, was very difficult to satisfy. The ATSA element was finally investigated (inspired by designs presented in [58] and [59]) and found to exhibit a relatively broad pattern bandwidth, light loading on the guided mode (also over a broad bandwidth) as well as simple excitation from the open sidewall of the HMSIW. As depicted in Figure 4.4 each arm of the ATSA element is essentially a quarter section of an ellipse fed by an exponential taper, fully described by parameters r, w_{feed}, l_{feed} and ellipse axis ratio b.

The complexity of the HMSIW fed ATSA element was too high for analytical techniques to be developed, and therefore mature numerical design tools were employed. In particular,

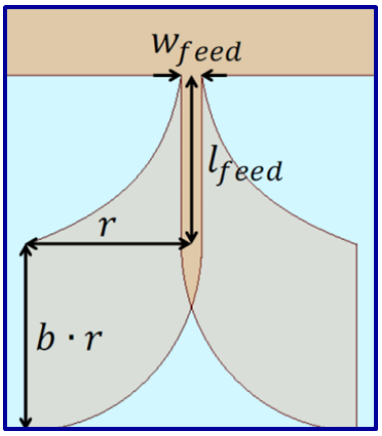

Figure 4.4: Half-mode SIW fed antipodal tapered slot antenna (ATSA) element geometry

HFSS was used to optimize the unit-cell ATSA element parameters from 8–12 GHz in terms of its return loss (to ensure an acceptable impedance bandwidth), beamwidth (to ensure a wide antenna scan range), and radiated power (to ensure distribution of radiated power across many unit-cells). The unit-cell simulation environment is shown in Figure 4.5.

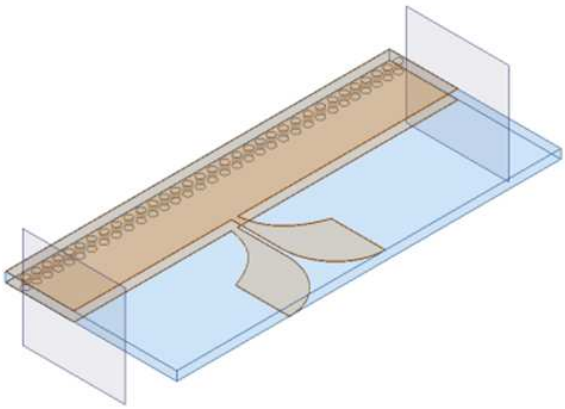

Figure 4.5: Unit-cell ATSA element HFSS simulation and optimization environment

Optimization in HFSS requires variables and their ranges to be defined (shown in Table 4.1) as well as cost function settings (shown in Table 4.2). Optimization algorithms manipulate the specified variable values to find the minimum of a cost function (defined in equation 4.3). In order to define the cost function, let G be the number of goals (or calculations as shown in Table 4.2), N_j be the number of range points for the j^{th} goal, W_j be the weight factor of the j^{th} goal, and e_i be the error contribution from the j^{th} goal at the

i^{th} range point. The cost function may then be expressed as shown in equation 4.3 and is essentially a weighted sum of the goal errors. [60]

$$Cost = \sum_{j}^{G} \frac{W_j}{N_j} \sum_{i}^{N_j} e_i \tag{4.3}$$

Table 4.1: ATSA Optimization Variables

Variable	Minimum	Maximum
l_{feed}	1 mm	5 mm
r	2 mm	6.5 mm
b	0.2	2
w_{feed}	0.2 mm	2 mm

Table 4.2: ATSA Optimization Cost Function Settings

Calculation	Range	Goal	Weight
Return Loss	8-12 GHz (1 GHz step)	≤ -12 dB	1
Insertion Loss	8-12 GHz (1 GHz step)	$= -1.4$ dB	1
Normalized Pattern	8-12 GHz (1 GHz step) for $\theta = 90°$ and $-45° < \phi < 45°$ (1 degree step)	≥ -3 dB	90

The normalized pattern calculation (used as a goal to achieve a 90° 3 dB beamwidth) in Table 4.2 has a weight factor of 90 because there are 90 times more range points (90 ϕ angles for each frequency) than for the return loss and insertion loss calculations. From equation 4.3 it is evident that more range points reduces the equivalent weight of each point by a factor of the number of points N_j. The variable domains in Table 4.1 were given a large degree of freedom to find a geometry offering acceptable performance.

A problem often associated with optimization is convergence on a local rather than global minimum of the cost function. For this reason a genetic algorithm based optimization was conducted which according to [60] is a stochastic optimizer which, at the expense of many random solutions, has the benefit of jumping out of local minima. A sequential non-linear

programming optimization [60] was then conducted using the genetic algorithm results as the starting point to fine tune the result. It is likely that in combining the two optimization algorithms that a global minimum of the cost function was reached (within the variable domains). Note that in general the cost function should be tailored to the needs of the designer. For example a higher gain LWA should have less radiation per unit-cell (to increase the antenna aperture) and if a narrower scan range is acceptable the gain can be increased by increasing the element directivity in the desired scan range.

The result of the optimization was parameter values $w_{feed} = 0.42$ mm, $l_{feed} = 3.42$ mm, $r = 3.55$ mm, and $b = 1.06$. Optimization was preferred over full parameter characterization due to the interdependence of the four design parameters, however single variable parametric sweeps were conducted after optimization to investigate their individual impacts on performance. The results of the parameter investigation are described qualitatively in Table 4.3.

Table 4.3: ATSA parameter impact on unit cell radiating and impedance performance

Parameter increased	Unit-cell effects
w_{feed} (0.1 mm to 0.7 mm)	Increases accepted power radiated per unit-cell at the cost of reduced unit-cell impedance bandwidth and beamwidth
l_{feed} (1 mm to 6 mm)	Decreases center frequency of unit-cell impedance match from greater than 12 GHz to less than 8 GHz
r (2 mm to 5 mm)	Decreases lower radiating cutoff frequency
b (0.2 to 1.3)	Increases unit-cell bandwidth at the cost of decreased beamwidth

Unit-cell S-Parameter simulations after optimization are shown in Figure 4.6 where a minimum 10dB return loss was observed between 8 and 12 GHz. The simulated radiated power per unit-cell varied from 6% at 8GHz to 22% at 12 GHz, indicating that a large number of radiating elements would be required for efficient radiation in the lower frequency range of the antenna. Simulation results predicted a minimum 3dB beamwidth between 65

and 100° in the $x - y$ plane (limiting the expected gain of scan angles approaching reverse or forward endfire) as shown in Figure 4.7.

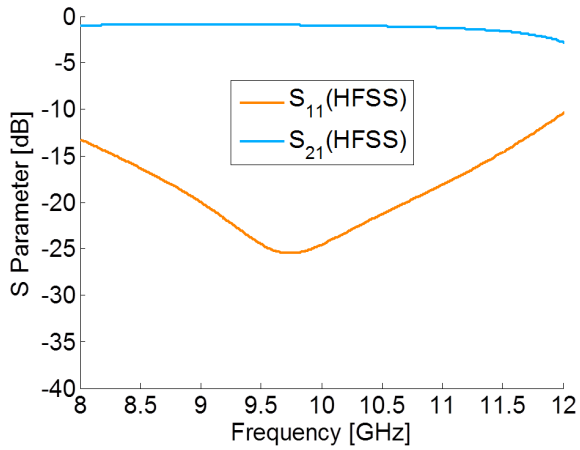

Figure 4.6: Unit-cell return loss and insertion loss

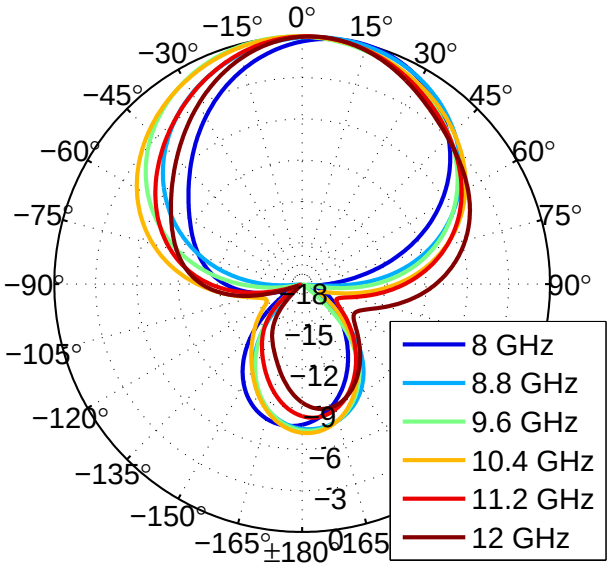

Figure 4.7: Unit-cell E-plane radiation pattern

4.3 Unit-Cell Matching For Broadside Radiation

The HMSIW phase constant β_0 at 9.6 GHz was extracted from Figure 4.3 (491.4 rad/m) and used to calculate the unit-cell length required for broadside radiation at 9.6 GHz (i.e. $\beta_{-1}(9.6GHz) = 491.4 - 2\pi/s = 0$ so $s = 12.8mm$). In order to observe the anticipated open-stopband, three unit-cells were cascaded without matching sections and simulated to acquire the transfer matrix as a function of frequency between 8–12 GHz. Multiple unit-cells were cascaded to account for the mutual coupling of adjacent radiating elements. The transfer matrix was then processed as shown in [34] (and outlined in Appendix A) to calculate the Bloch impedance of the structure which was compared to the HMSIW impedance (extracted from HFSS waveport solutions) as shown in Figure 4.9. The Bloch impedance is the theoretical input impedance of the periodic structure assuming it extends infinitely [24] and thus a poor Bloch impedance match to the HMSIW feed-line impedance corresponds to a poor input impedance match. This claim is verified in Figure 4.9 where the S-parameters of the 15 element structure shown in Figure 4.8 are presented alongside the Bloch impedance. As expected, the poor match of the Bloch impedance to the waveguide impedance at 9.6 GHz corresponds to a degradation in the return loss of the antenna and reveals the open-stopband behavior of the structure near 9.6 GHz.

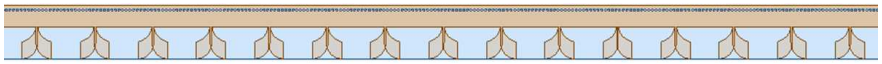

Figure 4.8: Non-inverting element structure without open-stopband compensation

In order to achieve broadside scanning performance, the open-stopband must be mitigated. The efficacy of the unit-cell matching technique for open-stopband mitigation can be observed in the Bloch impedance of the periodic structure [15]. For a periodic structure terminated with a real valued impedance, maximum power transfer occurs when the source, load and Bloch impedance are equal. Minimizing the unit-cell S_{11} with the addition of a matching section was considered equivalent to matching the Bloch impedance to the

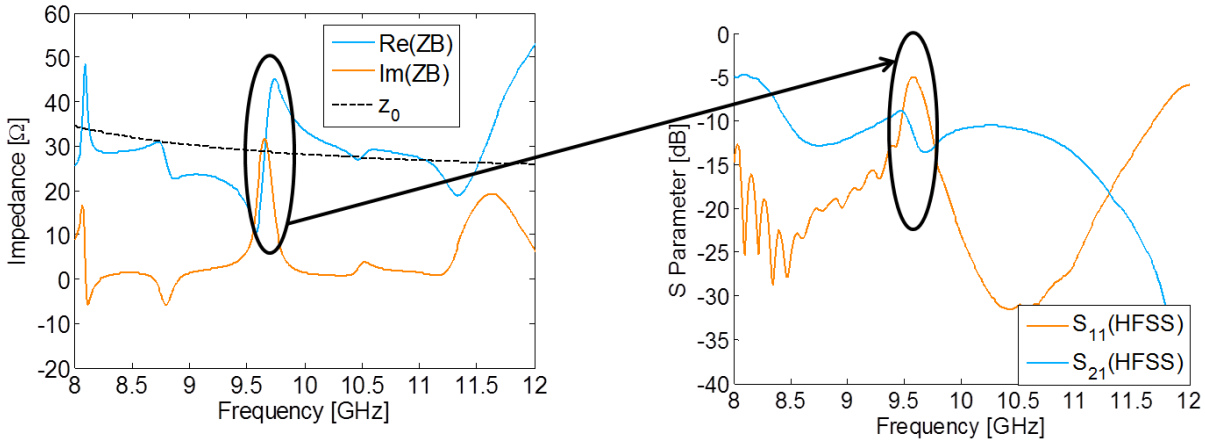

Figure 4.9: Bloch impedance and S-parameters of non-inverting element antenna exhibiting an open-stopband at broadside (9.6 GHz)

real valued HMSIW impedance (which was the source and load impedance of the periodic structure) as was explained in Chapter 2. Another way of interpreting this technique is that the reflections have to be reduced to an acceptably low level so that even when they add constructively in the reverse direction they do not severely degrade the input impedance match. A matching section was realized as a length of HMSIW parameterized in terms of its width, length, and distance to the unit-cell radiating element (Figure 4.10 w_{match}, l_{match}, and d_{match}, respectively).

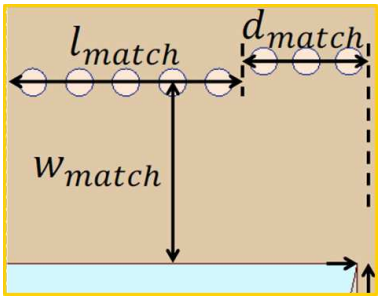

Figure 4.10: Unit-cell matching section parameters

The matching section parameters were optimized using the simulation environment shown in Figure 4.11 with the goal of minimizing the unit-cell S_{11} at the desired broadside frequency (9.6GHz).

The optimization variables and their domains are shown in Table 4.4. The domain of

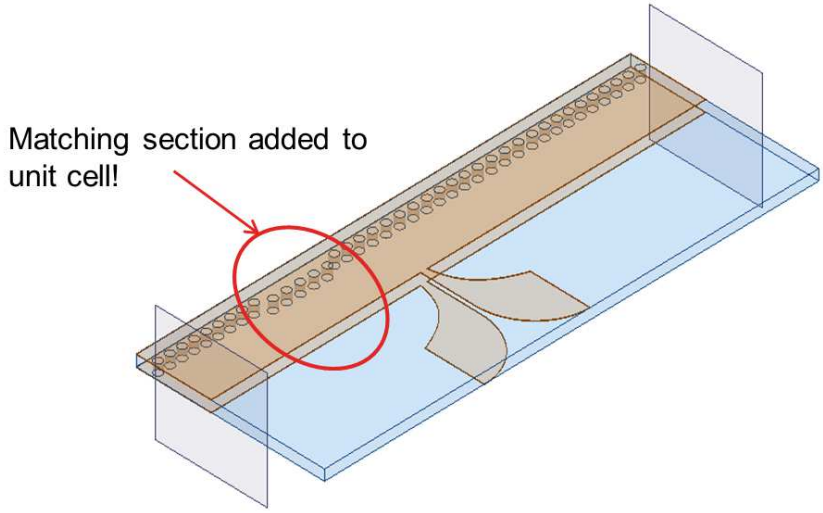

Figure 4.11: Non-inverting element antenna unit-cell matching section HFSS simulation and optimization environment

w_{match} was restricted to being within the allowed via spacing of maximum twice the via diameter while the length and location (l_{match} and d_{match}) of the matching section within the unit-cell was given a high degree of freedom. Optimization variable $s_{element}$, the unit-cell length, was included in order to allow the optimizer to acquire a 360° phase shift per unit-cell at 9.6 GHz as is required for broadside radiation.

Table 4.4: Unit-cell reduced width HMSIW matching section optimization variables

Variable	Minimum	Maximum
w_{match}	2.688 mm	4.032 mm
l_{match}	0 mm	10 mm
d_{match}	0 mm	10 mm
$s_{element}$	8 mm	16 mm

The unit-cell optimization used the sequential nonlinear programming technique [60]. The cost function settings are shown in Table 4.5. The S_{21} imaginary component was evaluated on a linear scale and therefore had to be weighted heavier than the return loss goal in order to enforce its impact on the cost function. Retrospectively, converting the

imaginary component of S_{21} and the associated goal to a logarithmic scale would have been equally or more effective.

Table 4.5: Unit-cell matching section sequential nonlinear programming optimization settings

Calculation	Range	Goal	Weight
Return Loss	9.6 GHz	≤ -30 dB	1
S_{21} Imaginary Component	9.6 GHz	$= 0$	100

The cost-function for the optimization was reduced to nearly zero indicating that the unit-cell would have a very low reflection coefficient at the broadside frequency (indicated by the S-parameter plot in Figure 4.12) and that the element periodicity $s_{element}$ for 9.6 GHz broadside radiation had been deduced (after ensuring a positive, real valued S_{21}). The resulting parameter values were $l_{match} = 4.31$ mm, $w_{match} = 3.36$ mm, $d_{match} = 2.34$ mm and $s_{element} = 13.38$ mm.

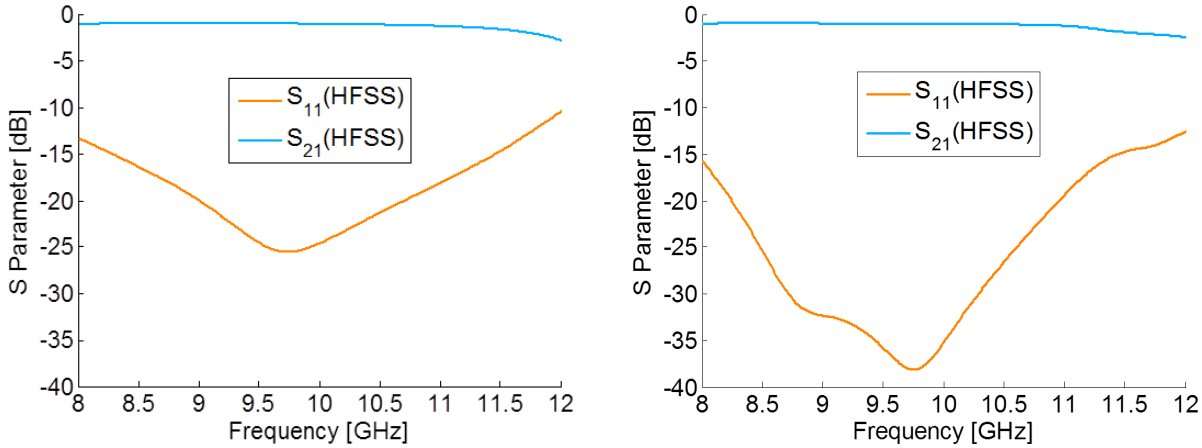

(a) No Matching

(b) With Matching

Figure 4.12: S-parameters of non-inverting element antenna unit-cell with and without the 9.6 GHz matching section

Now, in order to inspect the efficacy and accuracy of the assumptions and the technique, three unit-cells with matching sections were simulated and the Bloch impedance of the structure was calculated, again using the technique outlined in Appendix A. In addition a 15

element structure with matching sections was simulated to ensure the return loss degradation was mitigated. Figure 4.13 presents the results of these simulations as compared to the previous results without the unit-cell matching section. It was observed that the addition of the unit-cell matching section significantly improved the Bloch impedance matching to the waveguide impedance z_0 at the broadside frequency, corresponding to a greatly improved broadside return loss, thus verifying open-stopband mitigation.

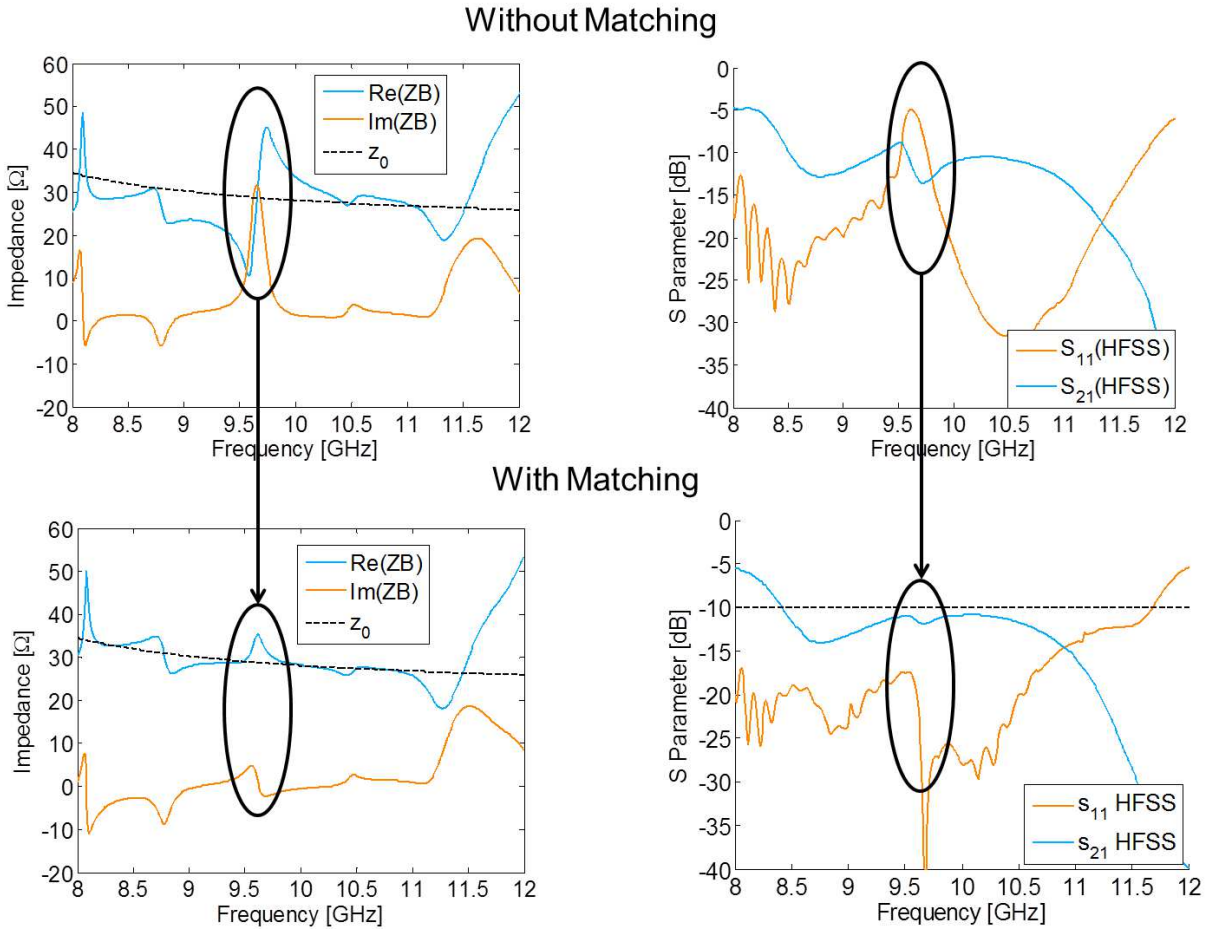

Figure 4.13: Non-inverting element antenna open-stopband mitigation verification through Bloch impedance and S-parameter simulation

4.4 Periodic Phase-Reversal

As was described in Chapters 2 and 3, the periodic phase-reversal design brings elements 180° closer together (with respect to the HMSIW feed-line guided wavelength) at the broadside frequency and successively inverts the polarity of adjacent radiators in order to maintain in-phase excitation of radiated fields (as was shown in Figure 3.4) [19].

Compared to the non-inverting element design, much of the periodic phase-reversal design remains unchanged. This includes HMSIW parameters, microstrip to HMSIW transition parameters (to be outlined in the next section), as well as ATSA element parameters w_{feed}, l_{feed} and b. ATSA element parameter r was given some flexibility in the periodic phase-reversal design to ensure adjacent ATSA elements would contact as it was observed that small gaps between elements degraded the simulated radiation pattern. Although the matching section parameter values were modified, the process by which they were found remained unchanged.

Firstly, in order to observe the expected open-stopband return loss degradation near the 9.6 GHz broadside frequency, a 20 element structure was simulated as shown in Figure 4.14. Again, the unperturbed HMSIW phase constant β_0 from Figure 4.3 was used to calculate the unit-cell length required for broadside radiation at 9.6 GHz (i.e. $\beta_{-1}(9.6\ GHz) = 491.4 - \pi/s = 0$ so $s = 6.4$ mm).

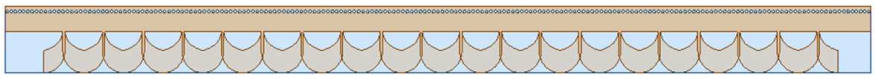

Figure 4.14: Twenty element periodic phase-reversal antenna open-stopband simulation

In addition, a six element structure was simulated and the results were processed to acquire the Bloch impedance using the technique outlined in Appendix A. The Bloch impedance and 20 element S-parameters are shown in Figure 4.15. Again a poor match between the Bloch impedance and the waveguide impedance corresponds to a degradation in the return loss of the 20 element structure.

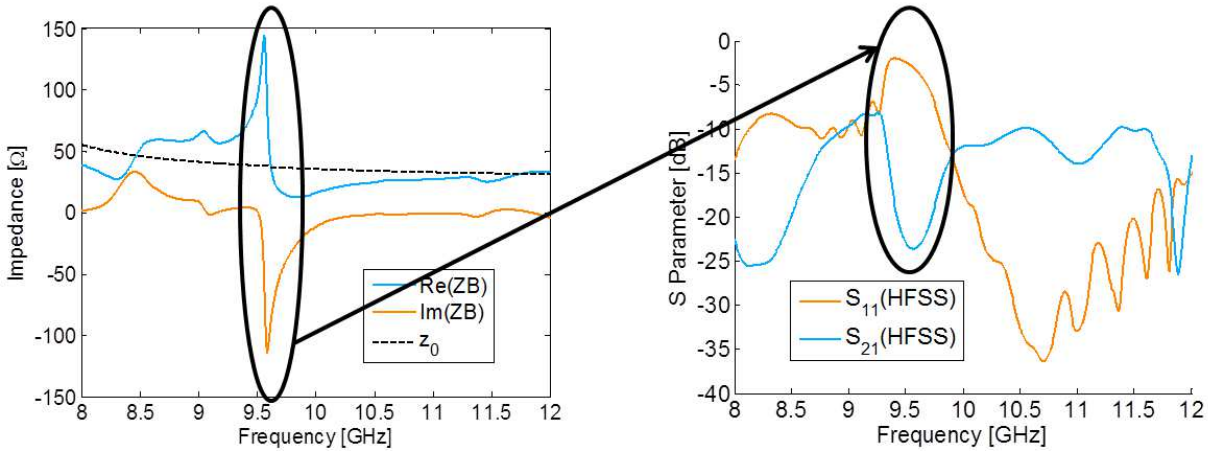

Figure 4.15: Periodic phase-reversal antenna open-stopband (9.6 GHz) Bloch impedance and return loss degradation

To address the open-stopband observed in the periodic phase-reversal LWA, the unit-cell matching technique was again employed. An optimization was executed that ensured element parameter r was valued such that adjacent ATSA elements would contact (i.e. $r = s_{element}/2 + w_{feed}/2$), while parameters w_{match}, l_{match}, d_{match} and $s_{element}$ were varied to acquire a minimum 30 dB return loss at the broadside frequency while maintaining a 180° phase shift between radiating elements (thus the inclusion of $s_{element}$ in the optimization).

Two cascaded unit-cells (as shown in Fig. 4.16) were used in the optimization to account for mutual coupling between adjacent radiators. Optimization with more unit-cells would likely have further improved the matching results for the 20 element structure at the broadside frequency, however it will be seen that the open-stopband was mitigated regardless.

The optimization variables for the periodic phase-reversal matching section remained the same as those used in the non-inverting element design, shown in Table 4.4, with a decreased domain for l_{match} and d_{match} due to the element spacing being reduced by approximately half. The optimization settings also remained the same (Table 4.5) to ensure weak unit-cell reflections at broadside and a total phase shift of 0° per two radiating elements (i.e. 180° between elements).

The resulting parameters values were $l_{match} = 4.12$ mm, $w_{match} = 3.24$ mm, $d_{match} = 2.14$

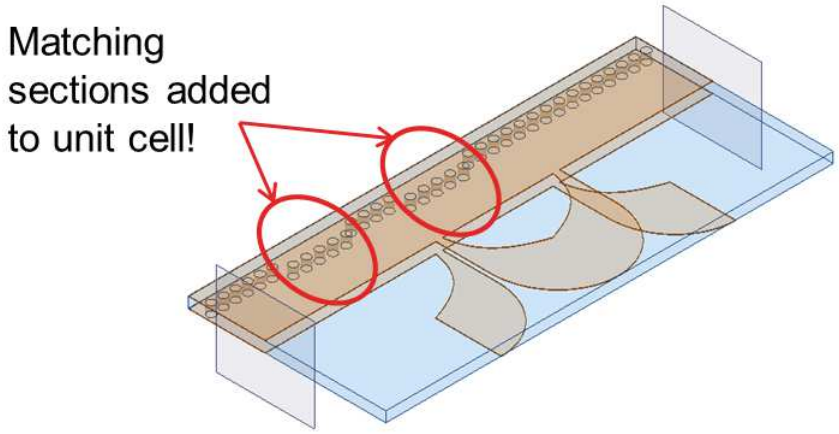

Figure 4.16: Periodic phase-reversal antenna unit-cell matching section HFSS simulation and optimization environment

mm and $s_{element} = 7.29$ mm. Figure 4.17 shows the S-parameters of the two element structure after matching section optimization compared to the single element S-parameters without unit-cell matching (from Section 4.2).

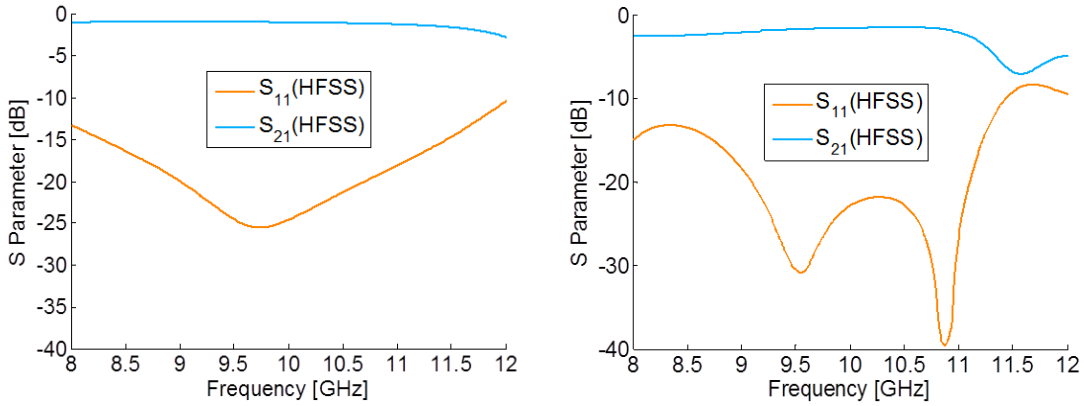

(a) Single element w/o Matching

(b) Two elements w matching

Figure 4.17: Periodic phase-reversal antenna two element S-parameters with matching compared to single element S-parameters without matching

In order to verify the technique was effective in eliminating the open-stopband, a six element periodic phase-reversal structure with unit-cell matching was simulated from which the Bloch impedance was calculated as a function of frequency using equations from Appendix A. A 20 element structure was also simulated in order to further verify the technique. The

results of these simulations are compared to the simulation results without matching sections in Figure 4.18. It is clear from Figure 4.18 that the addition of the unit-cell matching section greatly improved the Bloch impedance match to the waveguide impedance (extracted from HFSS waveport solutions) at the broadside frequency (9.6 GHz). The improved Bloch impedance match corresponds to an improved return loss for the 20 element structure as expected.

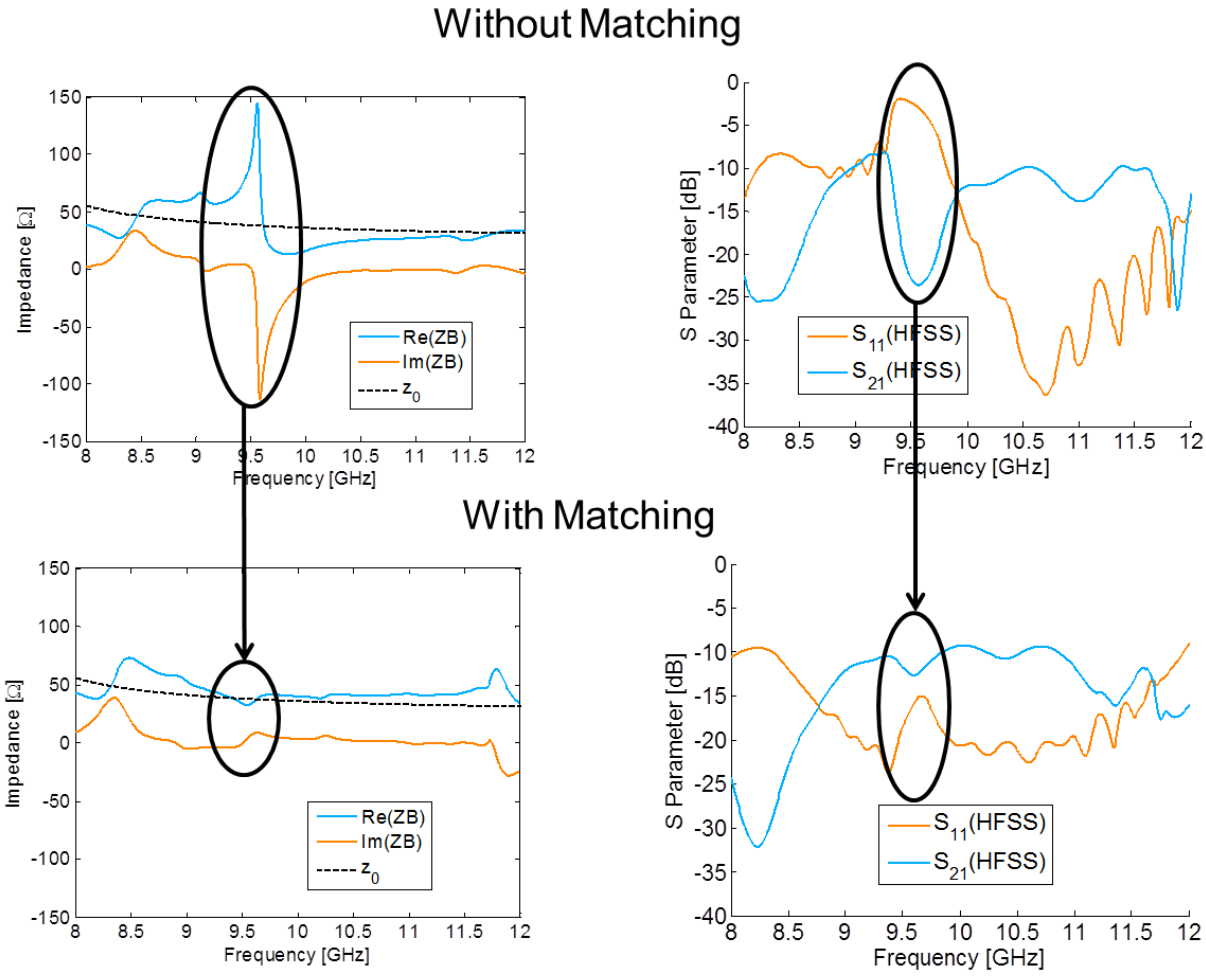

Figure 4.18: Periodic phase-reversal antenna Bloch impedance and S-Parameters with unit-cell matching

4.5 Tapered Microstrip Excitation

Microstrip transmission line was used for excitation and matched load termination of both the non-inverting element and periodic phase-reversal antennas. The geometry of the excitation mechanism is shown in Figure 4.19 and includes a microstrip to HMSIW taper transition as well as a tapered ground plane to enable the addition of ATSA elements to the HMSIW open sidewall.

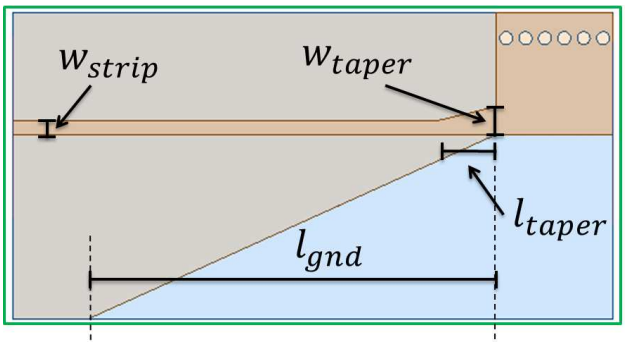

Figure 4.19: Tapered microstrip with tapered ground plane to HMSIW transition (w_{strip} = 0.55 mm, w_{taper} = 1.11 mm, l_{taper} = 2.28 mm, l_{gnd} = 16 mm)

Keysight (fomerly Agilent) ADS LineCalc tool was used to acquire the width for 50 ohm microstrip on the desired Rogers RO3210 substrate. The width was then optimized (for 50 ohms at 10 GHz) in HFSS resulting in w_{strip} = 0.55 mm, reduced from the ADS suggested width of w_{strip} = 0.58 mm. As discussed at the beginning of this chapter, it was initially believed that the substrate had a relative permittivity of 10.2 which caused some error in the microstrip width optimization. Regardless, the microstrip was re-simulated with the new anisotropic substrate model from which a 48.4 ohm impedance was computed which is still very close to the desired 50 ohms. Also TRL calibration [61, 62] used in measurements (and outlined in Appendix B) helped to remove connector mismatch from results.

It was first shown in [4] that microstrip could efficiently transition to SIW over a broad bandwidth through the use of a linearly tapered quarter wavelength microstrip section. This technique was used in the proposed designs. Empirically derived equations provided in [63]

allow computation of the ideal microstrip width that could be used to feed a given SIW, thus defining the ideal taper width. The taper length can then be calculated using equations from [64] to find a quarter wavelength section assuming a linear taper from the microstrip width to the taper width. The technique from [63] used for the taper width calculation does not however describe a method for dealing with HMSIW. Instead another optimization (described by Table 4.6 and Table 4.7) was completed where the HMSIW structure was fed by a non-tapered line (as shown in Figure 4.20) with a width that was varied to increase the return loss to greater than 20 dB within 8–12 GHz.

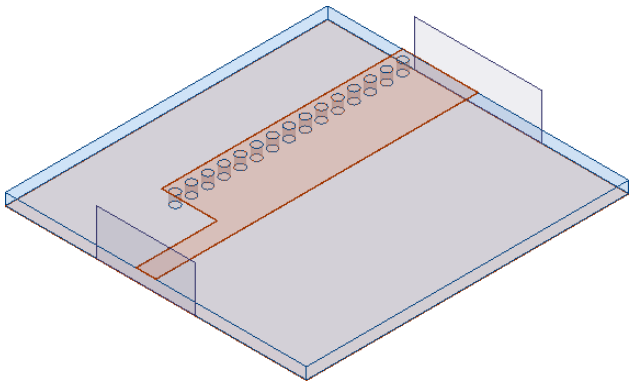

Figure 4.20: Microstrip to HMSIW taper width (w_{taper}) optimization environment

Table 4.6: Microstrip to HMSIW taper width optimization variables

Variable	Minimum	Maximum
w_{taper}	0.5 mm	3 mm

Table 4.7: Microstrip to HMSIW taper width sequential nonlinear programming optimization settings

Calculation	Range	Goal	Weight
Return Loss	8–12 GHz (0.2 GHz step)	$\leq -20dB$	1

The result of the optimization was an optimal taper width of $w_{taper} = 1.11$ mm. Analytical equations from [64] were then used to compute the length of taper required to ensure a quarter wavelength assuming a linear taper from microstrip width $w_{strip} = 0.55$ mm to the taper width $w_{taper} = 1.11$ mm at 10 GHz (near the center of the expected operating frequency band) as is required to maximize the usable return loss bandwidth [63]. The resulting length $l_{taper} = 2.28$ mm was found to be acceptable without optimization, maintaining a return loss greater than 20 dB between 8–12 GHz for the single ended transition.

The HMSIW ground plane typically extends past the open sidewall of the structure in most published works (as shown in Figure 4.20) however it does not for the proposed antenna designs due to the introduction of the ATSA elements. Truncation of the ground plane did not have a significant impact on the return loss of the transition, however it was observed that tapering the ground plane could reduce the insertion loss for a dual sided transition, likely due to unwanted radiation from the abrupt ground plane discontinuity without tapering. A parametric sweep revealed that increasing the taper length greater than 16 mm offered diminishing benefits, at least partially due to loss in the extended length of the structure, and thus the taper length was set to $l_{gnd} = 16$ mm.

The final design of the single ended transition (shown in Figure 4.19) with the corrected anisotropic substrate model was simulated and its S-parameters are shown in Figure 4.21.

The simulated single ended transition return loss was greater than 20 dB between 8–12 GHz and the insertion loss was less than 0.5 dB. A back-to-back transition was also simulated as shown in Figure 4.22.

The S-parameters of the back-to-back transition are shown in Figure 4.23 where the insertion loss was observed to be less than 1 dB between 8–12 GHz and a return loss greater than 20 dB was maintained.

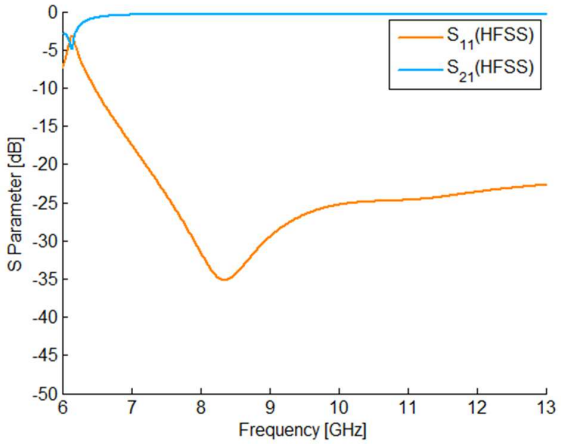

Figure 4.21: Single-ended tapered microstrip with tapered ground plane to HMSIW transition S-parameters

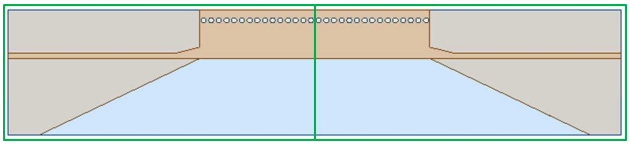

Figure 4.22: Back-to-back transition simulation geometry

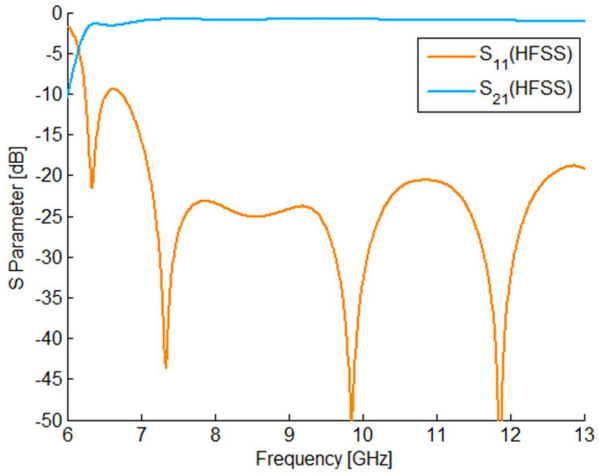

Figure 4.23: Back-to-back transition S-parameters

4.6 Leaky Wave Analysis and Theoretical Radiation Patterns

With both antenna designs complete the radiating characteristics of multiple cascaded unit-cells were predicted using periodic LWA theory. First, as was emphasized in Chapter 2, the leaky-wavenumbers of the structures had to be computed ($k_{LW} = \beta_{-1} - j\alpha$ where β_{-1} is the phase constant of the $n = -1$ space harmonic and α is the mode attenuation coefficient). To do so the simulated transmission matrix of three cascaded unit-cells of the non-inverting element design, used also to calculate the Bloch impedance of the periodic structure, were processed as shown in Appendix A. The technique is relatively simple, relying on the computation of the eigenvalues of the transmission matrix at each frequency. The calculated leaky-wavenumber (normalized to free space wavenumber k_0) of the non-inverting element antenna is shown in Figure 4.24 from which a broadside frequency of 9.61 GHz was predicted ($\beta_{-1}/k_0 = 0$).

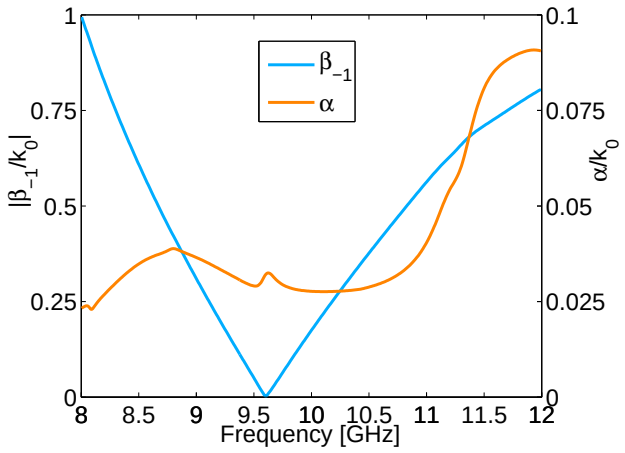

Figure 4.24: Non-inverting element LWA k_{LW}

The calculated leaky-wavenumber of the periodic phase-reversal antenna (normalized to free space wavenumber k_0) using simulated data for six cascaded elements is shown in Figure 4.25, where a broadside freqeuncy of 9.57 GHz was predicted.

The leaky-wavenumbers of the antennas can be used to investigate the grating lobe free scan range of the antennas as well as to compute theoretical radiation patterns. Firstly,

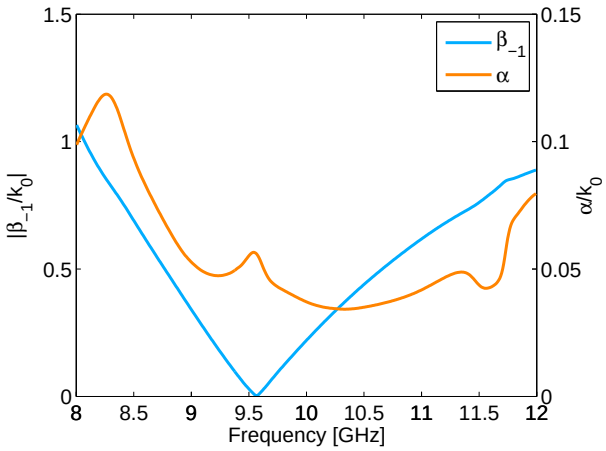

Figure 4.25: Periodic phase-reversal LWA k_{LW}

periodic LWA phase constants for the first three radiating space harmonics ($n = 0$, $n = -1$, and $n = -2$) are shown for the non-inverting element antenna in Figure 4.26 relative to the magnitude of the free space wavenumber k_0 which defines the "fast-wave region" on the graph. As was described in Chapter 2, when the phase constant of a space harmonic (or Floquet mode) enters the fast wave region it becomes fast and radiating. Thus the computed phase constant for the $n = -1$ mode predicts beam scanning from reverse to forward endfire between approximately 8–12.8 GHz however the $n = -2$ mode starts to radiate at reverse endfire at approximately 12.1 GHz, limiting the grating lobe free scan range of the antenna.

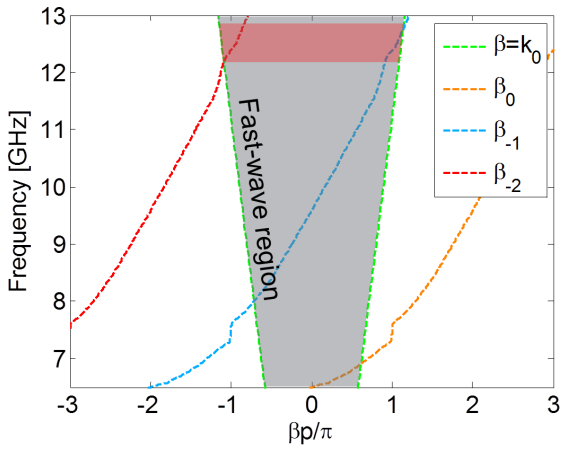

Figure 4.26: Non-inverting element antenna simulated dispersion curves for first three radiating space harmonics

Using the array factor computation introduced in Chapter 2 [35], [9] in combination with the element radiation pattern from simulations, the antenna radiation pattern can be predicted. Considering the coordinate system shown in Figure 3.1, let us define a spherical coordinate system with the $+y$ direction as the zenith, ϕ as the polar angle and θ as the azimuthal angle, both measured from $+x$. Then, the $M = 15$ unit-cell non-inverting element antenna array factor in the substrate plane of the antenna is computed as shown in Chapter 2 (i.e. equations 2.35 and 2.36), using:

$$V_m = e^{-jk_{LW}((m-1)s_{element}-l/2)}, m = 1, 2, ..., 15 \tag{4.4}$$

from which,

$$AF(\phi) = \sum_{m=1}^{15} V_m e^{jk_0(m-1)s_{element}\sin\phi} \tag{4.5}$$

can be solved. Note that the $\cos\theta$ term from equation 2.36 was changed to $\sin\phi$ due to the coordinate system definition above. The computation is essentially a discrete space Fourier transform of an aperture defined by point source isotropic radiators separated by $s_{element}$ with the magnitude and phase of the m^{th} radiator being defined by V_m. The normalized result of the array factor computation for the non-inverting element design is shown in Figure 4.27 for a sample of frequencies.

In Figure 4.27 the array factor beam scans from reverse endfire at 8 GHz to near forward endfire at 12 GHz, however at 12 GHz a reverse endfire grating lobe has begun to appear with a magnitude around -2 dB, as expected from the dispersion diagram of Figure 4.26. In order to predict the radiation pattern of the antenna the array factor must be multiplied by the element pattern for each frequency (using element patterns from Figure 4.7) [1]. Note that the array factor is symmetric about $\phi = \pm 90°$ and the full array factor from $\phi = \pm 180°$ is used for pattern computation.

The resulting theoretical radiation patterns for the non-inverting element antenna are

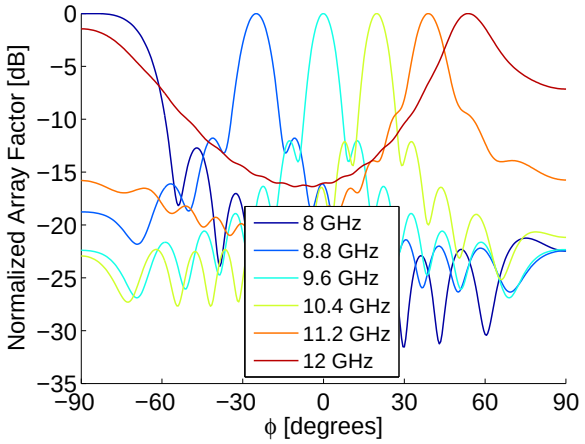

Figure 4.27: 15 unit-cell non-inverting element antenna normalized array factor

shown in Figure 4.28, where back radiation (in the $|\phi| > 90°$ region) is reduced by the element radiation pattern. Patterns approaching reverse and forward endfire ($|\phi| = \pm 90°$) have broader beamwidths, in part due to the element pattern reducing radiation in these directions. From the theoretical pattern, the reverse endfire grating lobe corresponding to radiation from the $n = -2$ space harmonic was expected to be greater than -10 dB at 12 GHz, thus limiting the grating lobe free scan range of the antenna.

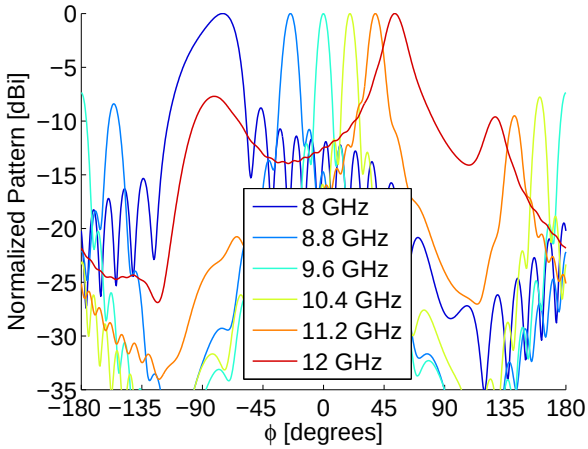

Figure 4.28: 15 element non-inverting element antenna theoretical patterns

Now, as described before, the periodic phase-reversal of elements in a LWA can increase the antenna's grating lobe free scan range by reducing the radiating element spacing. This claim is verified by the periodic phase-reversal dispersion curve shown in Figure 4.29 where

it is seen the $n = -1$ space harmonic is allowed to scan through the full fast wave region without the appearance of grating lobes from the -2 space harmonic.

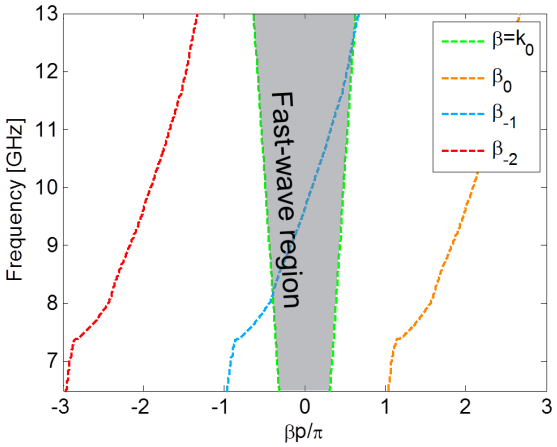

Figure 4.29: Periodic phase-reversal antenna simulated dispersion curves for the first three radiating space harmonics

The leaky-wavenumber of the periodic phase-reversal antenna was used to compute the antenna array factors shown in Figure 4.30. From the array factors it is evident that the $n = -1$ space harmonic is able to scan up to 12 GHz with no sign of a reverse endfire grating lobe.

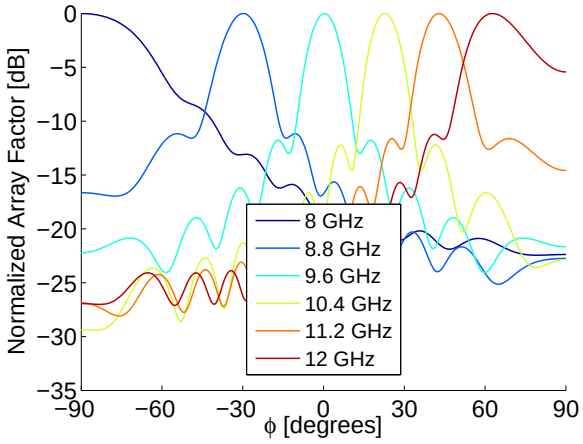

Figure 4.30: 20 element periodic phase-reversal antenna array factors

Grating lobes therefore do not limit the antenna scan range. This was verified in the theoretical radiation patterns for the periodic phase-reversal LWA shown in Figure 4.31

which again were obtained by multiplying the antenna array factor by the corresponding ATSA element pattern from Figure 4.7 for a given frequency. Scan angles approaching endfire directions again suffered pattern and beamwidth degradation due to the element pattern, which predicted poor radiation in these directions. Additionally, high values of α at lower frequencies (shown in Figure 4.25) are indicative of radiation being concentrated at the input of the antenna, which further degrades the pattern and beamwidth at reverse endfire (also shown in the array factor in Figure 4.30).

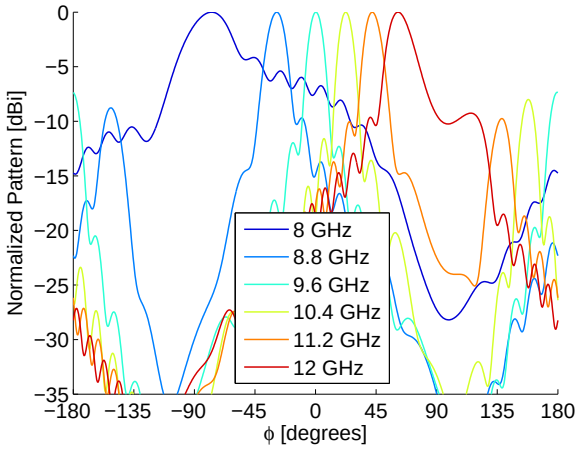

Figure 4.31: 20 element periodic phase-reversal antenna theoretical patterns

4.7 Chapter Summary

In this chapter the design techniques used to arrive at the proposed antenna architectures were outlined. Leaky wavenumbers for the resulting structures were computed and used to predict theoretical radiation patterns for both antennas. A resulting summary of the suggested generalized design process and considerations for SIW based periodic and periodic phase-reversal LWAs is given here:

- The first design choices that should be addressed are the choice of substrate permittivity and broadside to cutoff frequency ratio f_b/f_c. These choices can be made based on analysis provided in Appendix C where it is shown that maximizing f_b/f_c will minimize

the required substrate permittivity for grating lobe free scanning, however it should be chosen such that the operating frequency range of the antenna is within the single mode operating bandwidth of the waveguide.

- Using the phase constant of the resulting waveguide, the operating frequency range can be deduced for the desired scan range of the antenna by calculating the $n = -1$ mode phase constant and using the scan angle approximation $\sin(\phi_{max}) \approx \beta_{-1}/k_0$ (where $\phi = 0$ is broadside).

- The radiating element should then be designed to weakly load the guided mode (indicated by a high unit cell return loss) over an impedance bandwidth encompassing the desired operating frequency range. Additionally, the radiating element pattern should encompass the desired scan range, and the radiated power per element should be designed to meet directivity requirements for the given application (weaker radiation over a longer antenna increases directivity).

- For broadside radiation, a unit-cell matching network can be designed to minimize the unit-cell S_{11} at the desired broadside frequency (i.e. matching the Bloch impedance of the periodic structure at broadside to the characteristic impedance of the HMSIW).

- The addition of radiating elements and matching sections to the structure inevitably effects the phase shift per unit-cell compared to the unloaded waveguide transmission line model. The unit-cell length must, therefore, be adjusted to ensure a 2π phase shift between elements at the desired broadside frequency for the non-inverting element antenna or a π phase shift for the periodic phase-reversal design.

- Depending on the degree to which radiating element mutual coupling impacts design performance, some number of cascaded unit-cells (say M) should be simulated. For accurate representation of a longer periodic structure (say N unit-cells), simulations should be conducted with incrementing numbers of unit-cells until results of periodic

analysis (in Appendix A) converge. The resulting M unit-cell structure S-parameters can then be inspected to ensure the desired broadside frequency is maintained (i.e. $\angle S21 = M2\pi$ for the non-inverting element antenna and $\angle S21 = M\pi$ for the periodic phase-reversal antenna, corresponding to $\beta_{-1}(f_b) = 0$). Additionally, open-stopband mitigation can be verified through Bloch impedance analysis (i.e. $Z_B^+ \approx Z_0$). The change in the phase constant of the structure relative to the unloaded HMSIW phase constant used for initial design may result in grating lobe free scanning conditions being broken. If the broadside frequency shifts, the open-stopband mitigation is inadequate, or the grating lobe free scanning condition is broken, design iteration may be required.

- Once acceptable results for the M unit-cell structure are attained, either by iteration or conservative design choices, the leaky-wavenumber can be used to compute the array factor of the N unit-cell full antenna. In combination with simulated unit-cell patterns at each frequency the antenna radiation patterns can be predicted.

- Finally, full antenna prototyping and simulation is required to verify that the antenna performance is within specifications.

In Chapter 5 the theoretical antenna performance derived in this chapter for both the non-inverting element architecture and the periodic phase-reversal architecture are compared to full antenna simulations and prototype measurements.

Chapter 5

Experimental validation

In the previous chapter the design and simulation techniques used to arrive at the proposed antenna architectures were shown in detail. In this chapter, prototype fabrication is described and the finalized design simulations and measured results are presented.

5.1 Antenna Prototyping

Both the non-inverting element antenna and the periodic phase-reversal antenna were fabricated by Candor Industries on the same Rogers 3210 panel to reduce the cost of prototyping. A 15 unit-cell non-inverting element prototype was fabricated and is shown in Figure 5.1. The antenna is approximately 26.6 cm long and 1.2 cm wide. Five identical prototypes were fabricated in order to investigate the repeatability of the fabrication process. Three identical 20 element periodic phase-reversal prototypes were fabricated, one of which is shown in Fig 5.2. The antenna is more compact than the non-inverting element antenna (approximately 22.7 cm long and 1.2 cm wide).

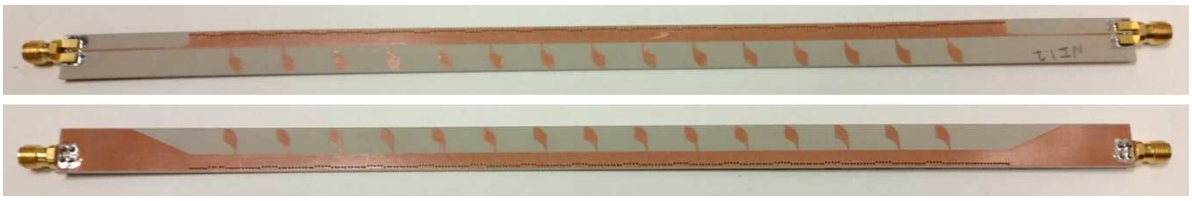

Figure 5.1: One of five 15 element non-inverting element antenna prototypes

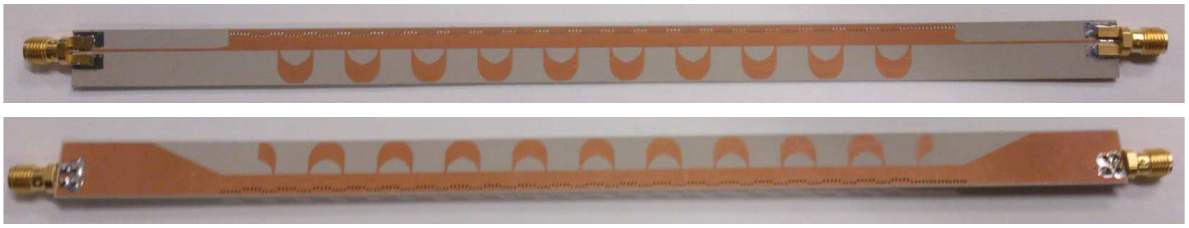

Figure 5.2: One of three 20 element periodic phase-reversal antenna prototypes

5.2 Antenna Leaky-Wavenumber Measurements and Simulations

The leaky-wavenumber ($k_{LW} = \beta_{-1} - j\alpha$, where β_{-1} is the phase constant of the $n = -1$ space harmonic and α is the mode attenuation coefficient) of the 15 unit-cell non-inverting element periodic structure was extracted from simulations and compared to the measured leaky-wavenumbers of the 5 prototype antennas. In order to yield the best comparison, measurements and simulations both consisted of 15 cascaded unit-cells. Results for the periodic structure were processed as shown in [34] and outlined in Appendix A in order to obtain the leaky-wavenumber at each solution frequency. Measurements required the removal of connector effects using TRL calibration (outlined in Appendix B [62], [61]) and microstrip to HMSIW transitions were removed using HFSS simulations and basic de-embedding techniques (also outlined in Appendix B). The TRL calibration and microstrip to HMSIW transition deembedding was required to move the measurement planes to lie on periodic boundaries of the periodic structure, as is necessary in order to process the resulting data using periodic analysis. The simulated and measured normalized leaky-wavenumbers are shown in Fig. 5.3. One prototype was used subsequently for impedance and radiation pattern measurements (labelled β_{-1} Measured in Fig. 5.3).

The manufacturing process drill placement accuracy of ± 3 mils may be partially responsible for the slight deviation between measurements and simulations considering minimum via spacing features of 10 mils exist in the design. There were also measurement repeatability issues including cable movement as well as solder and connector differences which affect TRL calibration. The prototypes were fabricated on the same panel and so deviation in the

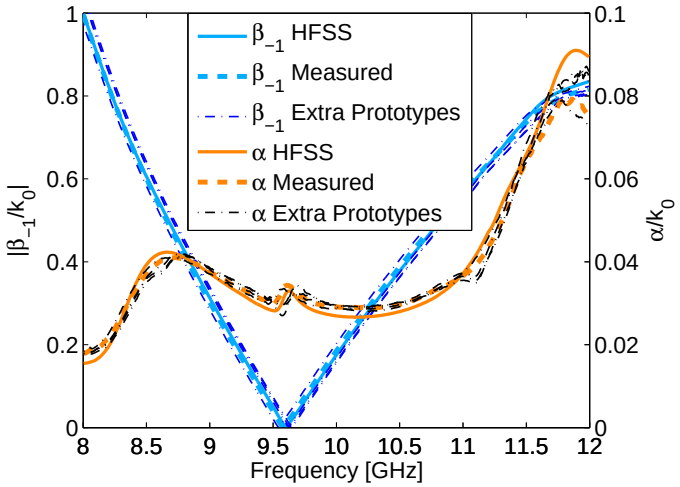

Figure 5.3: Normalized leaky-wavenumbers for simulated and measured 15 element non-inverting element antenna

substrate permittivity was probably an insignificant source of error, however if the unknown $x-y$ anisotropy is significant and the antennas were oriented differently on the panel, some variance in performance could then be expected. The leaky-wavenumbers indicate broadside radiation (when $\beta_{-1}=0$) near 9.6 GHz as anticipated by proper element spacing.

Measured leaky-wavenumbers for the three periodic phase-reversal antenna prototypes are shown in Figure 5.4 and are compared to the simulated leaky-wavenumber (extracted from a 20 element simulation). One prototype was used in subsequent measurements (labeled β_{-1} Measured in Fig. 5.4). Again TRL calibration and simulated microstrip to HMSIW data was used to shift the measurement planes to periodic boundaries withing the structure. Periodic analysis was then applied to the resulting 20 unit-cell measurements to compute the wavenumber at each frequency. Similarly, the simulated wavenumber was calculated using 20 unit-cell simulated data in order to yield the best comparison to measurements. As with the non-inverting element antenna, the leaky-wavenumbers of the periodic phase-reversal antenna indicate broadside radiation (when $\beta_{-1}=0$) near 9.6 GHz again as anticipated by proper element spacing for in-phase radiated field excitation.

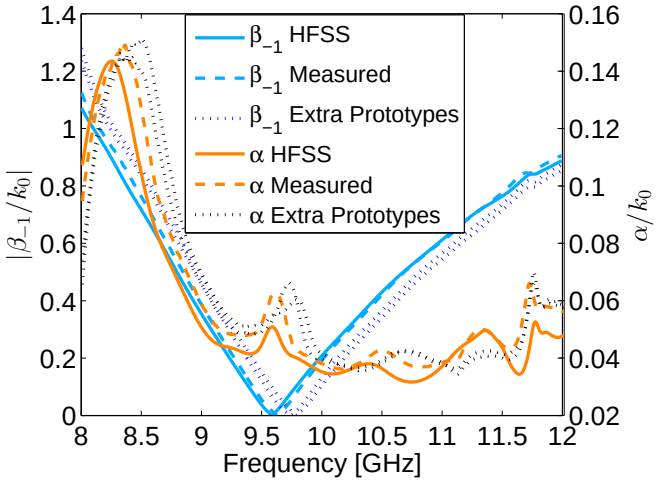

Figure 5.4: Normalized leaky-wavenumbers for the simulated and measured 20 element periodic phase-reversal antenna

5.3 Full Antenna Simulated and Measured S-parameters

Usually when a leaky wave antenna is in use, port 2 is terminated with a matched load in order to ensure traveling wave behavior on the structure. For this reason S_{22} and S_{12} are omitted from the results presented in this section. Full two port measurements were however necessary in order to process the data using periodic analysis to obtain the leaky-wavenumbers presented in the previous section. Two port measurements also enable the observation of the power terminated in the matched load of the antenna and therefore S_{21} is presented in addition to the typical 1-port antenna impedance bandwidth measurement S_{11}.

The simulated and measured non-inverting element antenna S-parameters are presented in Fig. 5.5. In order to best represent the frequency range over which power was coupled to radiation rather than leaving the antenna ports, the impedance bandwidth should require both the return loss and insertion loss to be greater than 10 dB. By this definition the antenna impedance bandwidth extended from 8.4–11.6 GHz (32%). The S-parameter measurements shown used TRL calibration to remove connector effects however microstrip to HMSIW transitions were not de-embedded.

The simulated and measured periodic phase-reversal antenna S-parameters are shown in

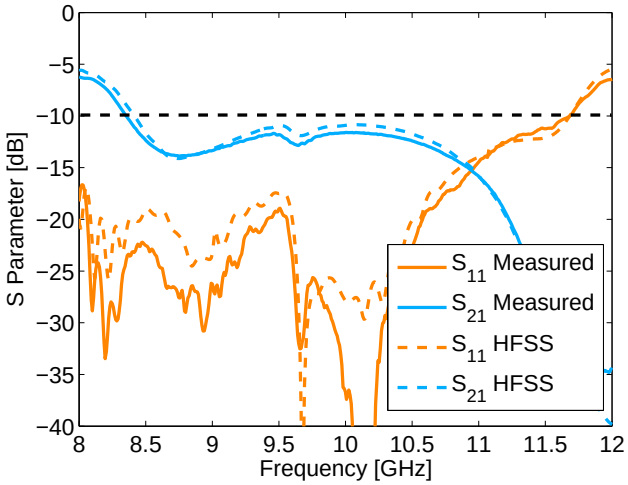

Figure 5.5: 15 element non-inverting element antenna measured and simulated S-parameters exhibiting a 32% impedance bandwidth and an effectively eliminated open-stopband at 9.6 GHz

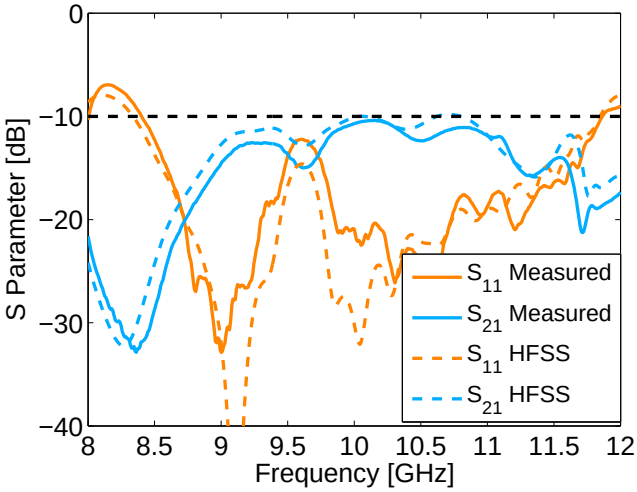

Figure 5.6: 20 element periodic phase-reversal antenna measured and simulated S-parameters exhibiting a 34% percent impedance bandwidth and a visible but mitigated open-stopband at 9.6 GHz

Fig 5.6. As with the non-inverting element antenna, the insertion loss and return loss should both be greater than 10 dB over the antenna bandwidth to ensure efficient excitation of the structure as well as less than 10% power dissipation in the matched load (port 2). The prototype insertion loss was greater than 10 dB between 8–12 GHz and thus the impedance bandwidth of the structure was observed to be limited only by the insertion loss and extended from 8.4–11.8 GHz (34%).

5.4 Radiation Patterns

Radiation pattern and gain measurements were conducted using antenna measurement facilities at the University of Calgary. The antenna range consisted of a Raymond-EMC anechoic chamber with an externally controllable turntable for DUT rotation (in this thesis being the prototype antennas) and an external Hewlett Packard® 8722D vector network analyzer (VNA) rated from 50 MHz to 40 GHz.

Antenna measurements using anechoic chamber ranges are often performed by connecting a sensor antenna and an AUT to a VNA in order to detect power transmitted between the two antennas over some known distance and a direct line of sight. For complete characterization, the AUT can be rotated in three dimensions relative to the line of sight of the sensor to characterize how well the AUT transmits/receives power at each polar/azimuthal angle. In order to obtain an accurate radiation pattern measurement of the AUT it must be illuminated by a plane wave (or conversely, illuminate a sensor with a plane wave, as antennas are reciprocal devices) without interference from multipath or signals from external sources. For the latter two of these reasons (interference and multipath) the anechoic chamber is generally lined with absorbing materials to suppress reflections and is electromagnetically sealed. The former requirement (plane wave illumination) is an idealistic one and can generally be approximated by a sufficient distance between the sensor and the AUT,

such that the following far field condition is met [1]:

$$R > \frac{2D^2}{\lambda_0}, \tag{5.1}$$

where D is the largest dimension of the AUT (or the sensor, whichever is larger). Distance R is called the Fraunhofer distance and can be derived as the distance at which a the curvature of a spherical wave-front is such that a tangential line of length D at this distance will be illuminated with a total phase shift of 22.5° over its length [1]. For an ideal plane wave source, in-phase illumination would occur at any distance from the source. The Fraunhofer distance is adequate for mid to high gain antennas so long as a high accuracy in low side-lobe levels is not required [1]. A schematic for the measurement setup used in characterization of the proposed antennas is shown Figure 5.7.

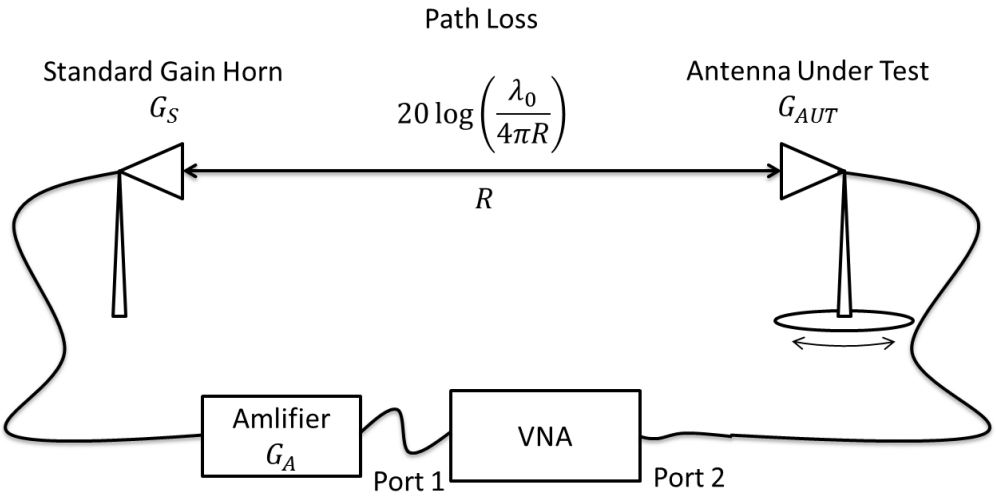

Figure 5.7: Radiation pattern and gain measurement setup

As shown in Figure 5.7, the AUT was mounted inside the anechoic chamber on the turntable to be rotated in a single plane, across from a standard gain ETS Lindgren pyramidal horn antenna [65] (3160 Series, Horn 3160-07, rated between 8.2-12.4GHz) that was used as a sensor. In order to meet the far field requirement for the non-inverting element antenna of total length 28.2 cm, R would have to be greater than 6.4 meters for 12 GHz measurements

which is longer than the length of the chamber. Now, at the sacrifice of some accuracy, if the length of the antenna aperture is taken as being $15 \cdot s_{element}$ (20.07 cm) (neglecting the microstrip feed and termination length), then the far field condition is $R \geq 3.22m$ and therefore making use of the maximum possible separation distance between the horn and the AUT (3.45 meters) was deemed acceptable. For the periodic phase-reversal antenna total length, the far field distance R would again be greater than the available distance in the chamber and so the antenna length was again reinterpreted, at the cost of some accuracy, to be an aperture length of $20 \cdot s_{element}$ (14.58 cm) resulting in $R \geq 1.7m$ and thus again a distance R of 3.45 meters was deemed acceptable.

Now, considering the coordinate systems shown in Figures 3.1 and 3.3, as was done in Chapter 4, again let us define a spherical coordinate system with the $+y$ direction (the antenna longitudinal axis) as the zenith, ϕ as the polar angle and θ as the azimuthal angle, both measured from $+x$. Both antennas are then linearly polarized in the ϕ direction and offer maximum radiation in the $x-y$ plane, thus defining the $x-y$ plane as the E-plane for all frequencies.

For E-plane co-polarized measurements the AUT had to be positioned with its aperture centered on the turntable and so that its $x-y$ plane was vertically and horizontally aligned with the center of the horn aperture. For co-polarized measurements the horn antenna was oriented with its broad wall extending vertically while the AUT $x-y$ was parallel to the ground. The AUT also had to be positioned with a known initial angle ϕ in the plane of rotation in order to accurately interpret measurement data. Photographs of the horn and the AUT in the anechoic chamber are shown in Figure 5.8 and Figure 5.9 respectively.

Polystyrene foam had to be used to construct a holder for the AUTs due to the open nature of the structures that made them very susceptible to radiating performance degradation in the presence of any other readily available materials. Retrospectively it would have been useful to design the antennas from the beginning assuming immersion in more rigid PMMA

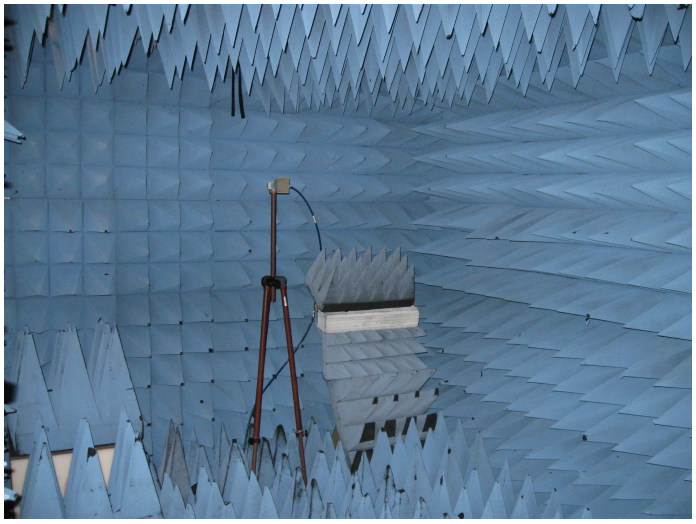

Figure 5.8: ETS Lindgren standard gain horn mounted for co-polarized E-plane measurement in the anechoic chamber

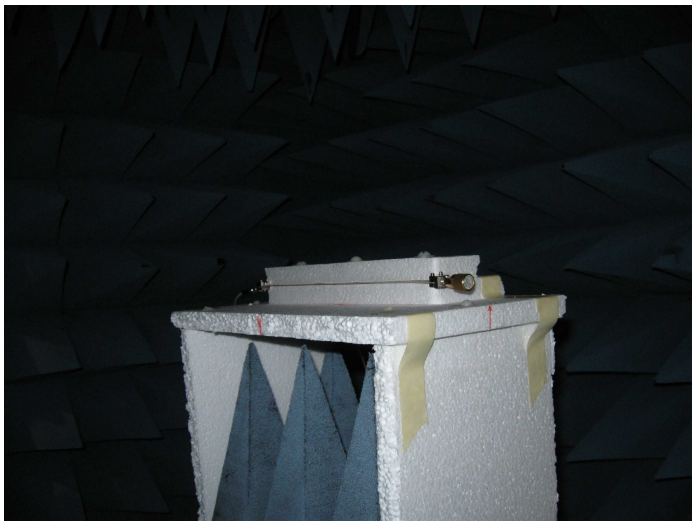

Figure 5.9: The non-inverting element antenna mounted for E-plane measurement in the anechoic chamber

based holder.

With the antennas alligned the AUT was then rotated by 0.5° increments and S_{21} measurements were recorded at each angle ϕ. Initially the radiation patterns were very noisy even with the lowest IF bandwidth setting on the VNA and thus the amplifier shown in the measurement schematic (Figure 5.7) was inserted to increase the dynamic range of the measurement system. The amplifier was characterized independently (shown in Figure 5.10) so that its associated gain could be removed from S_{21} measurements. Also shown in Figure 5.10 is the ETS Lindgren horn gain as a function of frequency [65].

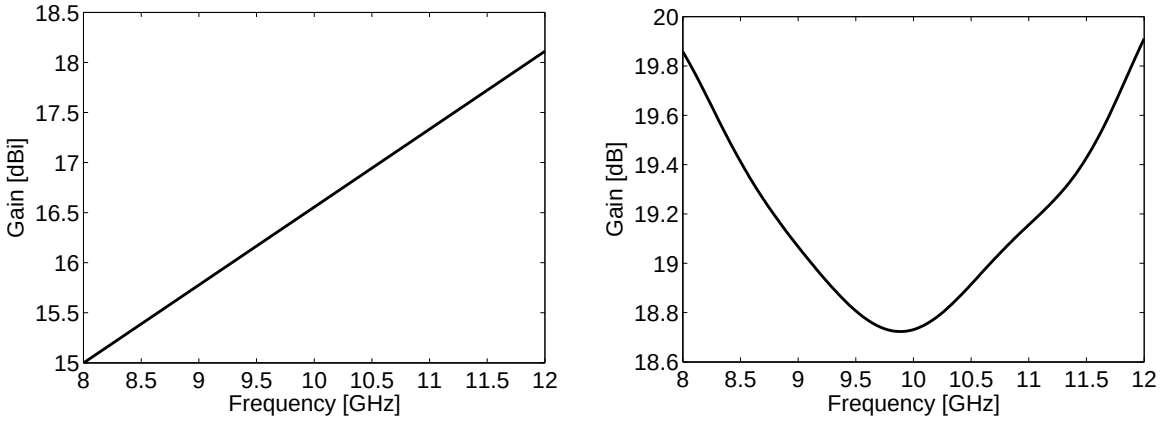

(a) Horn Gain (b) Amplifier Gain

Figure 5.10: Standard horn gain and measured amplifier gain

Loss due to the cables connecting the VNA to the amplifier/horn and AUT were calibrated before measurements. Also the antenna mismatch was recorded (S_{22}) in order to remove the reflected power from gain measurements. From the recorded $S_{21}^2 = \dfrac{P_r}{P_t}$ data, the AUT gain was then calculated using:

$$\frac{P_r}{P_t} = G_{AUT} G_S \left(\frac{\lambda_0}{4\pi R}\right)^2 \left(1 - S_{22}^2\right), \tag{5.2}$$

which is the Friis equation [1], modified to include the amplifier gain and the AUT mismatch. Note that all the information is now known except the AUT gain and thus can

be extracted from the S_{21} measurements at each angle. Measured, simulated and theoretical (from Chapter 4) E-plane (x-y plane) ϕ-polarized radiation patterns for the non-inverting element antenna for a sample of frequencies within the antenna impedance bandwidth are shown in Figures 5.11 and 5.12. As was anticipated, a reverse endfire grating lobe is visible at 12 GHz (Figure 5.12 in red near $\phi = -90°$).

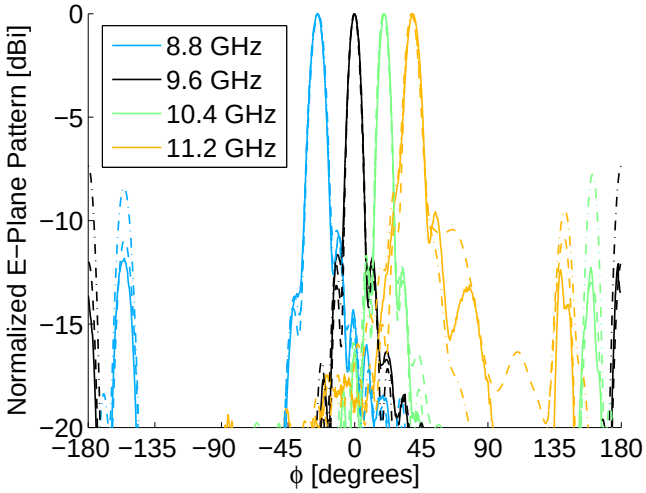

Figure 5.11: Non-inverting element antenna normalized E-plane radiation patterns [dBi]: Measured (———), Simulated (- - -), and Theoretical (- · - ·)

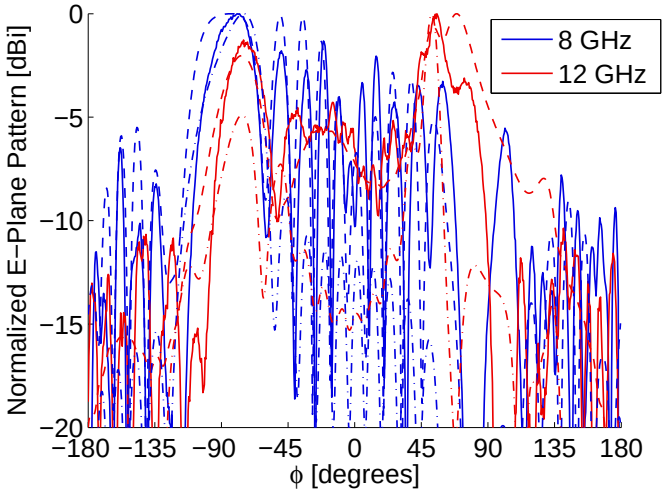

Figure 5.12: Non-inverting element antenna normalized E-plane radiation patterns [dBi]: Measured (———), Simulated (- - -), and Theoretical (- · - ·)

A simulated 3-D pattern for the non-inverting element antenna radiating at broadside is

shown in Figure 5.13 to exhibit the fan shape of the beam with maximum radiation in the plane of the substrate.

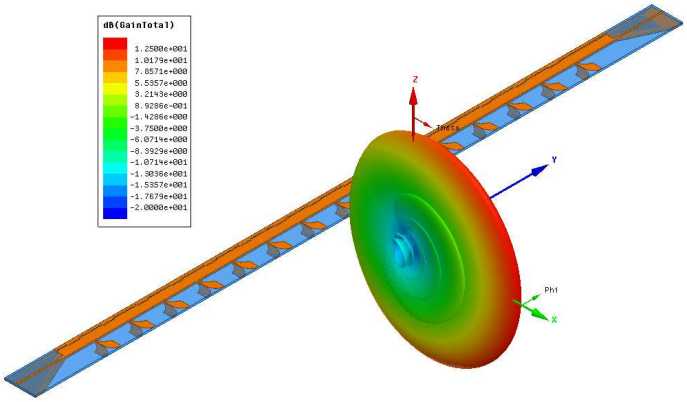

Figure 5.13: Non-inverting element antenna 3D simulated broadside radiation pattern

Back radiation (radiation in the region $|\phi| > 90°$) in measurements and simulations was lower than the theoretical back radiation, the most likely cause being that the extended length of the antenna and the radiating element mutual coupling were not accounted for in the unit-cell pattern used to calculate the theoretical radiation pattern (as shown in Chapter 4).

The H-plane of the main beam was defined by the cone shape produced by the array factor of the antenna, as shown in Figure 5.14. Due to the frequency dependence of the H-plane cones, H-plane pattern measurements were very difficult to acquire. Instead, simulated normalized H-plane patterns for the non-inverting element antenna are shown in Figure 5.15 for a sample of frequencies. At any particular frequency, $\theta = 0°$ corresponds to the main beam peak in the $|\phi| < 90°$ region while $|\theta| = 180°$ corresponds to the back radiation peak in the $|\phi| > 90°$ region.

According to simulations, the non-inverting element antenna linear polarization (E_ϕ/E_θ) of the main beam was greater than 15 dB for all frequencies. Cross-polarized radiation in this antenna is caused by the vertical offset of the ATSA element arms, causing θ directed radiation.

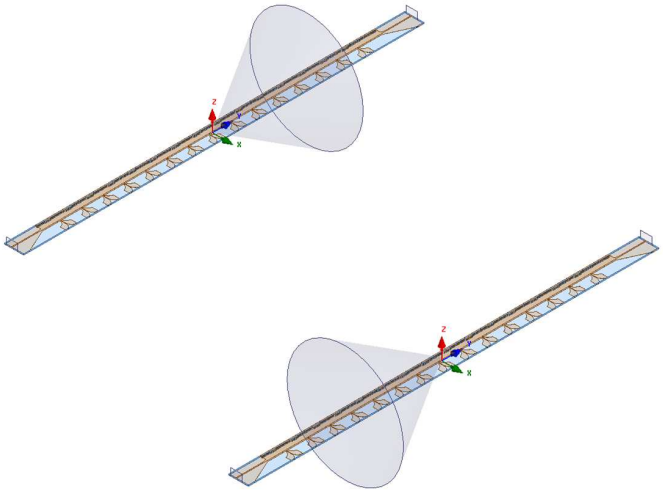

Figure 5.14: H-Plane radiation pattern cones

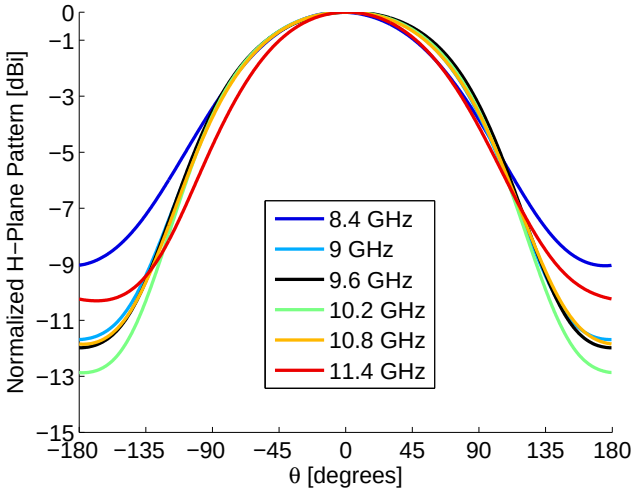

Figure 5.15: Non-inverting element antenna H-plane radiation patterns

The scanning behavior of the non-inverting element antenna is shown in Figure 5.16 where the main beam angle (ϕ_m) has been reported as a function of frequency. Simulated and measured results are presented as well as theoretical results relying on the well known relation $\phi_m = sin^{-1}(\frac{\beta_{-1}}{k_0})$. Both the simulated and measured β_{-1} values (from Figure 5.3) were used in this relation and are presented.

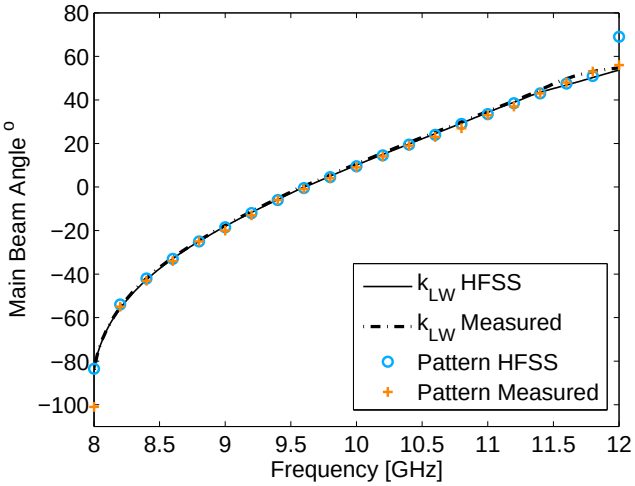

Figure 5.16: Non-inverting element antenna main beam angle ϕ_m as a function of frequency

Measured, simulated and theoretical (from Chapter 4) E-plane (x-y plane) radiation patterns for the periodic phase-reversal antenna for a sample of frequencies within the antenna impedance bandwidth are shown in Figure 5.17.

A simulated 3-D pattern for the periodic phase-reversal antenna radiating at broadside is shown in Figure 5.18 to exhibit the fan shape of the beam with maximum radiation in the plane of the substrate. As was anticipated, unlike the non-inverting element antenna, the periodic phase-reversal antenna did not exhibit a reverse-endfire grating lobe at 12 GHz.

As was the case for the non-inverting element antenna as well, the periodic phase-reversal antenna back radiation (radiation in the region $|\phi| > 90°$) in measurements and simulations was lower than the theoretical back radiation. This was due to the fact that the unit-cell pattern did not account for the extended antenna length or the mutual coupling between radiating elements.

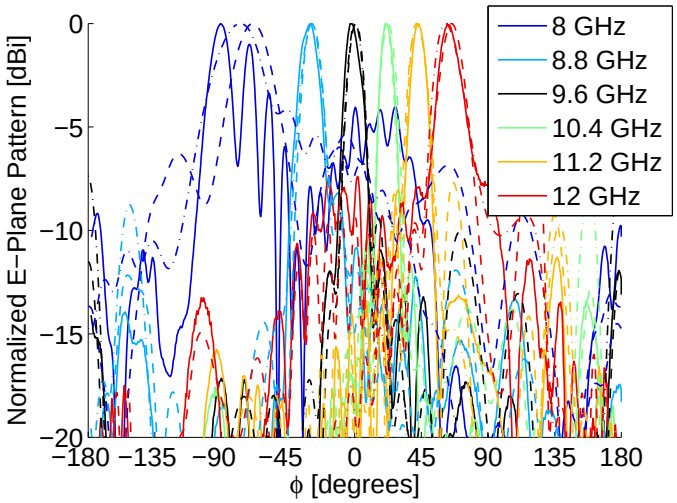

Figure 5.17: Periodic phase-reversal antenna normalized E-plane radiation patterns [dBi]: Measured (———), Simulated (- - -), and Theoretical (- · - ·)

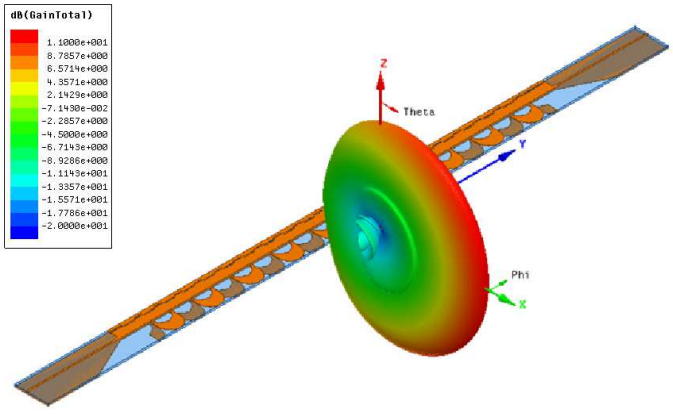

Figure 5.18: Periodic phase-reversal antenna simulated 3-D pattern radiating at broadside

H-plane pattern measurements for the periodic phase-reversal antenna were very difficult to acquire due to the frequency dependence of the H-plane cones (as was explained for the non-inverting element antenna). Instead, simulated normalized H-plane patterns for the periodic phase-reversal antenna are shown Figure 5.19 for a sample of frequencies.

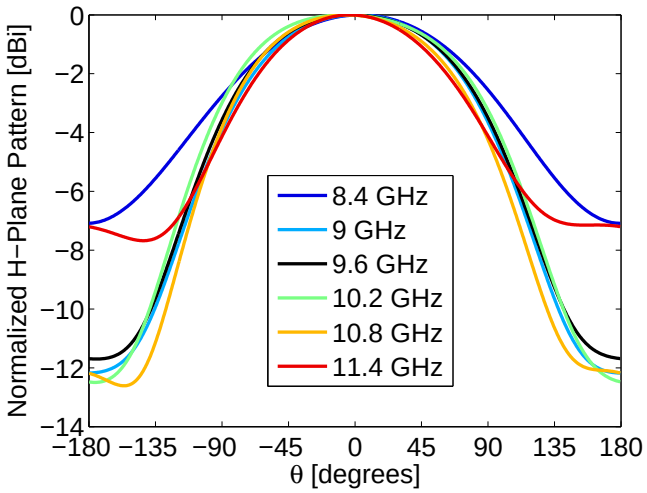

Figure 5.19: Periodic phase-reversal antenna H-plane co-polarized (ϕ) radiation patterns

The periodic phase-reversal antenna polarization (E_ϕ/E_θ) was found in simulations to be greater than 25 dB in the direction of the main beam for all frequencies. The improved polarization of the periodic phase-reversal LWA can be attributed to the fact that θ directed radiation, from adjacent ATSA radiators, cancels out at all frequencies (in the main beam direction) due to the successive polarity inversion of elements.

The main beam angle of the periodic phase-reversal antenna was calculated using the leaky wave phase constant in conjunction with the well known relation $\phi_m = \sin^{-1}\left(\frac{\beta_{-1}}{k_0}\right)$. Results of this computation are shown in Figure 5.20 for both measured and simulated leaky-wavenumbers and are compared to measured and simulated pattern main beam angles. In Figure 5.20 it was observed that the main beam angle prediction was inaccurate for lower frequencies near reverse-endfire (i.e. there was an outlier in measured data observed at 8.2 GHz). The cause of this is uncertain however it is possible that the pattern could have been affected by the coaxial cable feed-line or the antenna holder setup.

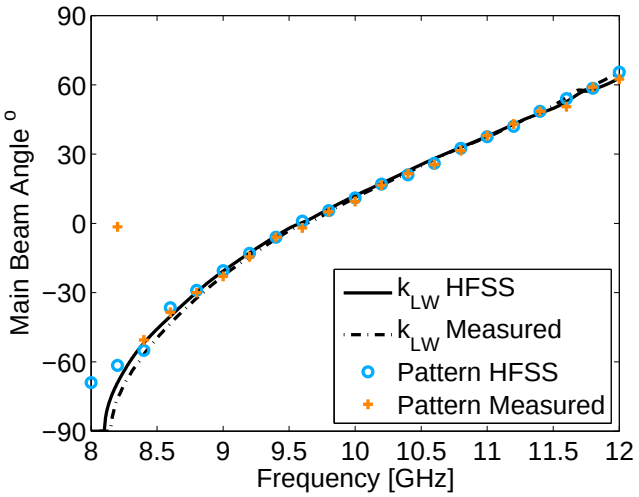

Figure 5.20: Periodic phase-reversal antenna main beam angle

5.5 Antenna Gain and Efficiency

The non-inverting element antenna gain, extracted from simulations and prototype measurements, is shown in Figure 5.21. The simulated antenna efficiency is also presented and was between 52–77% within the antenna impedance bandwidth. The efficiency calculation included power dissipated in the matched load as part of the accepted power. Reflected power was excluded from the calculation (as is customary).

The periodic phase-reversal antenna gain is reported as a function of frequency in Figure 5.22. The simulated efficiency is also shown where again power dissipated in the matched load was included as part of the accepted power and reflected power was excluded.

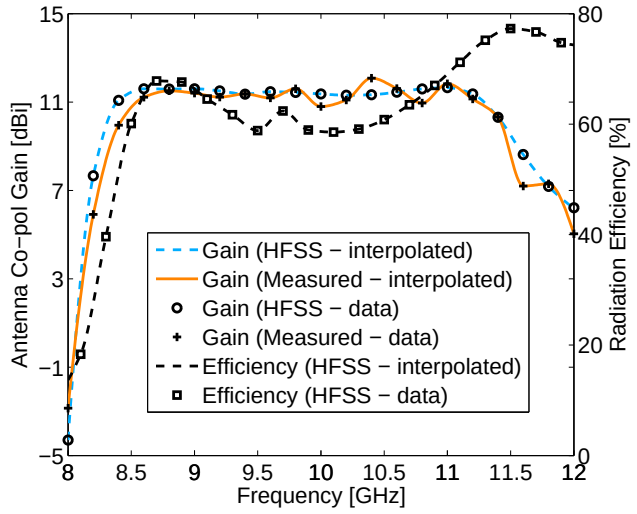

Figure 5.21: Non-inverting element antenna gain and efficiency

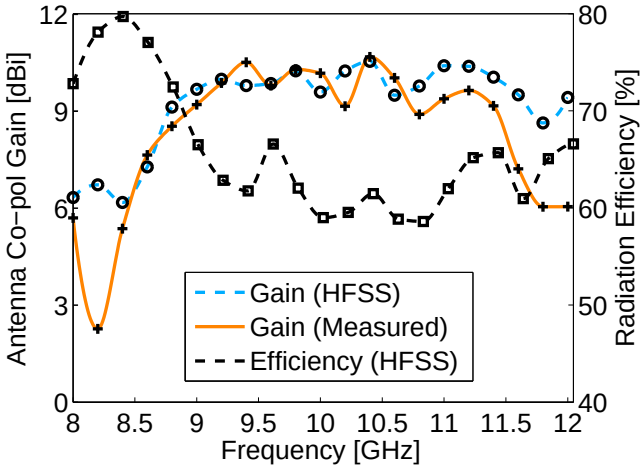

Figure 5.22: Periodic phase-reversal antenna gain and efficiency

5.6 Simulated Permittivity Reduction Results

As has been mentioned previously throughout this thesis, the periodic phase-reversal antenna architecture enables a reduction in the substrate permittivity while maintaining grating lobe free scanning. To further verify and illustrate this point, both the non-inverting element design and the new periodic phase-reversal design were scaled in simulations and the substrate permittivity was changed to $\epsilon_r = 6.15$ (as would be the case in using a Rogers RO3006 substrate). The antenna dimensions were scaled by a factor of $\sqrt{10.96/6.15}$ in order to maintain the same 9.6 GHz broadside frequency. The simulated dispersion curves for relevant space harmonics (Floquet modes) for both antennas are shown in Figure 5.23. Region 1 indicates the fast wave (radiating) region for the periodic phase-reversal antenna and region 2 indicates the fast wave (radiating) region for the non-inverting element design. It was observed that the dispersion curves for the periodic phase-reversal architecture shift by a factor of π and approximately double in slope. This allows the $n = -1$ space harmonic to scan the full space (between points A and B) before the $n = -2$ space harmonic becomes fast and radiating at point C. In contrast, the non-inverting element design's $n = -1$ space harmonic begins to radiate at point D and can only scan until point E without the appearance of grating lobes. Point E corresponds to the frequency at which the $n = -2$ space harmonic becomes fast and radiating.

This was further observed in the simulated radiation patterns of the $\epsilon_r = 6.15$ scaled structures shown in Figure 5.24 where it is seen that the pattern for the non-inverting element design suffers from a reverse endfire grating lobe at 11.5 GHz while the periodic phase-reversal architecture can scan to forward endfire (14 GHz) without the appearance of grating lobes.

Simulated S-parameters for the structures with reduced permittivity are shown in Figures 5.25 and 5.26. In Figure 5.25, the degradation of the antenna return loss near 12.4 GHz indicates an open-stopband associated with the $n = -2$ space harmonic radiating at -45°

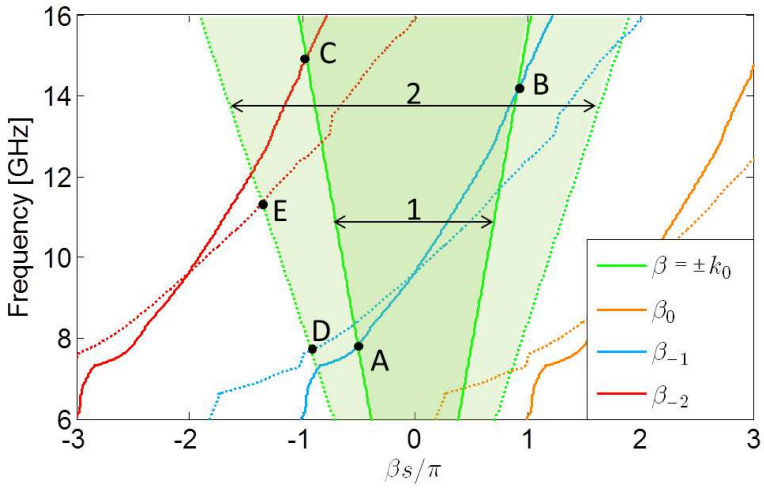

Figure 5.23: $\epsilon_r = 6.15$ dispersion curves: Periodic phase reversal design (———), Non-inverting element design (- - -). For the periodic phase reversal antenna, the $n = -1$ space harmonic scans through region **1** from **A** to **B**, below frequency **C** where the $n = -2$ space harmonic begins radiating. For the non-inverting element antenna, the $n = -1$ space harmonic scans through region **2** starting at **D**, however the pattern will exhibit grating lobes from the $n = -2$ space harmonic above frequency **E**

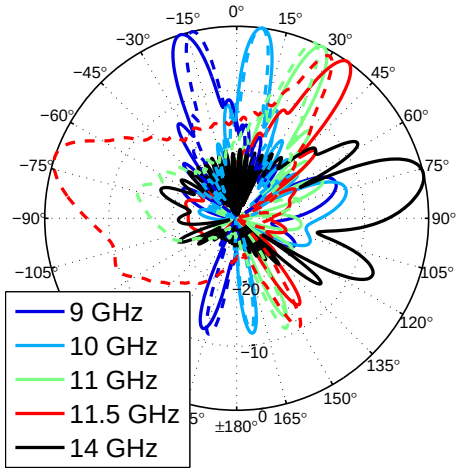

Figure 5.24: $\epsilon_r = 6.15$ normalized radiation patterns [dBi]: Periodic phase reversal design (———), Non-inverting element design (- - -)

and the $n = -1$ space harmonic radiating at $+45°$ (symmetric about the broadside axis). From Figure 5.26, it is seen that forward endfire ($\sim$14 GHz) is within the periodic phase-reversal antenna impedance bandwidth, however reverse endfire is not. With another design iteration the antenna could likely be optimized to offer reverse to forward endfire scanning on a substrate with a relative permittivity as low as $\epsilon_r = 4.5$ as predicted in Appendix C.

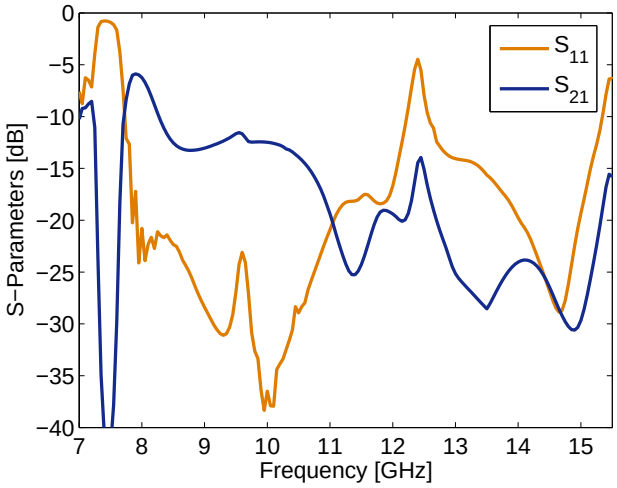

Figure 5.25: Non-inverting element antenna with $\epsilon_r = 6.15$ S-parameters

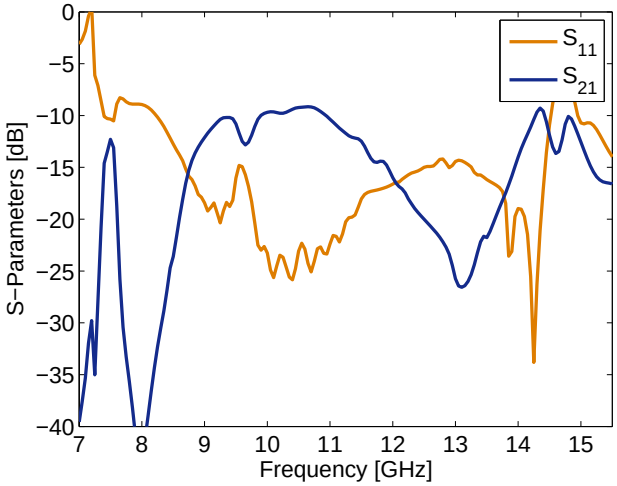

Figure 5.26: Periodic phase-reversal antenna with $\epsilon_r = 6.15$ S-Parameters

5.7 Chapter Summary

In this chapter, prototyping of both the non-inverting element antenna and the periodic phase-reversal antenna was outlined. Measurements of the antenna leaky-wavenumbers were compared to simulated leaky-wavenumbers extracted from HFSS. Of several prototypes, one of each antenna type, (i.e. the non-inverting element antenna and the periodic phase-reversal antenna) offering the closest leaky-wavenumber agreement with simulations, was used in subsequent measurements. Impedance (S-parameter) measurements for the chosen prototypes were very close to simulated results. A 33.4% (compared to 32.6% simulated) impedance bandwidth was observed for the non-inverting element antenna and a 34.1% (compared to 34.7% simulated) impedance bandwidth for the periodic phase-reversal antenna.

The broadside (9.6 GHz) return loss of the non-inverting element antenna prototype was 19 dB (compared to 17 dB simulated) corresponding to a measured broadside gain of 11.1 dBi (compared to 11.4 dBi simulated). The broadside (9.6 GHz) return loss of the periodic phase-reversal antenna prototype was 12 dB (compared to 14.5 dB simulated) corresponding to a measured gain of 9.7 dBi (compared to 9.8 dBi simulated). The lower broadside return loss of the periodic phase-reversal antenna was somewhat expected. It is likely that the high mutual coupling of adjacent elements in the periodic phase-reversal antenna reduced the effectiveness of the unit-cell matching network with many cascaded unit-cells. To correct this in the future, the unit-cell matching network optimization should be done with many cascaded unit-cells (at the cost of reduced computational efficiency). Even without further optimization, the unit-cell matching technique used for broadside open-stopband mitigation was deemed successful for both designs.

Antenna radiating performance was verified through E-plane co-polarized radiation pattern and gain measurements. Both antennas exhibited beam steering through broadside without significant pattern or gain degradation. Simulated H-plane patterns for the antennas combined with E-plane patterns define a frequency scanning fan shape beam with

maximum radiation in the plane of the substrate. From simulations, cross-polarization was less than -15 dB and -25 dB for the non-inverting element antenna and the periodic phase-reversal antenna, respectively. The radiation efficiency of each antenna was extracted from simulations, and was between 52-77% for the non-inverting element antenna, and between 58-80% for the periodic phase reversal antenna. The measured non-inverting element antenna gain was greater than 10 dB over an 86° scan range, while the measured periodic phase reversal antenna gain was greater than 9 dB over a 72° scan range, both antennas including broadside. The measured E-plane patterns and gain values were compared to simulations and theoretical radiation patterns from Chapter 4.

The main beam angle as a function of frequency was in good agreement for all investigative techniques, except for a single measured outlier for the periodic phase-reversal antenna at 8.2 GHz, where the measured beam angle was 0° instead of the theoretical -65°. At the desired broadside frequency (9.6 GHz), the main beam angle according to measured and simulated leaky wavenumbers, as well as from measured and simulated radiation patterns, all fell between and +0.5° and -1° for the non-inverting element antenna, and between +1° and -2° for the periodic phase-reversal antenna. Radiation patterns were in best agreement in the vicinity of broadside, with increasing gain and pattern deviation as the beam approached reverse and forward endfire. The maximum deviation between the measured and simulated gain for the non-inverting element antenna was 1.8 dB at 8.2 GHz. The maximum gain deviation from simulations for the periodic phase-reversal antenna coincided with the main beam angle outlier at 8.2 GHz, and was 4.8 dB. Within the impedance bandwidth of each antenna (and closer to broadside), the measured gain discrepancy from simulations was reduced to 1.3 dB at 11.6 GHz for the non-inverting element antenna, and to 2.2 dB at 11.8 GHz for the periodic phase-reversal antenna.

A more appropriate antenna range for the electrically large antennas (possibly using a near field measurement facility or a larger anechoic chamber), in a addition to more precise

sensor and AUT mounting and alignment may have improved the agreement between measured and simulated gain values and radiation patterns for all frequencies. Also, simulations may have been improved by adding environmental factors such as the coaxial cable feed-line, the antenna holding structure, and the matched load termination, at the cost of significantly increased simulation times.

Although the power handling capacity of the proposed antennas was not investigated, SIW has a relatively high power handling capacity (much higher than microstrip) [5] and so it is likely that the power handling of the proposed antennas is also high.

Finally the impact of substrate permittivity reduction on antenna performance was investigated for both antennas by scaling the structures in simulations and changing the substrate permittivity to $\epsilon_r = 6.15$. As was expected, the non-inverting element antenna scan range became severely limited by the appearance of grating lobes, whereas the periodic phase-reversal antenna was allowed to scan to forward endfire without the appearance of grating lobes, thus exhibiting the main advantage of the periodic phase-reversal antenna architecture.

Chapter 6

Conclusion and Future Work

As was emphasized in the introduction of this thesis, research in the area of SIW based hardware development is a response to the need for planar circuitry with mm-wave frequency scalability [3]. The success of SIW in meeting this need at a system level will largely rely on designers having a wealth of SIW based components to choose from, including antennas. As a result, this thesis has presented the study of a new broadside scanning HMSIW periodic LWA as well as a periodic phase-reversal version of the new antenna. Both antennas would likely be well suited for high resolution mm-wave radar applications as well as for atmospheric weather and temperature sensing applications.

6.1 Thesis Achievements and Contributions

In an effort to meet the goals of this thesis outlined in Chapter 1, the following key achievements and contributions were made:

- Two new SIW based broadside scanning periodic LWA architectures have been proposed. These antennas were the first broadside scanning LWAs in SIW to offer maximum radiation in the plane of the substrate. They were also among the first SIW based periodic LWAs to offer broadside radiation in addition to a wide scan range (the only other one found in literature that did not use the CRLH approach was presented in [17]).

- The design procedures for the proposed antenna architectures were provided in detail in Chapter 4. A generalized summary of the design procedure was outlined in Section 4.7 in the hopes that it may be followed in order to realize different structures oper-

ating under similar broadside scanning periodic LWA theory (e.g. upon realization of different periodic radiator or unit-cell matching section geometries).

- Both of the new antennas used the unit-cell matching technique to enable broadside scanning performance and thus verified the open-stopband mitigation technique in SIW for the first time.

- The proposed periodic phase-reversal LWA was the first periodic phase-reversal LWA to be realized in SIW. The main benefits of the periodic phase-reversal technique are size reduction and the potential for substrate permittivity reduction while maintaining grating lobe free scanning. Both of these potential benefits were verified for the new antenna.

- In order to enable full-space scanning without grating lobes, minimum permittivity conditions for TEM transmission line based periodic and periodic phase-reversal LWAs have been derived by [19] as outlined in Chapter 2. These conditions are more restrictive for non-TEM waveguides however no exact conditions had been derived due to the dependence of dispersion characteristics on both the substrate permittivity and the waveguide cutoff frequency. For this reason, conditions for grating lobe free scanning in waveguide based periodic and periodic phase-reversal LWAs were derived as shown in Appendix C for a desired broadside frequency to waveguide cutoff frequency ratio f_b/f_c.

As mentioned in Chapter 1, these thesis contributions resulted in two international conference publications and two journal publications listed here:

- Preliminary simulated and measured results for the non-inverting element antenna were presented at the 2014 European Conference on Antennas and Propagation for which conference proceedings were published in [20].

- Finalized design, simulations, and prototype measurements for the non-inverting element antenna (primarily outlined in Chapters 3 and 5) were published with IEEE in the Antennas and Wirelesss Propagation Letters journal [13].

- Preliminary simulated and measured results for the periodic phase-reversal antenna were presented at the 2014 International Symposium on Antennas and Propagation for which conference proceedings were published in [18].

- Finalized design, simulations, and prototype measurements for the periodic phase-reversal antenna (primarily outlined in Chapters 3 and 5) have been submitted for publication with IEEE in the Antennas and Wirelesss Propagation Letters journal. The publication is currently pending approval.

6.2 Antenna Limitations and Future Work

As with almost all bodies of research, this thesis does leave room for improvement and should be seen as the first iteration of design and prototyping for the periodic and periodic phase-reversal antennas presented. As such, the following suggested future work and research could help to improve the antenna designs and further generalize and expedite the design procedures:

- The end goal of most research in the area of SIW components is to enable the design of SIW based systems in the mm-wave frequency range. For this reason the proposed structures should be scaled and tested for use in the mm-wave frequency range (30-300 GHz).

- A formal comparison of SIW based CRLH metamaterial versus periodic LWAs should be conducted. One anticipated advantage of the CRLH approach is that no lower limit exists for the substrate permittivity for grating lobe free scanning. Speculated disad-

vantages of the CRLH approach include computational complexity in the design phase, and higher conductor losses due to large currents in operation near SIW cutoff. [11]

- As is described in [14], tapering of the radiating aperture amplitude distribution can help to improve directivity and side-lobe levels in LWAs, and thus future design iterations of the proposed antennas could make use of this concept to improve radiation patterns.

- The ATSA radiating element and unit-cell matching section designs in this thesis were optimization based. In the future, to reduce design times, it may be useful to perform thorough parametric studies of the radiating element and matching section geometries and the resulting unit-cell performance.

- Antenna radiation pattern and gain measurements were sensitive to even low dielectric materials coming into contact with the structures, meaning that polystyrene foam had to be used to mount the antennas for measurements. Re-designing the antennas with the inclusion of a stronger antenna holder material would help to simplify the antenna measurement setup and would enable measurement of H-plane patterns. Also a measurement setup with a higher dynamic range would help to speed up measurement times and to characterize low side-lobe levels of the antennas as well as cross-polarization.

- In the future, it would be interesting to validate the performance of the periodic phase-reversal antenna with a reduced substrate permittivity through prototyping.

- In a future design iteration of the non-inverting element antenna, better choice of the broadside frequency to cutoff frequency ratio, in addition to a wider bandwidth radiating element optimization, may enable reverse to forward endfire scanning. A wider bandwidth radiating element optimization may also enable reverse to forward endfire scanning of the periodic phase-reversal antenna within its impedance bandwidth.

- The periodic phase-reversal antenna simulation with a reduced substrate permittivity was observed to offer forward endfire radiation within the impedance bandwidth of the antenna despite the radiating element pattern having weak radiation in the endfire direction. One hypothetical explanation is that a radiating surface wave mode could be excited as scan-angles approach endfire. A study on the mechanism by which endfire radiation is allowed by the proposed antennas may lead to designs offering a high gain from reverse to forward endfire.

Bibliography

[1] W. Stutzman and G. Thiele, *Antenna Theory and Design*, 3rd ed. John Wiley & Sons, 2013.

[2] N. Weste and D. Harris, *CMOS VLSI Design: A Circuits and Systems Perspective*, 4th ed. Addison-Wesley, 2011.

[3] M. Bozzi, A. Georgiadis, and K. Wu, "Review of substrate-integrated waveguide circuits and antennas," *IET Microwaves, Antennas & Propagation*, vol. 5, no. 8, p. 909, 2011.

[4] D. Deslandes and K. Wu, "Integrated microstrip and rectangular waveguide in planar form," *IEEE Microwave and Wireless Components Letters*, vol. 11, no. 2, pp. 68–70, Feb. 2001.

[5] Y. J. Cheng, K. Wu, and W. Hong, "Power handling capability of substrate integrated waveguide interconnects and related transmission line systems," *IEEE Transactions on Advanced Packaging*, vol. 31, no. 4, pp. 900–909, Nov 2008.

[6] D. R. Jackson, C. Caloz, and T. Itoh, "Leaky-Wave Antennas," *Proceedings of the IEEE*, vol. 100, no. 7, pp. 2194–2206, Jul. 2012.

[7] P. Burghignoli, G. Lovat, and D. Jackson, "Analysis and Optimization of Leaky-Wave Radiation at Broadside From a Class of 1-D Periodic Structures," *IEEE Transactions on Antennas and Propagation*, vol. 54, no. 9, pp. 2593–2604, 2006.

[8] G. Lovat, P. Burghignoli, and D. Jackson, "Fundamental Properties and Optimization of Broadside Radiation From Uniform Leaky-Wave Antennas," *IEEE Transactions on Antennas and Propagation*, vol. 54, no. 5, pp. 1442–1452, May 2006.

[9] A. Sutinjo, "Analysis and design of printed leaky-wave antennas for broadside radiation," PhD, University of Calgary, 2009.

[10] C. Caloz, T. Itoh, and A. Rennings, "CRLH metamaterial leaky-wave and resonant antennas," *IEEE Antennas and Propagation Magazine*, vol. 50, no. 5, pp. 25–39, Oct. 2008.

[11] Y. Dong and T. Itoh, "Composite right/left-handed substrate integrated waveguide and half mode substrate integrated waveguide leaky-wave structures," *IEEE Transactions on Antennas and Propagation*, vol. 59, no. 3, pp. 767–775, 2011.

[12] W. Hong, B. Liu, Y. Wang, and Q. Lai, "Half mode substrate integrated waveguide: A new guided wave structure for microwave and millimeter wave application," in *Joint 31st International Conference on Infrared Millimeter Waves and 14th International Conference on Teraherz Electronics*, vol. 152, 2006, p. 4244.

[13] R. Henry and M. Okoniewski, "A Broadside Scanning Half Mode Substrate Integrated Waveguide Periodic Leaky Wave Antenna," *IEEE Antennas and Wireless Propagation Letters*, vol. 13, pp. 1429–1432, 2014.

[14] A. Oliner and D. Jackson, *Antenna Engineering Handbook, Chapter 11: Leaky-Wave Antennas*, 4th ed. McGraw-Hill, 2007.

[15] S. Paulotto, P. Baccarelli, F. Frezza, and D. R. Jackson, "A novel technique for open-stopband suppression in 1-D periodic printed leaky-wave antennas," *IEEE Transactions on Antennas and Propagation*, vol. 57, no. 7, pp. 1894–1906, 2009.

[16] T. Cameron, A. Sutinjo, and M. Okoniewski, "A circularly polarized broadside scanning patch array," in *2010 Proceedings of the Fourth European Conference on Antennas and Propagation (EuCAP)*, 2010, pp. 1–3.

[17] A. Guntupalli and K. Wu, "Multi-dimensional scanning multi-beam array antenna fed by integrated waveguide butler matrix," in *2012 IEEE MTT-S International Microwave Symposium Digest (MTT)*, June 2012, pp. 1–3.

[18] R. Henry and M. Okoniewski, "Half Mode Substrate Integrated Waveguide Periodic Leaky Wave Antenna With Antipodal Tapered Slots," in *Antennas and Propagation Society International Symposium (APSURSI)*, 2014, pp. 1284–1285.

[19] N. Yang, C. Caloz, and K. Wu, "Full-space scanning periodic phase-reversal leaky-wave antenna," *IEEE Transactions on Microwave Theory and Techniques*, vol. 58, no. 10, pp. 2619–2632, 2010.

[20] R. Henry and M. Okoniewski, "A New Half Mode Substrate Integrated Waveguide Leaky Wave Antenna," in *The 8th European Conference on Antennas and Propagation (EuCAP 2014)*, no. EuCAP, 2014, pp. 586–589.

[21] L. Yan, W. Hong, K. Wu, and T. Cui, "Investigations on the propagation characteristics of the substrate integrated waveguide based on the method of lines," *IEE Proceedings Microwaves, Antennas and Propagation*, vol. 152, no. 1, pp. 35–42, 2005.

[22] Y. Cassivi, L. Perregrini, P. Arcioni, M. Bressan, K. Wu, and G. Conciauro, "Dispersion characteristics of substrate integrated rectangular waveguide," *IEEE Microwave and Wireless Components Letters*, vol. 12, no. 9, pp. 333–335, Sep. 2002.

[23] F. Xu and K. Wu, "Guided-wave and leakage characteristics of substrate integrated waveguide," *IEEE Transactions on Microwave Theory and Techniques*, vol. 53, no. 1, pp. 66–73, 2005.

[24] D. Pozar, *Microwave Engineering*, 3rd ed. John Wiley & Sons, 2005.

[25] C. Balanis, *Advanced Engineering Electromagnetics*, 1st ed. John Wiley & Sons, 1989.

[26] D. Deslandes and K. Wu, "Design Consideration and Performance Analysis of Substrate Integrated Waveguide Components," in *32nd European Microwave Conference, 2002*, no. 2, Oct. 2002, pp. 1–4.

[27] Q. Lai, W. Hong, and Z. Kuai, "Half-mode substrate integrated waveguide transverse slot array antennas," *IEEE Transactions on Antennas and Propagation*, vol. 57, no. 4, pp. 1064–1072, 2009.

[28] A. Sutinjo, M. Okoniewski, and R. Johnston, "Radiation from fast and slow traveling waves," *IEEE Antennas and Propagation Magazine*, vol. 50, no. 4, pp. 153–154, 2008.

[29] A. Oliner and D. Jackson, *Modern Antenna Handbook, Chapter 7: Leaky-Wave Antennas*, C. Balanis, Ed. John Wiley & Sons, 2008.

[30] W. Hansen, "Radiating electromagnetic wave guide," Jun. 25 1946, uS Patent 2,402,622.

[31] J. Hines, V. Rumsey, and C. Walter, "Traveling-wave slot antennas," *Proceedings of the IRE*, vol. 40, pp. 1181–1188, 1953.

[32] A. Sutinjo, M. Okoniewski, and R. Johnston, "Suppression of the slot-mode radiation in a slitted waveguide using periodic slot perturbations," *Antennas and Wireless Propagation Letters, IEEE*, vol. 8, pp. 550–553, 2009.

[33] R. Gilbert, *Antenna Engineering Handbook, Chapter 9: Waveguide Slot Antenna Arrays*, 4th ed. McGraw-Hill, 2007.

[34] R. Collin, *Foundations for Microwave Engineering*, 2nd ed. John Wiley & Sons, 2007.

[35] C. Caloz and T. Itoh, "Array factor approach of leaky-wave antennas and application to 1-D/2-D composite right/left-handed (CRLH) structures," *IEEE Microwave and wireless components letters*, vol. 14, no. 6, pp. 274–276, 2004.

[36] P. Baccarelli and S. Paulotto, "A new Brillouin dispersion diagram for 1-D periodic printed structures," *IEEE Transactions on Microwave Theory and Techniques*, vol. 55, no. 7, pp. 1484–1495, 2007.

[37] A. Lai, T. Itoh, and C. Caloz, "Composite right/left-handed transmission line metamaterials," *Microwave Magazine, IEEE*, no. September, pp. 34–50, 2004.

[38] M. Guglielmi and D. Jackson, "Broadside radiation from periodic leaky-wave antennas," *IEEE Transactions on Antennas and Propagation*, vol. 41, no. 1, pp. 31–37, 1993.

[39] M. Mujumdar, A. Alphones, J. Cheng, and Nasimuddin, "Compact leaky wave antenna with periodical slots on substrate integrated waveguide," in *8th European Conference on Antennas and Propagation (EuCAP)*, April 2014, pp. 766–770.

[40] Q. Yang, Y. Zhang, and X. Zhang, "X-band composite right/left-handed leaky wave antenna with large beam scanning-range/bandwidth ratio," *Electronics Letters*, vol. 48, no. 13, pp. 746–747, 2012.

[41] Y. Mizumori and K. Okubo, "Backfire-to-endfire radiation characteristics of CRLH-TL using substrate integrated waveguide and metal-patches," in *Asia Pacific Microwave Conference*, 2009, pp. 1419–1422.

[42] C. Jin and A. Alphones, "Leaky-wave radiation behavior from a double periodic composite right/left-handed substrate integrated waveguide," *IEEE Transactions on Antennas and Propagation*, vol. 60, no. 4, pp. 1727–1735, 2012.

[43] Z. Chen and X. Qing, "Multilayered Composite Right/Left-Handed Leaky-Wave Antenna With Consistent Gain," *IEEE Transactions on Antennas and Propagation*, vol. 60, no. 11, pp. 5056–5062, 2012.

[44] H. Lee, J. Choi, Y. Kasahara, and T. Itoh, "A circularly polarized single radiator leaky-wave antenna based on crlh-inspired substrate integrated waveguide," in *2014 IEEE MTT-S International Microwave Symposium (IMS)*, June 2014, pp. 1–3.

[45] Y. Dong and T. Itoh, "Substrate Integrated Composite Right-/Left-Handed Leaky-Wave Structure for Polarization-Flexible Antenna Application," *IEEE Transactions on*

Antennas and Propagation, vol. 60, no. 2, pp. 760–771, 2012.

[46] J. Machac and M. Polivka, "A dual band SIW leaky wave antenna," in *IEEE MTT-S International Microwave Symposium Digest*, Jun. 2012, pp. 1–3.

[47] J. Liu, D. Jackson, and Y. Long, "Substrate integrated waveguide (SIW) leaky-wave antenna with transverse slots," *IEEE Transactions on Antennas and Propagation*, vol. 60, no. 1, pp. 20–29, 2012.

[48] D. Deslandes and K. Wu, "Substrate integrated waveguide leaky-wave antenna: concept and design considerations," in *Asia Pacific Microwave Conference*, 2005, pp. 1–3.

[49] A. Martinez-Ros, J. Gomez-Tornero, and G. Goussetis, "Planar leaky-wave antenna with flexible control of the complex propagation constant," *IEEE Transactions on Antennas and Propagation*, vol. 60, no. 3, pp. 1625–1630, 2012.

[50] J. Xu, W. Hong, H. Tang, Z. Kuai, and K. Wu, "Half-mode substrate integrated waveguide (HMSIW) leaky-wave antenna for millimeter-wave applications," *IEEE Antennas and Wireless Propagation Letters*, vol. 7, pp. 85–88, 2008.

[51] F. Xu, K. Wu, and X. Zhang, "Periodic leaky-wave antenna for millimeter wave applications based on substrate integrated waveguide," *IEEE Transactions on Antennas and Propagation*, vol. 58, no. 2, pp. 340–347, 2010.

[52] Q. Lai, C. Fumeaux, and W. Hong, "Periodic leaky-wave antennas fed by a modified half-mode substrate integrated waveguide," *IET Microwaves, Antennas & Propagation*, vol. 6, no. 5, p. 594, 2012.

[53] Y. Cheng, W. Hong, and K. Wu, "Millimeter-wave half mode substrate integrated waveguide frequency scanning antenna with quadri-polarization," *IEEE Transactions on Antennas and Propagation*, vol. 58, no. 6, pp. 1848–1855, 2010.

[54] A. Suntives and S. Hum, "A fixed-frequency beam-steerable half-mode substrate integrated waveguide leaky-wave antenna," *IEEE Transactions on Antennas and Propagation*, vol. 60, no. 5, pp. 2540–2544, 2012.

[55] P. Anju, A. Lindo, C. Aanandan, D. Krishna, and P. Young, "Novel Millimeter-Wave Antenna Array Using Half Mode Substrate Integrated Waveguide (HMSIW)," *2012 International Conference on Advances in Computing and Communications*, pp. 274–277, 2012.

[56] Q. Zhang and Y. Lu, "45 Linearly Polarized Substrate Integrated Waveguide-Fed Slot Array Antennas," in *2008 International Conference on Microwave and Millimeter Wave Technology*, Apr. 2008, pp. 1214–1217.

[57] "RO3200 Series Circuit Materials Data Sheet," *Rogers Corporation*.

[58] J. Siddiqui and Y. Antar, "Design of an ultrawideband antipodal tapered slot antenna using elliptical strip conductors," *IEEE Antennas and Wireless Propagation Letters*, vol. 10, pp. 251–254, 2011.

[59] T. A. Milligan, *Modern Antenna Design, Chapter 10: Traveling-Wave Antennas*, 2nd ed. John Wiley & Sons, Apr. 2005.

[60] R. . ANSYS ®Academic Research, *Help System*. ANSYS, Inc.

[61] G. Engen and C. Hoer, "Thru-reflect-line: An improved technique for calibrating the dual six-port automatic network analyzer," *IEEE Transactions on Microwave Theory and Techniques*, vol. MTT-27, no. 12, pp. 987–993, 1979.

[62] J. E. Schutt-Aine, "Automated Microwave Measurements: TRL Calibration," *University of Illinois ECE 451 Lecture Slides*.

[63] D. Deslandes, "Design equations for tapered microstrip-to-Substrate Integrated Waveguide transitions," in *2010 IEEE MTT-S International Microwave Symposium*, May 2010, pp. 704–707.

[64] K. Lu, "An efficient method for analysis of arbitrary nonuniform transmission lines," *IEEE Transactions on Microwave Theory and Techniques*, vol. 45, no. 1, pp. 9–14, 1997.

[65] E. Lindgren, "Model 3160 Series Pyramidal Horn Antennas Manual," 2003.

Appendix A

Periodic Analysis for Leaky-Wavenumber and Bloch Impedance Extraction from Simulations and Measurements

The analysis presented in this appendix was found in [34] and [24], and is general to periodic structures. Both books are good references for a more thorough background in periodic structures.

A.1 Leaky-Wavenumber Computation

For any periodic structure, a propagation constant defining the voltage/current phase and amplitude periodically along the structure can be extracted from the Eigenvalues of the transmission matrix of an integer number of unit-cells using the following procedure.

First assume the following definitions: Forward propagating waves at the n and $n+1$ terminals have amplitudes c_n^+ and c_{n+1}^+ respectively. Backward traveling waves at the n and $n+1$ terminals have amplitudes c_n^- and c_{n+1}^- respectively. Then, the wave amplitudes at the n and $n+1$ terminals can be related by:

$$\begin{bmatrix} c_n^+ \\ c_n^- \end{bmatrix} = \begin{bmatrix} T_{11} & T_{12} \\ T_{21} & T_{22} \end{bmatrix} \begin{bmatrix} c_{n+1}^+ \\ c_{n+1}^- \end{bmatrix}. \tag{A.1}$$

Assuming that the periodic amplitude and phase shift is the same for every unit-cell (as is true for infinite periodic structures), we can define $k_{LW} = \beta - j\alpha$ as the propagation constant defining these relations (i.e. $c_{n+1}^+ = e^{-jk_{LW}Ns}c_n^+$ and $c_{n+1}^- = e^{-jk_{LW}Ns}c_n^-$ where Ns

is the length of N unit-cells with individual length s). Then, equation A.1 becomes:

$$\begin{bmatrix} T_{11} - e^{jk_{LW}Ns} & T_{12} \\ T_{21} & T_{22} - e^{jk_{LW}Ns} \end{bmatrix} \begin{bmatrix} c_{n+1}^{+} \\ c_{n+1}^{-} \end{bmatrix} = 0 \tag{A.2}$$

which corresponds with matrix Eigenvalue definition $\Lambda = e^{jk_{LW}Ns}$. Nontrivial solutions require that the determinant of the matrix be zero, which leads to the following relations:

$$T_{11}T_{22} - T_{12}T_{21} + e^{2jk_{LW}Ns} - e^{jk_{LW}Ns}\left(T_{11} + T_{22}\right) = 0 \tag{A.3}$$

$$\Lambda_{1,2} = e^{jk_{LW}Ns} = \frac{T_{11} + T_{22} \pm \sqrt{\left(T_{11} + T_{22}\right)^2 - 4\left(T_{11}T_{22} - T_{12}T_{21}\right)}}{2} \tag{A.4}$$

$$k_{LW1,2} = -j\frac{ln\Lambda_{1,2}}{Ns} \tag{A.5}$$

Now, $k_{LW1,2}$ (and corresponding $\Lambda_{1,2}$) solutions require some interpretation in order to accurately obtain α and β. Firstly, values of k_{LW} with negative α values are chosen from $k_{LW1,2}$ (or $jk_{LW1,2}$ values with positive α) since these values correspond to forward traveling waves. Then, if there are a large number of unit-cells N, the phase of $\Lambda = e^{jk_{LW}Ns}$ must be unwrapped. Firstly, Λ can be written in phasor form as:

$$\begin{aligned} \Lambda &= e^{jk_{LW}Ns} \\ &= e^{\alpha Ns}e^{j\beta Ns} \\ &= e^{\alpha Ns}\angle\beta Ns \end{aligned} \tag{A.6}$$

from which,

$$\beta = \frac{\angle\Lambda}{Ns}. \tag{A.7}$$

Unwrapping the phase requires a reference frequency where the phase shift is known. The easiest way to obtain this information is through simulations ($\angle S_{21}$ data) as was done in this thesis.

A.2 Bloch Impedance Computation

When the propagation constant of a periodic structure is calculated, the ratio of c_n^+ to c_n^- becomes fixed. This ratio can be defined as a reflection reflection coefficient:

$$\Gamma_B = c_n^+ / c_n^-. \tag{A.8}$$

Using this reflection coefficient, the transverse electric field of the Bloch wave (or Floquet mode) will have amplitude

$$V_{Bn} = c_n^+ + c_n^- = c_n^+(1+\Gamma_B) = c_0^+(1+\Gamma_B)e^{-jk_{LW}ns} \tag{A.9}$$

at the n^{th} plane. Similarly,

$$I_{Bn} = c_0^+(1-\Gamma_B)e^{-jk_{LW}ns}. \tag{A.10}$$

Then,

$$Z_B = \frac{V_{Bn}}{I_{Bn}} = \frac{1+\Gamma_B}{1-\Gamma_B}, \tag{A.11}$$

showing that the wave impedance at some periodic boundary is constant and called the Bloch impedance.

The Bloch impedance can be solved from known transmission parameters or ABCD parametrs of N cascaded unit cells. As with the periodic structure wavenumber analysis, assume a Bloch wave (Floquet mode) with required solutions of the form $c_{n+1}^+ = e^{-jk_{LW}Ns}c_n^+$

and $c_{n+1}^{-} = e^{-jk_{LW}Ns}c_n^{-}$. Substituting voltage and current into the forward and reverse traveling wave amplitudes (i.e. $c_{n+1}^{+} = V_{n+1}$ and $c_{n+1}^{-} = I_{n+1}$) in equation A.2 results in:

$$\begin{bmatrix} A - e^{jk_{LW}Ns} & B \\ C & D - e^{jk_{LW}Ns} \end{bmatrix} \begin{bmatrix} V_{n+1} \\ I_{n+1} \end{bmatrix} = 0 \tag{A.12}$$

which can be re-written as:

$$\begin{aligned} \left(A - e^{jk_{LW}Ns}\right) V_{n+1} &= -BI_{n+1} \\ -CV_{n+1} &= \left(D - e^{jk_{LW}Ns}\right) I_{n+1}. \end{aligned} \tag{A.13}$$

Now, defining the Bloch impedance as the voltage to current ratio at terminal $n+1$, we arrive at:

$$\frac{Z_B}{Z_0} = \frac{V_{n+1}}{I_{n+1}} = \frac{-B}{A - e^{jk_{LW}Ns}} = -\frac{D - e^{jk_{LW}Ns}}{C} \tag{A.14}$$

from which:

$$2e^{jk_{LW}Ns} = A + D \pm \sqrt{(A+D)^2 - 4}. \tag{A.15}$$

Back substitution of this result into equation A.13 results in:

$$Z_B^{\pm} = \frac{2BZ_0}{D - A \pm \sqrt{(A+D)^2 - 4}} \tag{A.16}$$

which is the equation used in this thesis for Bloch impedance computations. The $\pm$ superscript indicates that the Bloch impedance for forward or reverse traveling waves will be different. Note that T parameters and ABCD parameters can be interchanged in all the analysis in this appendix.

Appendix B

Thru-Reflect-Line (TRL) Calibration and Deembedding

Figure B.1 illustrates the problem that is addressed by TRL calibration, being that often it is desirable to characterize an electrical network which is embedded within some feed network. In order to remove the effects of the feed network mismatches, losses and phase shifts, TRL calibration can be used [61].

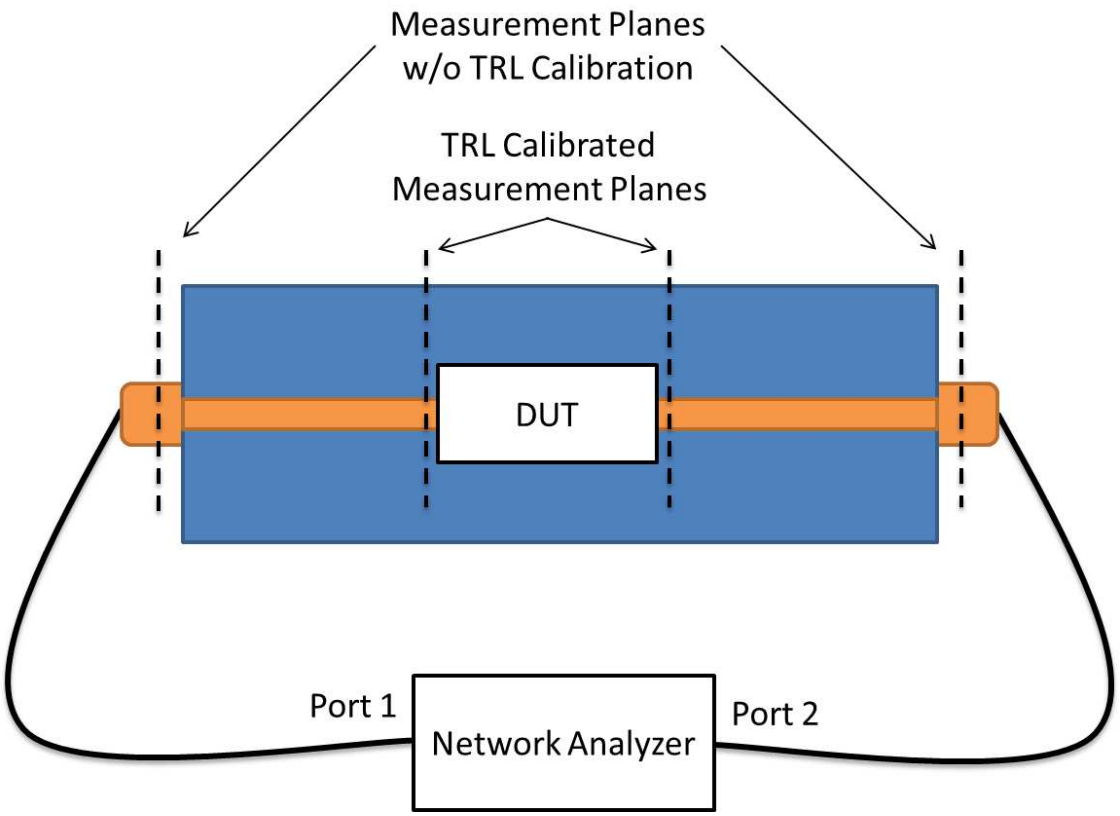

Figure B.1: Embedded DUT to be measured using a network analyzer and TRL calibration

The DUT measurement problem illustrated in Figure B.1 can be formulated as an equivalent mathematical problem shown in Figure B.2. The goal of TRL calibration is to obtain network parameters of error boxes A and B in Figure B.2 (representing unwanted transitions)

and remove their effects from DUT measurements. To do this, measurement of Thru, Line and Reflect standards with identical connectors and unwanted transitions as those to desired to be removed from DUT measurements can be used. TRL standards that could be used for correcting measurements from Figure B.1 are shown in Figure B.3. The Line standard should be a quarter wavelength at the geometric mean frequency of the desired correction band in order to minimize residual error over the band.

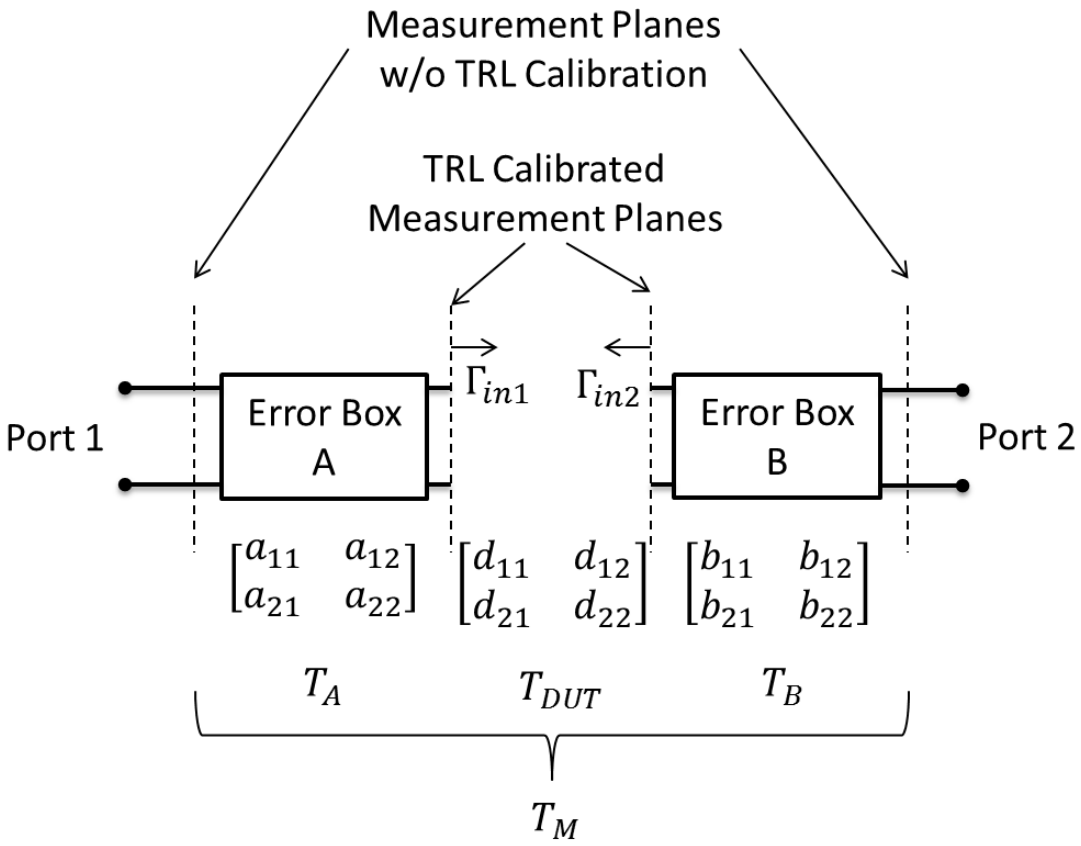

Figure B.2: Mathematically equivalent DUT measurement problem

With TRL standards fabricated, measurements shown in Figure B.4 must be taken for the Thru, Line and Reflect standards in addition to the uncorrected DUT measurement. Ideally, all measurements should be taken using the same test fixture and being careful to avoid cable movement between measurements.

S-parameter measurements of the TRL standards can be converted to T-parameters and

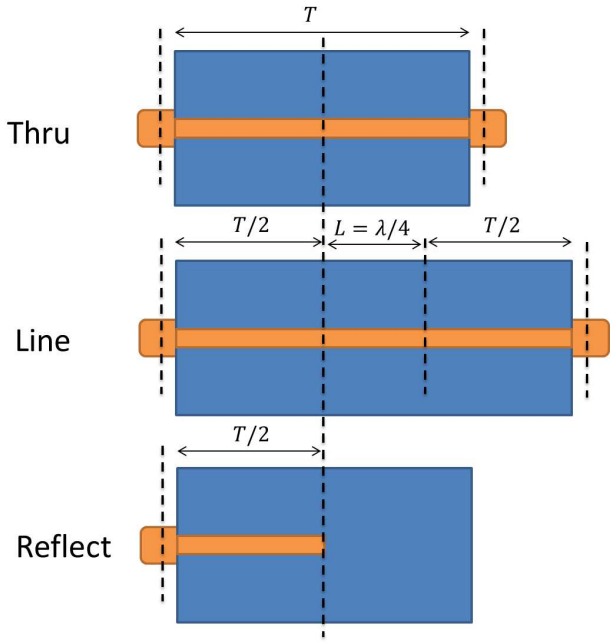

Figure B.3: TRL standards for DUT measurement correction

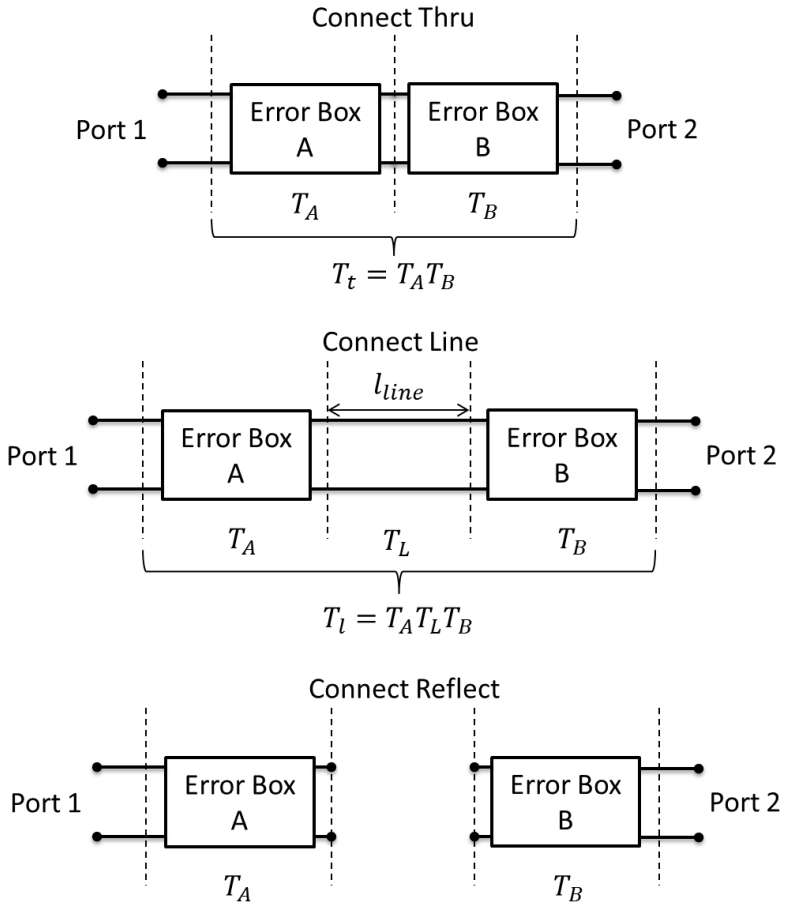

Figure B.4: Measurements of TRL standards

processed as shown in [62] and, [61] to obtain error box T-parameters T_A and T_B. Then, the uncorrected device measurement given by:

$$T_M = T_A T_{DUT} T_B, \tag{B.1}$$

can be corrected to obtain T_{DUT} as shown in equation B.2.

$$T_{DUT} = T_A^{-1} T_M T_B^{-1} \tag{B.2}$$

The TRL standards shown in Figure B.5 were used to remove the connector to microstrip transitions from antenna S-parameter measurements in this thesis.

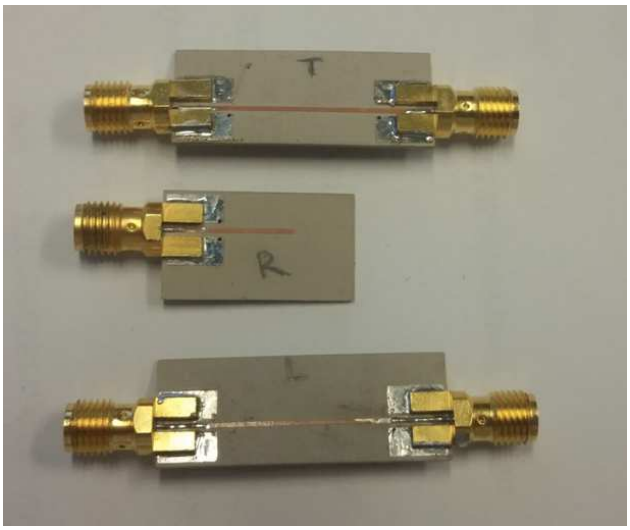

Figure B.5: Fabricated TRL Calibration Kit

Now, as was explained in Appendix A, periodic analysis of measured or simulated data requires measurement planes to lie on a periodic boundary of the structure. Therefore, to measure the leaky-wavenumber of the fabricated antennas, the microstrip to HMSIW transition had to be de-embedded from measurements as well. Due to the good agreement between simulations and fabricated prototypes, it was deemed acceptable to use simulated data to remove the transitions. The transition simulation environments are shown in Figure B.6. Individual transitions had to be simulated for the input and output of both the non-inverting

element antenna and the periodic phase-reversal antenna due to differing distances from the TRL calibrated measurement plane to the periodic boundary of the structure.

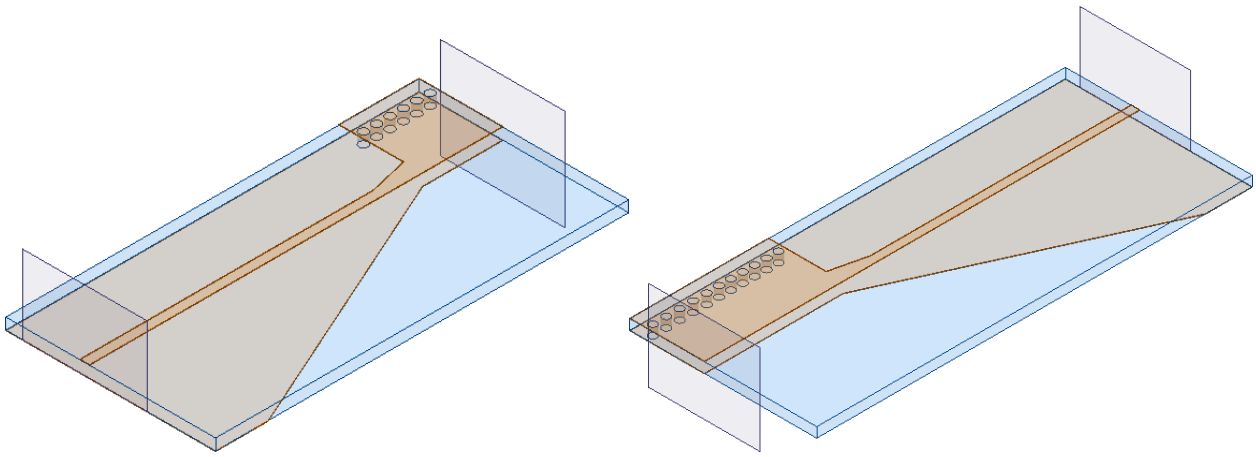

(a) Input microstrip to HMSIW transition (b) Output HMSIW to microstrip transition

Figure B.6: Non-inverting element antenna input and output microstrip to HMSIW transition de-embedding simulation environments

The simulated T-parameters of the transitions were then used to move the measurement planes to lie on the outermost periodic boundaries of the periodic structures. Mathematically, let's say the measured TRL calibrated T-parameters were T_{DUT}, the corrected measurements were $T_{Periodic}$, and the input and output transition simulations were T_{in} and T_{out}. The periodic structure measurements would then be computed using equation B.3.

$$T_{Periodic} = T_{in}^{-1} T_M T_{out}^{-1} \tag{B.3}$$

Appendix C

Minimum Relative Permittivity for Full-Space Scanning Waveguide Based Periodic LWAs

The minimum substrate permittivity for a waveguide based periodic LWA in order to ensure grating lobe free scanning is more stringent than for a TEM transmission line based periodic LWA. The minimum waveguide substrate permittivity depends on the cutoff frequency in relation to the desired broadside frequency. The derivation presented in this appendix assumes negligible perturbation of the waveguide mode (as was assumed for the TEM transmission line minimum permittivity derivation [19] shown in Chapter 2) and is as follows. Firstly, given

$$k = \frac{\sqrt{\epsilon_r}\omega}{c}, \tag{C.1}$$

$$k_c = \frac{\sqrt{\epsilon_r}\omega_c}{c}, \tag{C.2}$$

and

$$\frac{\beta}{k_0} = \frac{c}{\omega}\sqrt{k^2 - k_c^2} = \sqrt{\epsilon_r - \epsilon_r\frac{\omega_c^2}{\omega^2}}, \tag{C.3}$$

where ω_c is the waveguide cutoff frequency, and defining ω_{u2} as the frequency where the $n = -2$ space harmonic becomes fast (radiating), ω_{u1} as the frequency where the $n = 0$ space harmonic becomes slow (non-radiating), and ω_b as the desired broadside frequency,

then

$$\frac{\beta_{-1}}{k_0} = \sqrt{\epsilon_r - \epsilon_r \frac{\omega_c^2}{\omega_{u2}^2}} - \sqrt{\epsilon_r \frac{\omega_b^2}{\omega_{u2}^2} - \epsilon_r \frac{\omega_c^2}{\omega_{u2}^2}} = 1 \tag{C.4}$$

and at the same frequency

$$\frac{\beta_{-2}}{k_0} = \sqrt{\epsilon_r - \epsilon_r \frac{\omega_c^2}{\omega_{u2}^2}} - 2\sqrt{\epsilon_r \frac{\omega_b^2}{\omega_{u2}^2} - \epsilon_r \frac{\omega_c^2}{\omega_{u2}^2}} = -1. \tag{C.5}$$

Now, equating expressions C.4 and negative C.5 allows solving of ω_{u2} in terms of the desired waveguide cutoff frequency and broadside frequency.

$$\sqrt{\epsilon_r - \epsilon_r \frac{\omega_c^2}{\omega_{u2}^2}} - \sqrt{\epsilon_r \frac{\omega_b^2}{\omega_{u2}^2} - \epsilon_r \frac{\omega_c^2}{\omega_{u2}^2}} = -\sqrt{\epsilon_r - \epsilon_r \frac{\omega_c^2}{\omega_{u2}^2}} + 2\sqrt{\epsilon_r \frac{\omega_b^2}{\omega_{u2}^2} - \epsilon_r \frac{\omega_c^2}{\omega_{u2}^2}} \tag{C.6}$$

$$\omega_{u2}^2 = \frac{9}{4}\omega_b^2 - \frac{5}{4}\omega_c^2 \tag{C.7}$$

Enforcing this value of ω_{u2} using the substrate relative permittivity will result in the $n = -1$ space harmonic leaving the fast-wave region at exactly the same frequency as the $n = -2$ space harmonic enters the fast-wave region. To calculate the necessary substrate relative permittivity, ω_{u2} is substituted back into the equation C.4, resulting in:

$$\epsilon_r > \left(\frac{1}{\sqrt{1 - \frac{4\omega_c^2}{9\omega_b^2 - 5\omega_c^2}} - \sqrt{\frac{4\omega_b^2 - 4\omega_c^2}{9\omega_b^2 - 5\omega_c^2}}} \right)^2 . \tag{C.8}$$

This condition is entirely dependent on choice of cutoff frequency ω_c and broadside frequency ω_b. The same procedure can be followed for calculating the required ϵ_r such that the fundamental $n = 0$ mode will leave the fast-wave region at exactly the same frequency (ω_{u1}) that the $n = -1$ mode begins to radiate. Skipping the details of the derivation, it can be

shown that:

$$\omega_{u1}^2 = \frac{1}{4}\omega_b^2 + \frac{3}{4}\omega_c^2 \tag{C.9}$$

from which another condition on ϵ_r for grating lobe free scanning can be written as,

$$\epsilon_r > \left(\frac{1}{\sqrt{1 - \frac{4\omega_c^2}{\omega_b^2 + 3\omega_c^2}} - \sqrt{\frac{4\omega_b^2 - 4\omega_c^2}{\omega_b^2 + 3\omega_c^2}}} \right)^2 . \tag{C.10}$$

This condition is less stringent than the previous condition for any choice of f_b and f_c. The required permittivity then for grating lobe free scanning relies on equation C.8 which depends on the ratio of the desired broadside frequency to the waveguide cutoff frequency. This result is best presented graphically as shown in Figure C.1.

Now, the upper operating frequency (i.e. ω_{u2}, the frequency at which the $n = -1$ stops radiating and the $n = -2$ mode begins to radiate) should be less than three times the HMSIW cutoff frequency to avoid higher order modes propagating in the waveguide. The upper operating frequency ω_{u2} in equation C.7 entirely depends on the waveguide cutoff frequency and the desired broadside frequency and thus can be rearranged to enforce the condition $\omega_{u2}/\omega_c < 3$:

$$\frac{\omega_{u2}}{\omega_c} = \sqrt{\frac{9}{4}\frac{\omega_b^2}{\omega_c^2} - \frac{5}{4}} < 3 \tag{C.11}$$

which translates to a condition on the broadside frequency to cutoff frequency ratio, i.e.

$$\frac{\omega_b}{\omega_c} < 2.134 \tag{C.12}$$

which would be further restricted for a full SIW where $\omega_{u2}/\omega_c < 2$ in order to avoid higher order mode propagation. The domain of Figure C.1 (f_b/f_c) was therefore limited to given an

upper limit of 2.134 and a lower limit of $f_b/f_c = 1.1$ where already the permittivity values are unrealistically high for most applications.

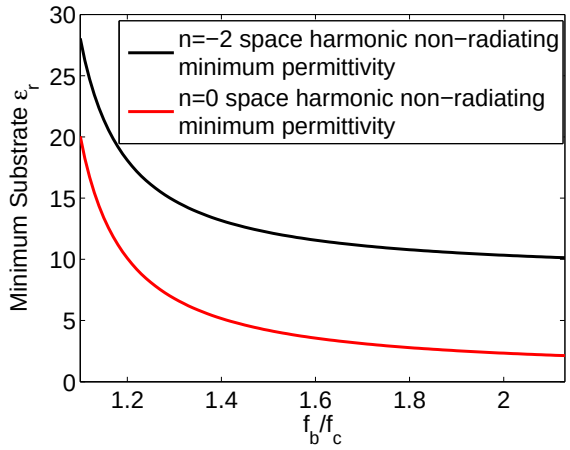

Figure C.1: Minimum permittivity requirement for an unperturbed HMSIW modeled periodic LWA with full-space grating lobe free scanning as a function of f_b/f_c

From Figure C.1 it is clear that choosing a cutoff frequency as far below the desired broadside frequency as possible will minimize the required substrate permittivity for full space scanning.

Now, following the same derivation process for a periodic phase-reversal LWA, we can first write:

$$\beta_n = \beta_0 + (2n+1)\beta_0(\omega_b) \tag{C.13}$$

from which β_{-1}/k_0 can be written as,

$$\frac{\beta_{-1}}{k_0} = \sqrt{\epsilon_r - \epsilon_r \frac{\omega_c^2}{\omega_{u2}^2}} - \sqrt{\epsilon_r \frac{\omega_b^2}{\omega_{u2}^2} - \epsilon_r \frac{\omega_c^2}{\omega_{u2}^2}} = 1 \tag{C.14}$$

and β_{-2}/k_0 as,

$$\frac{\beta_{-2}}{k_0} = \sqrt{\epsilon_r - \epsilon_r \frac{\omega_c^2}{\omega_{u2}^2}} - 3\sqrt{\epsilon_r \frac{\omega_b^2}{\omega_{u2}^2} - \epsilon_r \frac{\omega_c^2}{\omega_{u2}^2}} = -1 \tag{C.15}$$

which when equated leads to:

$$\omega_{u2}^2 = 4\omega_b^2 - 3\omega_c^2. \tag{C.16}$$

which when substituted back into equation C.14 will lead to the required permittivity to avoid grating lobes from the $n = -2$ space harmonic given some desired broadside to cutoff frequency ratio. Avoiding radiation from the fundamental mode of the periodic phase-reversal LWA results in the same condition on ω_{u1} as for the non-phase-reversal periodic LWA, i.e.

$$\omega_{u1}^2 = \frac{1}{4}\omega_b^2 + \frac{3}{4}\omega_c^2, \tag{C.17}$$

which when substituted back into equation C.14 will lead to the required permittivity to avoid grating lobes from the $n = 0$ space harmonic given some desired broadside and cutoff frequency ratio. In the case of the periodic phase-reversal LWA, the resulting permittivity requirement to avoid $n = 0$ space harmonic grating lobes is not always less stringent than the permittivity requirement to avoid $n = -2$ grating lobes, as is shown in Figure C.2.

Again, the upper operating frequency (i.e. ω_{u2}, the frequency at which the $n = -1$ stops radiating and the $n = -2$ mode begins to radiate) should be less than three times the HMSIW cutoff frequency to avoid higher order modes propagating in the waveguide. The upper operating frequency ω_{u2} in equation C.16 entirely depends on the waveguide cutoff frequency and the desired broadside frequency and thus can be rearranged to enforce the condition $\omega_{u2}/\omega_c < 3$:

$$\frac{\omega_{u2}}{\omega_c} = \sqrt{4\frac{\omega_b^2}{\omega_c^2} - 3} < 3 \tag{C.18}$$

which translates to a condition on the broadside frequency to cutoff frequency ratio, i.e.

$$\frac{\omega_b}{\omega_c} < 1.732. \tag{C.19}$$

The domain of Figure C.2 (f_b/f_c) was therefore limited to given an upper limit of 1.732 and a lower limit of $f_b/f_c = 1.1$ where already the permittivity values are unrealistically high for most applications.

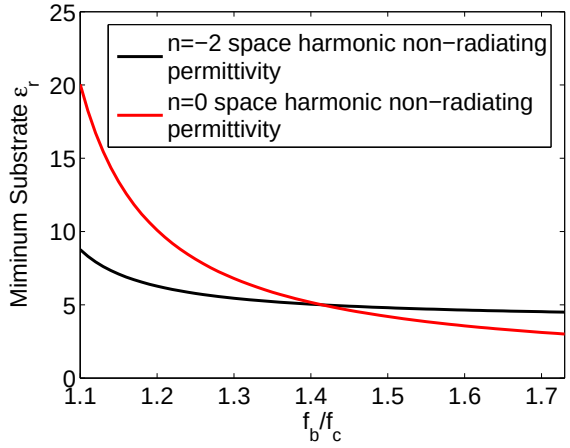

Figure C.2: Minimum permittivity requirement for an unperturbed HMSIW modeled periodic phase-reversal LWA with full-space grating lobe free scanning as a function of f_b/f_c

The analysis in this appendix was attempted a few times over the course of the research presented in this thesis but was not completed until after the antenna designs. In the future, it could be very useful for optimal waveguide design for periodic and periodic phase-reversal LWAs given a desired broadside frequency, scan range, and operating frequency bandwidth.